5-2013

Southward Continuation of the San Jacinto Fault Zone through and beneath the Extra and Elmore Ranch Left-Lateral Fault Arrays, Southern California

Steven Jesse Thornock
Utah State University

SOUTHWARD CONTINUATION OF THE SAN JACINTO FAULT ZONE THROUGH AND BENEATH THE EXTRA AND ELMORE RANCH LEFT-LATERAL FAULT ARRAYS, SOUTHERN CALIFORNIA

by

Steven J. Thornock

A thesis submitted in partial fulfillment
of the requirements for the degree

of

MASTER OF SCIENCE

in

Geology

Approved:

_____	_____
Susanne U. Janecke Major Professor	James P. Evans Committee Member
_____	_____
Anthony Lowry Committee Member	Mark R. McLellan Vice President of Research and Dean of the School of Graduate Studies

UTAH STATE UNIVERSITY
Logan, Utah

2013

ABSTRACT

Southward Continuation of the San Jacinto Fault Zone through and beneath the Extra and Elmore Ranch Left-Lateral Fault Arrays, Southern California

by

Steven J. Thornock, Master of Science

Utah State University, 2013

Major Professor: Dr. Susanne U. Janecke
Department: Geology

The Clark fault is one of the primary dextral faults in the San Jacinto fault zone system, southern California. Previous mapping of the Clark fault at its southern termination in the San Felipe Hills reveals it as a broad right lateral shear zone that ends north of the crossing, northeast-striking, left-lateral Extra fault. We investigate the relationship between the dextral Clark fault and the sinistral Extra fault to determine whether the Clark fault continues to the southeast. We present new structural, geophysical and geomorphic data that show that the Extra fault is a ~7 km wide, coordinated fault array comprised of four to six left-lateral fault zones. Active strands of the Clark fault zone persists through the Extra fault array to the Superstition Hills fault in the subsurface and rotate overlying sinistral faults in a clockwise sense. New detailed structural mapping between the San Felipe and Superstition Hills confirms that there is no continuous trace of the Clark fault zone at the surface but the fault zone has uplifted an elongate region ~950 km. sq. of latest Miocene to Pleistocene basin-fill in the field

area and far outside of it. Detailed maps and cross sections of relocated microearthquakes show two earthquake swarms, one in 2007 and another in 2008 that project toward the San Felipe Hills, Tarantula Wash and Powerline strands of the dextral Clark fault zone in the San Felipe Hills, or possibly toward the parts of the Coyote Creek fault zone. We interpret two earthquake swarms as activating the San Jacinto fault zone beneath the Extra fault array. These data coupled with deformation patterns in published InSAR data sets suggest the presence of possible dextral faults at seismogenic depths that are not evident on the surface.

We present field, geophysical and structural data that demonstrate dominantly left-lateral motion across the Extra fault array with complex motion on secondary strands in damage zones. Slickenlines measured within three fault zones in the Extra fault array reveal primarily strike-slip motion on the principal fault strands. Doubly-plunging anticlines between right-stepping en echelon strands of the Extra fault zone are consistent with contraction between steps of left-lateral faults and are inconsistent with steps in dominantly normal faults. Of the 21 published focal mechanisms for earthquakes in and near the field area, all record strike-slip and only two have a significant component of extension.

Although the San Sebastian Marsh area is dominated by northeast-striking left-lateral faults at the surface, the Clark fault is evident at depth beneath the field area, in rotated faults, in microseismic alignments, and deformation in the Sebastian uplift. Based on these data the Clark fault zone appears to be continuous at depth to the Superstition Hills fault, as Fialko (2006) hypothesized with more limited data sets.

(178 pages)

PUBLIC ABSTRACT

Steven J. Thornock

The Clark fault is a significant fault within the southern San Andreas fault system. The Clark fault abruptly ends where it intersects a second, smaller fault that crosses it called the Extra fault zone. In this study we investigate the possibility of the Clark fault continuing beneath and beyond the Extra fault zone. Based on field mapping and other geological data that we present, we determine that the Clark fault continues below the Extra fault and is not evident on the surface. Over time, earthquake slip along the Clark fault has caused the Extra fault zone to rotate in a clockwise direction. Both fault zones have high potential for causing a high magnitude (M >6.0) earthquake in the near future.

A second objective of this study is to identify the direction of motion along the Extra fault zone and related faults. Data collected from the field indicate that the fault is a strike-slip fault that moves in a left-lateral sense. Previously published geophysical data support our data collected in the field.

ACKNOWLEDGMENTS

Foremost my thanks go to the Southern California Earthquake Center (SCEC) for funding this research and to Utah State University for giving me opportunities to teach. I am immensely grateful for this opportunity of learning provided by Susanne Janecke. Without Susanne's insights, motivation, truck, and plain hard work, this project would never have reached fruition. So many others assisted in this process including the other members of my committee, Jim Evans and Tony Lowry. My thanks go to Erik Mustonen for allowing me to encroach on his generous hospitality during weeks of fieldwork. Also to Tammy Rittenour for graciously accepting a structure student into her OSL short course and for her patient help. Huge thanks go to my fellow students who were always supportive and encouraging. Especially to Mitch Prante who, regardless of his busy schedule, always had time to help and talk. Finally to my wife, Christie, who sacrificed in often unnoticed ways over the course of this life-changing experience.

Steven J. Thornock

CONTENTS

LIST OF TABLES

Table

LIST OF FIGURES

Figure

LIST OF PLATES

INTRODUCTION AND MOTIVATION

GEOLOGIC SETTING

Southern California encompasses a transitional zone between the San Andreas transform fault to the north and Gulf of California spreading centers to the south (Fig. 1; Atwater, 1970). The zone is comprised of four primary northwest-striking dextral fault zones that are roughly parallel to each other. The broad zone from northeast to southwest, respectively, consists of the San Andreas, San Jacinto, San Felipe, and Elsinore fault zones (Fig. 1; Dibblee, 1954; Sharp, 1967; Wallace, 1990; Janecke et al., 2010) that accommodate the Pacific and North American plate motion (Atwater, 1970). Strain is primarily dextral-slip motion and split fairly evenly between the San Andreas fault and the San Jacinto fault zone with smaller contributions from the Elsinore or San Felipe faults (Sanders, 1989; Matti and Morton, 1993; Fialko, 2006; Janecke et al., 2010).

Starting as early as 6-8 Ma, slip along the West Salton detachment fault and the San Andreas fault formed the expansive West Salton Trough (Fig. 1; Dibblee, 1954, 1984; Winker and Kidwell, 1986, 1996; Axen and Fletcher, 1998; Dorsey, 2006; Dorsey et al., 2007, 2011, 2012; Steely et al., 2009; Janecke et al., 2010). Slip continued until about 1.1-1.5 Ma when a major structural reorganization stopped motion across the West Salton detachment fault and transferred the strain to new dextral slip faults of the San Felipe, San Jacinto and Elsinore fault zones (Fig. 1; Johnson and Hutton, 1982; Johnson et al., 1983; Matti and Morton, 1993; Lutz et al., 2006; Kirby et al., 2007; Steely et al., 2009; Janecke et al., 2010; Dorsey et al., 2012).

Figure 1: Regional Map showing the location of major fault zones and primary geographic names in the Southern San Andreas fault system. Faults are labeled and drawn in black on light-toned sections of the image and in white on more dark-tone sections of the underlying image. The field area is outlined in green west of the southern Salton Sea. The basemap is a Landsat image processed for ideal color contrast in the sediment and rock.

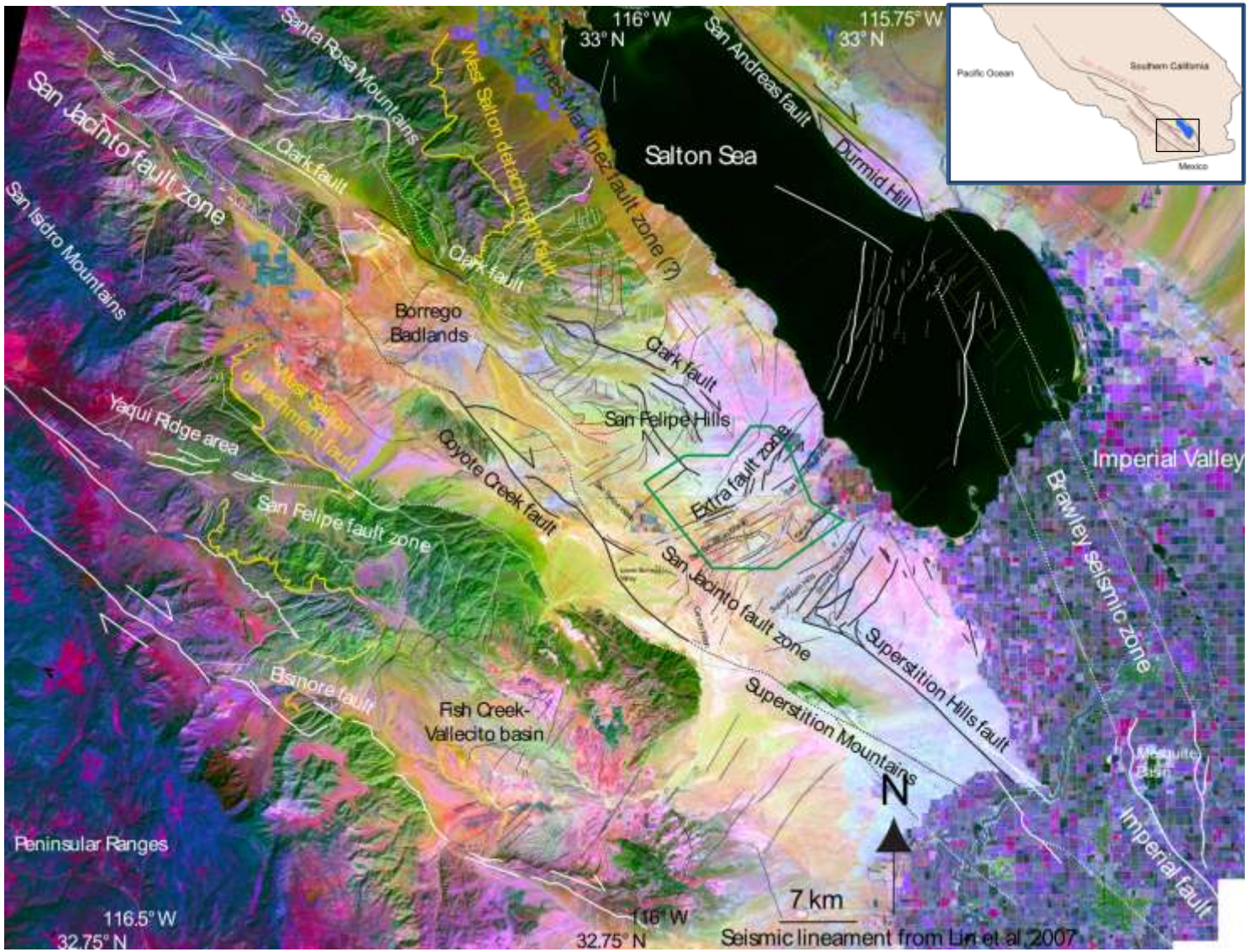
116° W
33° N
115.75° W
33° N
Santa Rosa Mountains
San Jacinto fault zone
San Isidro Mountains
Clark fault
West Salton detachment fault
Torres Martinez fault zone (?)
Salton Sea
San Andreas fault
Durmid Hill
Clark fault
Borrego Badlands
Clark fault
San Felipe Hills
Yaqui Ridge area
West Salton detachment fault
Coyote Creek fault
Extra fault zone
Imperial Valley
Brawley seismic zone
San Felipe fault zone
San Jacinto fault zone
Superstition Hills fault
Superstition Mountains
Imperial fault
Mesquite Basin
Borrego fault
Fish Creek-Vallecito basin
Peninsular Ranges
N
7 km
Seismic lineament from Lin et al. 2007
116.5° W
32.75° N
116° W
32.75° N
Pacific Ocean
Southern California
Mexico

The field area is located west of the Salton Sea within the San Sebastian Marsh area (Fig. 2). This is a broad low area between the San Felipe Hills and Superstition Hills regions (Fig. 2). The average ground elevation is about 25 m below sea level (bsl) and altitudes drop as low as about 70 m below sea level where San Felipe Wash flows into the Salton Sea. The lowest point in the center of the field area is roughly 40 m bsl.

Prior reconnaissance mapping showed the San Sebastian Marsh field area to be dominated by en echelon folds and northeast-striking left-lateral faults and mostly Holocene sediment (Dibblee, 1954, 1984; Sharp et al., 1989). South of the field area, in the Superstition Hills, the dextral Superstition Hills fault uplifted a sizable area of strongly folded and faulted Pleistocene sedimentary rocks of the Brawley Formation on its northeast side (Dibblee, 1954; 1984; Sharp et al., 1989). Large expanses of uplifted Pleistocene sediment in the field area and on the southwest side of the Superstition Hills fault were incorrectly mapped as Holocene cover by previous researchers (this study).

STRATIGRAPHY AND SEDIMENTOLOGY

The entire field area is within the Salton Trough (Fig. 2), the active depocenter for the eastern Peninsular Ranges and the Colorado River (Winker and Kidwell, 1996). Active subsidence and deposition of basin-fill over plutonic basement rock began as early as the latest Miocene, coeval with slip on the West Salton detachment fault (Dibblee, 1954, 1984; Winker, 1987; Winker and Kidwell, 1996; Axen and Fletcher, 1998; Dorsey, 2006; Dorsey et al., 2007, 2011; Steely et al., 2009; Janecke et al., 2010). Small, localized sedimentary basins began to form a few million years earlier adjacent to poorly understood structures (Shirvell, 2006). Uplift and erosion of the basin-fill sediments

Figure 2: Generalized map of key fault zones and geography of the field area and the surrounding area. All faults are red and are from the USGS Quaternary database and Janecke and Thornock (unpublished mapping). Some places near the field area without faults are unmapped and are labeled so. The field area is outlined in green between the San Felipe Hills and Superstition Hills in the low San Sebastian Marsh area. The basemap is from Google Earth of 2012 Digital Globe imagery.

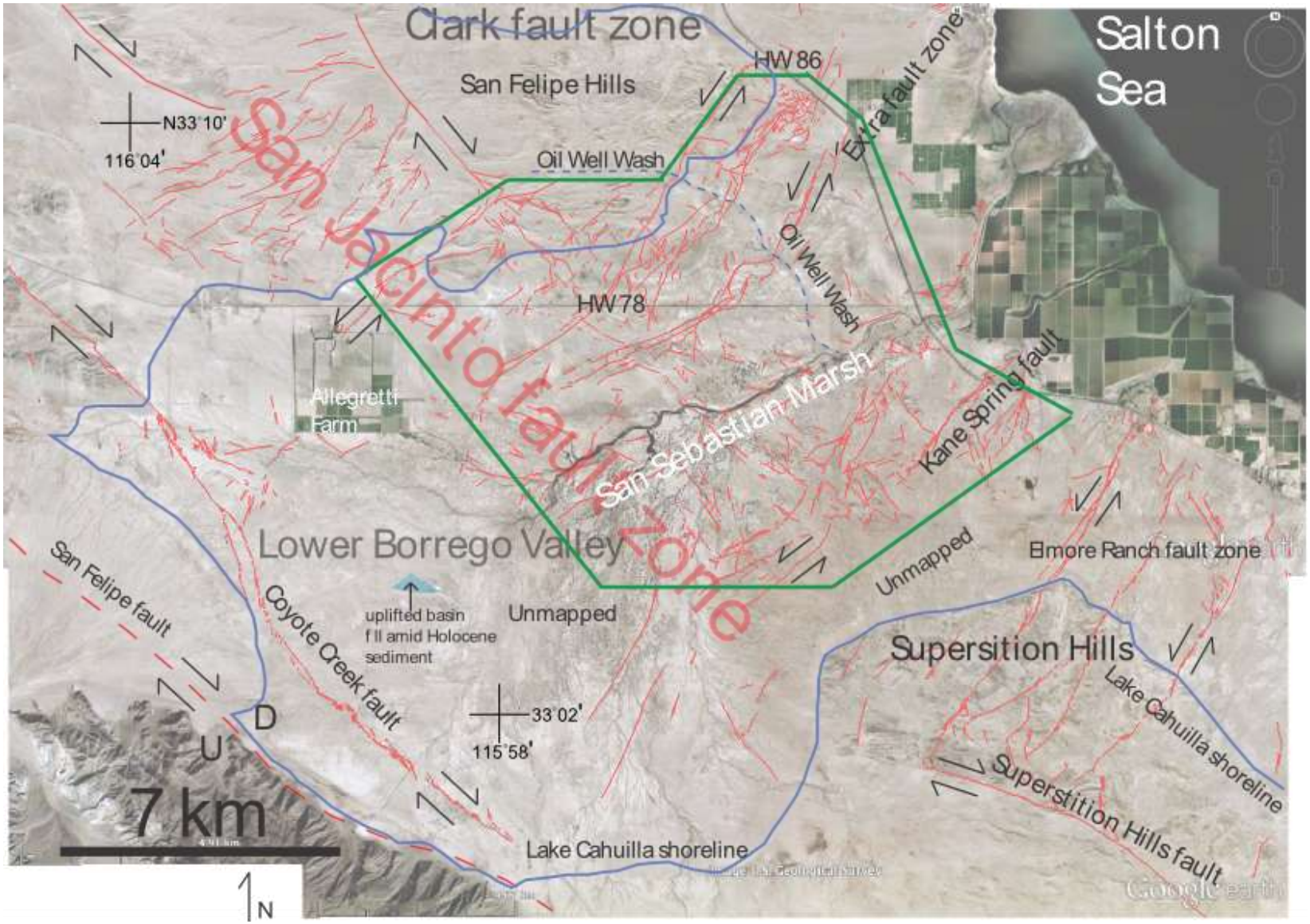
Clark fault zone
San Felipe Hills
HW 86
Extra fault zone
Salton Sea
N33°10'
116°04'
Oil Well Wash
San Jacinto fault zone
Oil Well Wash
HW 78
Allegretti Farm
San Sebastian Marsh
Kane Spring fault
Lower Borrego Valley
Unmapped
Elmore Ranch fault zone
San Felipe fault
Coyote Creek fault
uplifted basin fill amid Holocene sediment
Unmapped
Supersition Hills
Lake Cahuilla shoreline
33°02'
115°58'
D
U
7 km
Superstition Hills fault
Lake Cahuilla shoreline
N
Google earth

began after the structural reorganization that initiated slip on the San Jacinto and Elsinore fault zones (Johnson et al., 1983; Kirby et al., 2007; Janecke et al., 2010; Dorsey et al., 2011).

Rapid subsidence within the trough provided 5-6 km of accommodation space over a base of Cretaceous and older plutonic and metamorphic rocks and young mafic crust that formed in the central Salton Trough (Fig. 3; Sharp, 1967; Fuis and Kohler, 1984; Kohler and Fuis, 1986; Dorsey et al., 2011). The oldest widespread strata within the basin are formations of the marine Imperial Group (Fig. 3). These were deposited in shallow water when the Salton Trough was flooded by the Gulf of California in the latest Miocene (Dibblee, 1954, 1984; Johnson et al., 1983; Dorsey et al., 2011). This major marine incursion from the Gulf of California first produced evaporites of the Fish Creek Gypsum, then marine turbidites and nearshore deposits (Winker and Kidwell, 1996). The younger Palm Spring Group consists of units that are termed "L"-suite ("locally derived") and "C"-suite ("Colorado River") derived sediment (Winker and Kidwell, 1996). Locally derived sedimentary rocks from the Peninsular Ranges typically are light gray to greenish (Winker and Kidwell, 1996). Early units are primarily L-suite and later basin-fill sediment was provided primarily from the Colorado River with orange-red to red-brown sedimentary rocks that typify Colorado Plateau source rocks (Dibblee, 1954; Winker and Kidwell, 1986). The C-suite sediment filled all but a narrow proximal fringe of the basin near the West Salton detachment fault when it was active (Kairouz, 2005; Steely, 2006). Over time the ancestral Colorado River was deflected to its current path by motion across the San Andreas fault (Winker and Kidwell, 1986; Dorsey et al., 2011).

Figure 3: Simplified geologic column of the San Felipe-Borrego basin and Fish Creek-Vallecito subbasin. Data include Dibblee (1954, 1984, 1996); Winker and Kidwell (1996); Dorsey (2006); Dorsey et al. (2007); Kirby (2005); Steely (2006); Belgarde (2007); Figure used from Janecke and others 2010 Fig. 5 with permission.

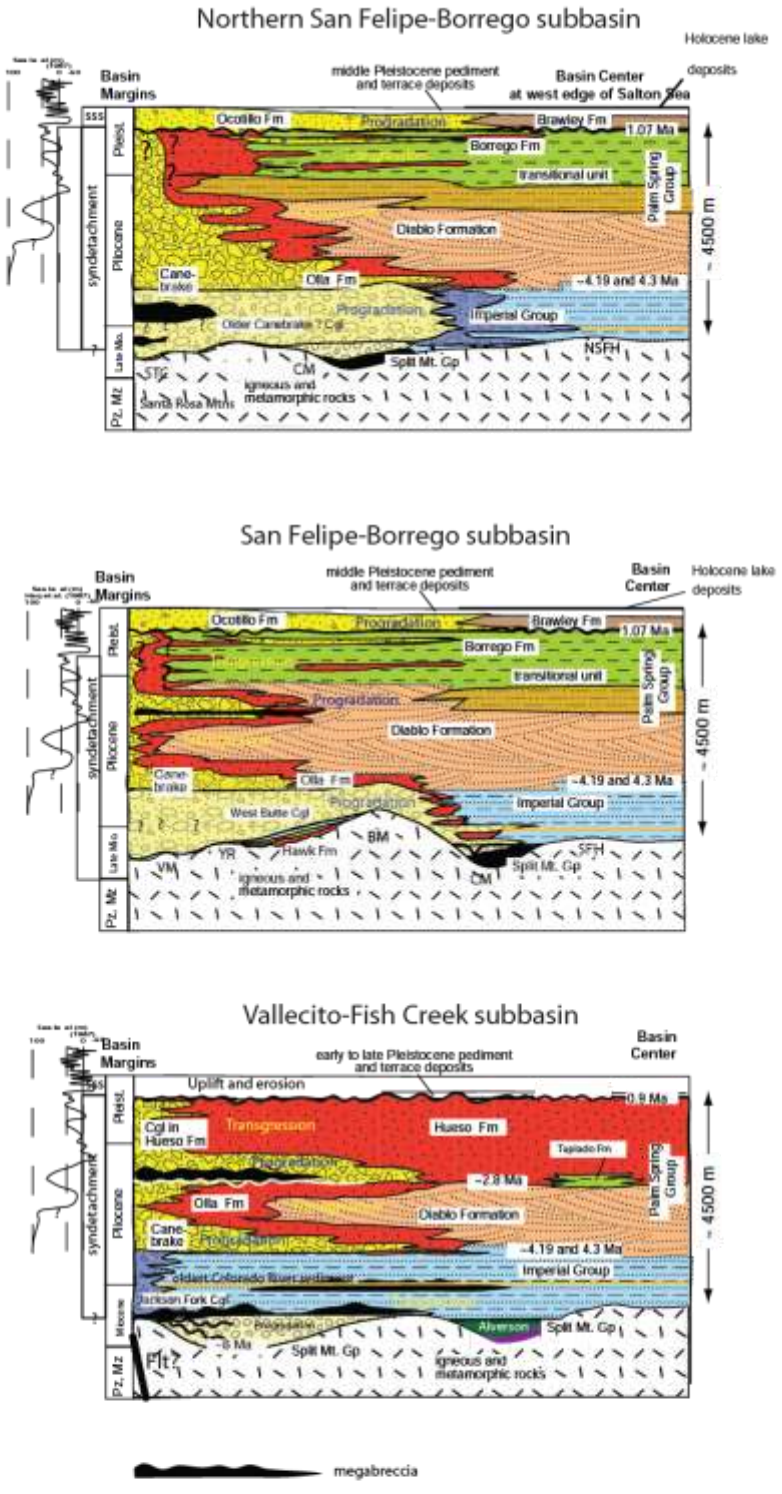
Northern San Felipe-Borrego subbasin
Holocene lake deposits
Basin Margins
middle Pleistocene pediment and terrace deposits
Basin Center at west edge of Salton Sea
Ocotillo Fm
Progradation
Brawley Fm
1.07 Ma
Borrego Fm
transitional unit
Palm Spring Group
Diablo Formation
~ 4500 m
Plioc.
Pleist.
syndetachment
Cane-brake
Olla Fm
~4.19 and 4.3 Ma
Progradation
Older Canebrake ? Cgl
Imperial Group
NSFH
Split Mt. Gp
CM
STF
igneous and metamorphic rocks
Santa Rosa Mtns
Pz. Mz
San Felipe-Borrego subbasin
Basin Margins
middle Pleistocene pediment and terrace deposits
Basin Center
Holocene lake deposits
Ocotillo Fm
Progradation
Brawley Fm
1.07 Ma
Borrego Fm
transitional unit
Palm Spring Group
Progradation
Diablo Formation
~ 4500 m
Plioc.
Pleist.
syndetachment
Cane-brake
Olla Fm
~4.19 and 4.3 Ma
Progradation
West Butte Cgl
Imperial Group
BM
YR
Hawk Fm
SFH
VM
Split Mt. Gp
CM
igneous and metamorphic rocks
Pz. Mz
Vallecito-Fish Creek subbasin
Basin Margins
early to late Pleistocene pediment and terrace deposits
Basin Center
Uplift and erosion
0.9 Ma
Cgl in Hueso Fm
Transgression
Hueso Fm
Taplado Fm
Palm Spring Group
Progradation
~2.8 Ma
Olla Fm
Diablo Formation
~ 4500 m
Plioc.
Pleist.
syndetachment
Cane-brake
Progradation
~4.19 and 4.3 Ma
oldest Colorado River sediment
Imperial Group
Jackson Fork Cgl
Miocene
Progradation
Alverson
Split Mt. Gp
~8 Ma
Split Mt. Gp
Flt?
igneous and metamorphic rocks
Pz. Mz
megabreccia

Since middle Pleistocene, when the West Salton detachment fault stopped being a significant regional structure, the Peninsular Ranges became a more widespread and voluminous sediment source in the western Salton Trough (Kirby et al., 2007; Steely et al., 2009; Janecke et al., 2010; Dorsey et al., 2011). Locally derived sediment accumulated in fluvial, eolian and lacustrine environments and sediment recycled from older basin fill became common-place (Kirby et al., 2007; Janecke et al., 2010).

The three formations that are exposed within the field boundary include the youngest member of the Palm Springs Group, the Borrego Formation, and the overlying Brawley and Ocotillo Formations (Fig. 3). The Borrego Formation is a ~1700-2500 m thick unit of mudstone and siltstone with less than fifty percent sandstone beds (Fig. 3; Lutz, 2005; Dorsey, 2006; Dibblee, 1984a; Lutz et al., 2006; Kirby et al., 2007; Housen and Dorsey, 2012). The time-transgressive basal contact is probably 2.9 Ma, middle to late Pliocene (Lutz et al., 2006; Kirby et al., 2007; Housen and Dorsey, 2012). Fossils indicate that deposition primarily occurred in an expansive, lacustrine-brackish setting (Dibblee, 1984a). Sediment was primarily sourced from the Colorado River with some input from local sources (Reitz, 1977; Wagoner, 1977; Dorsey, 2006; Kirby et al., 2007). The thick mudstones of this unit are generally massive and reddish-brown and sandstone is < 50% of the formation (Lutz et al., 2006; Kirby et al., 2007).

The laterally equivalent Ocotillo and Brawley formations overlie the Borrego Formation (Fig. 3; Dibblee, 1954, 1984; Lutz et al., 2006; Kirby et al., 2007). The Brawley and Ocotillo formations are generally conformable with the Borrego Formation below, but the contact changes laterally to a disconformity and an angular unconformity across the crest of a large basement-cored anticline (Dibblee, 1984a; Lutz et al., 2006;

Kirby et al., 2007). Distal Pleistocene fluvial, fluvial-deltaic, eolian and lacustrine deposits of mudstone, marlstone, siltstone and fine-grain sandstone make up the Brawley Formation (Fig. 3; Kirby et al., 2007). The Brawley Formation is younger than the Borrego Formation, and differs lithologically in being much more varied in provenance, its depositional environment, and presence of sedimentary structures and is somewhat coarser than the Borrego Formation. Some features present in the Brawley Formation that appear to be lacking in the Borrego Formation are large, sand-filled desiccation cracks, thick (> 10 cm) marlstone and micrite beds, climbing ripples, voluminous locally derived sand beds, and cross-bedded sandstone beds (Fig. 3; Kirby et al., 2007).

The coarser, time-equivalent sandstone and conglomerates of the Brawley Formation are the more proximal Ocotillo Formation (Fig. 3; Dibblee, 1984a; Lutz et al., 2006; Kirby et al., 2007). In distal locations the Ocotillo Formation sometimes separates the Brawley and Borrego Formations (Dibblee, 1984a), inter-fingers with, or replaces the Brawley all together (Fig. 3). The Ocotillo Formation is locally exposed in the cores of some uplifted domes and anticlines of the field area and typically is less than 3 m thick (Plate 1). East to northeast flowing streams likely deposited the Ocotillo Formation in a broad alluvial fan or fan-delta setting (Lutz et al., 2006; Kirby et al., 2007; Steely et al., 2009). Lutz et al. (2007) describes three general facies for the Ocotillo Formation in the Borrego Badlands, ~32 km to the west-northwest: a coarse sandy conglomerate, conglomerate sands, and bedded sands and silts with tabular bedding.

MAJOR STRUCTURE OF THE SAN JACINTO FAULT ZONE

The San Jacinto fault zone branches from the San Andreas fault northwest of San Bernardino (Dibblee, 1954; Rogers, 1965; Sharp, 1967, 1975; Jennings et al., 1982 Geologic map of California). Sharp (1967) suggested that the San Jacinto fault zone is the most active fault of the Southern San Andreas fault system (Fig. 4). Strands of the San Jacinto fault zone are en echelon, left-stepping and have dextral strike-slip motion (Sharp, 1967). Major strands of the San Jacinto fault zone include the Buck Ridge, Coyote Creek, Superstition Hills, Superstition Mountain and the Clark faults (Fig. 4; Dibblee 1954, 1984; Rogers, 1965; Sharp 1967, 1975). The Buck Ridge, Clark and Coyote Creek faults are in the central San Jacinto fault zone. The Coyote Creek fault is mostly continuous from its separation from the Clark fault southeast of Anza to its connection with the Imperial fault (Fig. 4; Sharp, 1967; Magistrale, 2002; Shearer et al., 2005).

The Clark fault has the largest lateral displacement of any fault within the San Jacinto fault zone, and may be it longest and straightest continuous fault (Fig. 4; Dibblee, 1954, 1984; Sharp, 1967; Janecke et al., 2010). Dextral slip on the Clark fault is confirmed by the M 6.2 Arroyo Salada earthquake in 1954 produced a focal mechanism with a steep fault plane striking N 56°W and only ~5% dip-slip (Sanders et al., 1986; Janecke et al., 2010). Maximum right-lateral displacement on the Clark and Buck Ridge fault zones is ~16.8 +3.7/−6.0 km based on the separation of distinctive crystalline rock in the Santa Rosa Mountains (Janecke et al., 2010; Forand, 2010).

The Clark fault steps right from the Claremont strand of the San Jacinto fault north of Hemet, CA (Sharp, 1967). Previous mapping had placed its other termination in

Figure 4: Regional fault map of the Southern San Andreas fault system. BRF—Buck Ridge fault; BR—Buck Ridge; NW- FCMF—NW Fish Creek Mountain fault; Segments of Clark fault: AS—Arroyo Salada segment; CVS—Clark Valley segment; HCS—Horse Canyon segment; TWS—Tarantula Wash segment; CVS—Clark Valley segment; SRS—Santa Rosa segment. Segments of Coyote Creek fault: BBS—Borrego Badlands segment; BMS—Borrego Mountain segment; CRS—Coyote Ridge segment; CS—central segment; SS Superstitions segment; SHS—Superstition Hills segment; SMS—Superstition Mountains segment. Segments of San Felipe fault zone: GC—Grapevine Canyon segment; MBS—Mescal Bajada segment; PR—Pinyon Ridge segment; FCMF—Fish Creek Mountain fault. Other names: BB—Borrego Badlands; BM—Borrego Mountain; BSF—Borrego Sink fold belt; Borrego syncline—BS; BRF—Buck Ridge fault; CCF—Coyote Creek fault; CF—Clark fault; DF—Dump fault; ER—Elmore Ranch fault; EVFZ—Earthquake Valley fault zone; FCM—Fish Creek Mountains; FCMF—Fish Creek Mountains fault; FCVB—Fish Creek–Vallecito basin; GC—Grapevine Canyon; H—Henderson Canyon fault; HC—Hell Canyon fault; KF—Kane Springs fault; OB—Ocotillo Badlands; PR—Pinyon Ridge; SFH—San Felipe Hills; SMA—Split Mountain anticline; SC—Sunset conglomerate of the Ocotillo Formation (hot pink); SCA—Salton City anticline; SF—Sunset fault; SFBB—San Felipe-Borrego basin; SFF—San Felipe fault; SR—Santa Rosa fault; SM—Superstition Mountain; SPF—Squaw Peak fault; SH— Superstition Hills; TB—Tierra Blanca Mountains; VLF—Veggie Line fault; VM—Vallecito Mountains; FCVB—Fish Creek–Vallecito basin; WSDF—West Salton detachment fault; WP—Whale Peak; YR—Yaqui Ridge. Faults are compiled and modifi ed from Rogers (1965), Jennings (1977), Morton (1999), Kirby (2005), Lutz (2005), Kennedy (2000, 2003), Kennedy and Morton (2003), Morton and Kennedy (2003), and Janecke et al., (2011). Mylonite was modifi ed from Sharp (1979), Kairouz (2005), and Steely (2006). Figure from Janecke et al., 2011 Figure 2. Used with permission from Janecke et al. (2010)

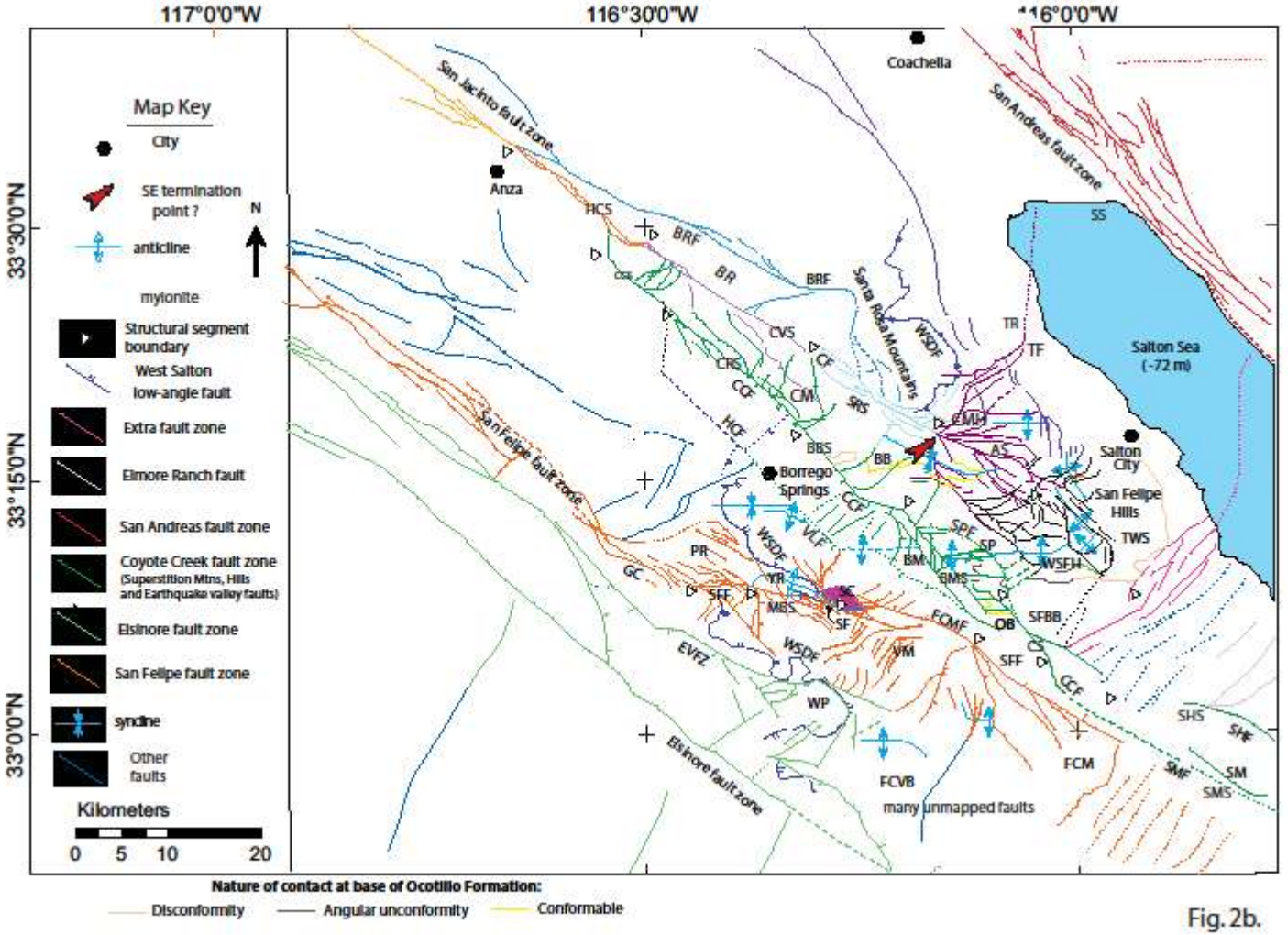
117°0'0"W
116°30'0"W
116°0'0"W
33°30'0"N
33°15'0"N
33°0'0"N
Map Key
City
SE termination point ?
anticline
mylonite
Structural segment boundary
West Salton low-angle fault
Extra fault zone
Elmore Ranch fault
San Andreas fault zone
Coyote Creek fault zone (Superstition Mtns, Hills and Earthquake valley faults)
Elsinore fault zone
San Felipe fault zone
syncline
Other faults
Kilometers
0 5 10 20
N
Coachella
San Jacinto fault zone
San Andreas fault zone
Anza
Salton Sea (-72 m)
Salton City
Borrego Springs
San Felipe Hills
Santa Rosa Mountains
Elsinore fault zone
many unmapped faults
HCS
BRF
BR
CVS
CRS
CCF
CM
SRS
HQF
BBS
BB
AS
CMH
TR
TF
SS
WSDF
VLF
SPF
SP
BM
EMS
WSFH
TWS
PR
GC
YR
SFF
MBS
SF
FCMF
OB
SFBB
EVFZ
YM
WP
FCVB
FCM
SHS
SHF
SMF
SM
SMS
Nature of contact at base of Ocotillo Formation:
Disconformity
Angular unconformity
Conformable

Fig. 2b.

the Arroyo Salada segment at the southern tip of the Santa Rosa Mountains (Figs. 1 and 4; Dibblee, 1954, 1984; Sharp, 1967, 1972; Bartholomew, 1970). Recent mapping by Kirby (2005) extends the fault 20-25 km farther south than previously defined and identified its termination about 3 km north of the Extra fault zone within the San Felipe Hills (Kirby et al., 2007; Belgarde, 2007; Janecke et al., 2010). This part of the Clark fault zone is referred to as the Tarantula Wash segment (Fig. 4; Belgarde and Janecke, 2007; Janecke et al., 2010). This new mapping and analysis extends the total length of the Clark fault to about 120 km (Kirby et al., 2007; Belgarde, 2007; Janecke et al., 2010). The southern termination of the Clark fault, at the surface, is revealed by unfaulted Brawley Formation and lack of surface rupture along its projected trace (Dibblee, 1954, 1984, 1996; Rogers, 1965; Sharp, 1967; Kirby, 2005; this study). The abrupt termination is thought to be due to truncation by northeast-striking cross faults in the north part of the current study area, at the southern edge of the San Felipe Hills (Fig. 2; Kirby, 2005; Kirby et al., 2007; Janecke et al., 2010).

The southern-most Clark fault has at least 4 major strands in a ~18 km wide shear-zone of very complex faulting and folding within the southern San Felipe Hills yet none cut clearly across the roughly E-W trending belt of Pleistocene Ocotillo and Brawley Formations or the Extra fault a short distance farther southeast (Fig. 2; Dibblee, 1954; Kirby, 2005; Belgarde, 2007; Kirby et al., 2007; Janecke et al., 2010; this study). A minimum of 5.6 +/- 0.4 km of dextral slip was calculated as necessary to produce the abundant and prominent folds within the southern part of the Tarantula Wash segment (Kirby, 2005; Janecke et al., 2010). The folded sedimentary rocks are Pliocene to Pleistocene and were dated using magnetostratigraphy (Kirby et al., 2007).

Long and active northwest-striking dextral faults accommodate most of the regional strain and are the dominant feature in the southern San Andreas fault system; however, conjugate northeast-striking left-lateral cross faults play an important role in local strain and structural relationships (Fig. 4; Clark, 1972; Sharp et al., 1982; Nicholson et al., 1986; Hudnut et al., 1989a; Sharp et al., 1989; Fialko, 2006; Kendrick et al., 2002). The cross faults are at a high angle to the master dextral faults in the southern San Andreas fault system, exhibit left-oblique motion and allow block rotation (Fig. 5; Hudnut et al., 1989b; Sanders, 1989; Sharp et al., 1989; Dickinson, 1996; Hauksson et al., 2012). Previously recognized northeast-striking left-lateral faults within or near the field area include strands of the Elmore Ranch, East and West Elmore Ranch, Kane Spring, East Kane Spring, Lone Tree and Extra faults (Fig. 5; Hudnut et al., 1989a; Sanders, 1989; Sharp et al., 1989; Kirby, 2005; Kirby et al., 2007).

PREVIOUS MAPPING AND GENERALIZED FINDINGS

Several reconnaissance and detailed geologic maps of the Imperial Valley and surrounding regions developed the overall structural and stratigraphic framework of the western Salton Trough (Dibblee 1954, 1984, 1996, Dibblee and Minch, 2008). Dibblee (1954, 1984, 1996) and Dibblee and Minch (2008) subdivided the stratigraphy, named the rock units, mapped and interpreted the main structures and produced the first large and medium scale geologic maps and cross sections. Rogers (1965) compiled a 1:250,000 scale geologic map of the San Jacinto fault zone but omitted some significant

Figure 5: Northeast-striking left-lateral fault arrays in the field area. Each array is outlined and filled with a different color. The NW-most fault array (blue) is the Tarantula Wash fault array outside of the study area. The majority of the field area is within the Extra fault array (green) but does cross into some of the Elmore Ranch fault array (purple). Both the Extra and Elmore Ranch fault arrays extend farther NE and the Extra fault array continues to the SW. The boundaries are generalized and only indicate which fault zones pertain to respective fault arrays.

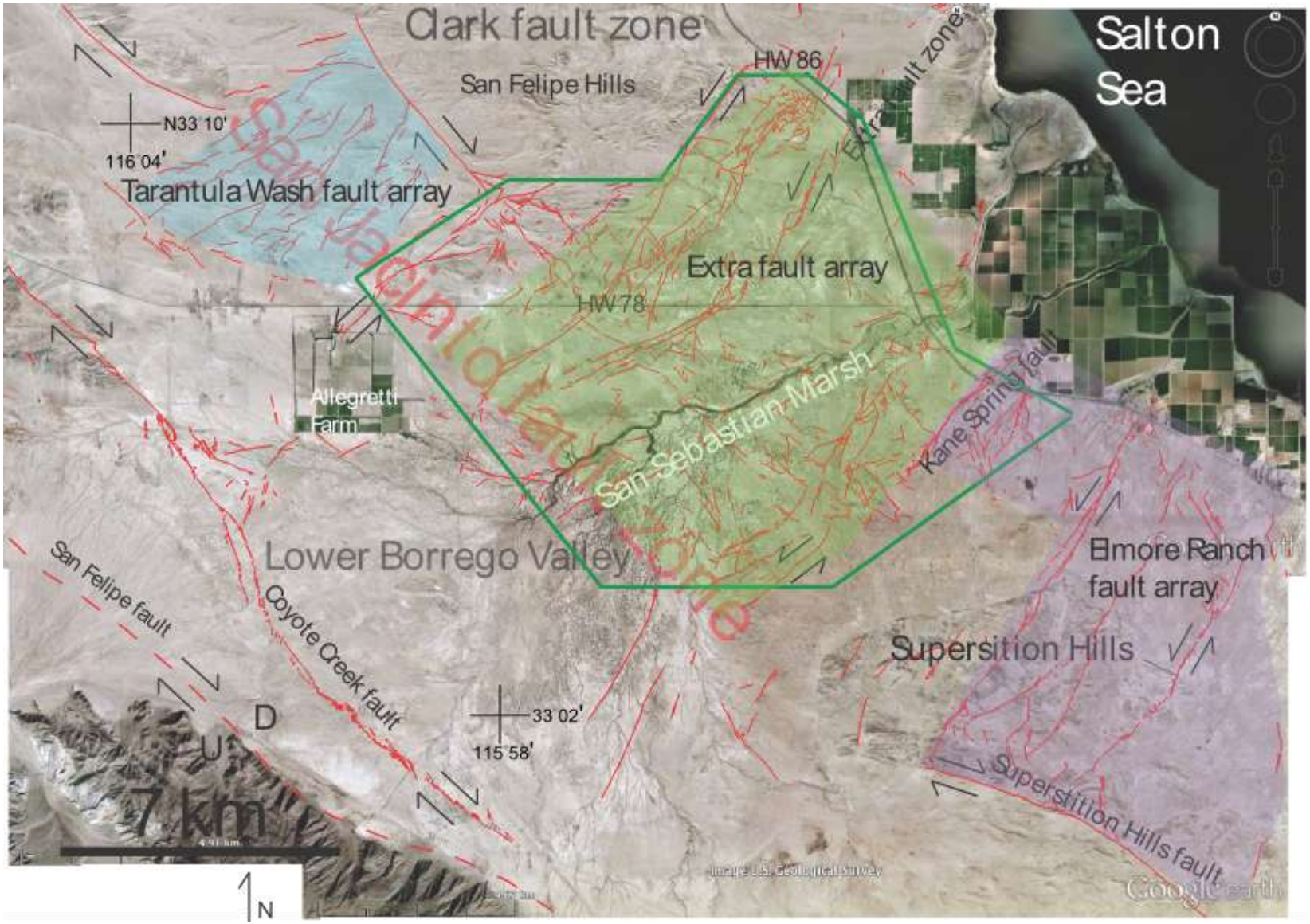
Clark fault zone
San Felipe Hills
HW 86
Extra fault zone
Salton Sea
N33 10'
116 04'
Tarantula Wash fault array
Extra fault array
HW 78
Allegretti Farm
San Sebastian Marsh
Kane Spring fault
Lower Borrego Valley
San Felipe fault
Coyote Creek fault
Elmore Ranch fault array
Supersition Hills
33 02'
115 58'
Superstition Hills fault
D
U
7 km
N
Image U.S. Geological Survey
Google earth

features that were later resolved by Sharp (1967, 1975). Sharp refined and corrected all mapping of the San Jacinto fault zone, producing a high quality geologic strip map but did not map southeast of the Santa Rosa Mountains (Sharp, 1967).

The Elmore Ranch and Superstition Hills earthquakes in 1987 led to the discovery of a large number of left-lateral strike-slip faults near and around the Superstition Hills, and structural maps of faults and folds within the Superstition Hills (Sharp et al., 1989; Hudnut et al., 1989a) but neither group mapped the current field area around San Sebastian Marsh. Kirby (2005), Kirby et al. (2007), Belgarde (2007), and Janecke and Belgarde (2008) built on prior thesis mapping by Morley (1963), Reitz (1977), Dronyk (1977), Heitmann (2002), Lilly (2003), and Bartholomew (1970) and documented many small-offset left-lateral faults within the San Felipe Hills and the southeast Santa Rosa Mountains. They demonstrated the complex geometries of the Clark fault, including its different structural geometries at shallow and deep crustal levels using 1:40,000 and 1:24,000 geologic maps, structural analysis and relocated microseismicity of Lin et al. (2007). Janecke and Belgarde (2008) inferred that mud-rich decollements facilitated an "overpass and underpass geometry" of strike-slip faulting in the Tule Wash area of the Clark fault zone. Recent developments in aerial photography, Google Earth, satellite photography, relocated earthquakes (Shearer et al., 2005; Lin et al., 2007, Yang et al., 2012) and constantly improving images allows for much higher precision in mapping areas of shallow topography such as this study area. Previous to this study, no detailed map of the San Sebastian Marsh area had been created.

Previous maps showed most of the field area as being covered by ancient Lake Cahuilla deposits from the Late Holocene because of its low elevation below the ancient

shorelines of the lake (Dibblee, 1954, 1984; Rogers, 1965; Hudnut et al., 1989a; Dibblee and Minch, 2008). In reality exhumed Pleistocene basin-fill is nearly continuous from the San Felipe Hills to Superstition Hills (Plate 1). Patches of thick Cahuilla deposits occur as terraces and localized fill along washes, as patchy sand dunes, and in the slightly raised parts of the study area as near-shore and beach deposits. The Holocene sediment forms patches and shoestring exposures instead of a thick continuous blanket of young sediment (Plate 1).

MOTIVATION

The Clark fault was previously mapped as having an abrupt termination about 3 km north of the Extra fault zone (Kirby, 2005; Belgarde and Janecke, 2006; Kirby et al., 2007; Janecke et al., 2011). This is somewhat unexpected considering the ~16.8 kilometers of offset on the southern Clark fault and the high slip rate of this right-lateral fault (Sharp, 1967; Kirby et al., 2007; Janecke et al., 2011). Some workers have inverted geodetic data and InSAR interferograms to suggest a through-going fault that connects the tip of the Clark fault, through the San Sebastian Marsh area with the Superstition Hills fault (Fialko, 2006; Wei et al., 2009). The primary purpose of this study is to investigate this hypothesis of a connection between the Clark fault and the Superstition Hills fault in light of the clear map data showing no significant dextral structure in the southernmost San Felipe Hills.

Fialko (2006) used InSAR collected from European Space Agency satellites 1 and 2 between 1992 and 2000 and geodetic data spanning from 1985 to 2005 to measure strain accumulation in the southern San Andreas fault system. He determined that strain

accumulation is split fairly equally between the San Andreas fault and the San Jacinto fault with a minor contribution from the Elsinore fault (Fig. 4). Computer simulations that assigned various slip-rates, locking depths and rigidity contrasts of the two fault zones computed where primary fault traces should be expected. He first assumed the Coyote Creek fault (Fig. 4) to be the primary strand of the San Jacinto fault zone based on geologically mapped traces but simulation results required an unreasonably high rigidity contrast across the actual location of the mapped trace of the Coyote Creek fault.

The values from the simulations that were most reasonable suggested that most of the strain in the San Jacinto fault zone was localized along the Clark - Superstition Hills fault area, directly through the array of northeast-striking faults of the Extra fault array (Fig. 2). Due to a lack of mapped surface traces, Fialko (2006) suggested that young Cahuilla sediments could cover the surface exposure of the connecting fault between the Clark and Superstition Hills faults or that a "blind fault" could be present in the study area. Sanders et al. (1986) similarly suggested that parts of the Clark fault are buried or blind. Without directly addressing the topic in the text, Wei and others (2009) implied that the Clark fault is continuous to the Superstition Hills fault in an InSAR interferogram by placing a dashed line between the Clark fault and the Superstition Hills fault (Wei et al., 2009). Their analysis of creep along the Superstition Hills fault, however, did not directly support or refute this hypothesis.

In this study we investigate the field relationship between the Clark fault and the smaller cross faults between the San Felipe Hills and the Superstition Hills in order to determine whether the Clark fault may be continuous southward or whether it is truncated at the intersection with the northeast-striking Extra fault array as most prior mapping

showed (Figs. 5, 6 A and B). We considered at least seven different geometric possibilities as our working hypotheses during early phases of this work (Table 1; Fig. 6). Field relationships and prior mapping showing lateral continuity of the Extra fault array quickly ruled out hypothesis 6C, 6D and 6F (Fig. 6) and focused our analysis of the remaining possibilities (Table 1; Fig. 6).

In November 1987 an M6.2 earthquake ruptured along the left-lateral Elmore Ranch fault zone and in adjacent faults in the Elmore Ranch fault array (Fig. 5; Hudnut et al., 1989a; Sharp et al., 1989). About 12 hours later, a M6.6 earthquake occurred at the intersection of the Elmore Ranch fault and the Superstition Hills fault and propagated southeastward along the Superstition Hills fault (Hudnut et al., 1989a; Sharp et al., 1989). Sinistral slip was recorded on the cross fault with as much as 120 mm of marker separation (Hudnut et al., 1989a). Motion on the Superstition Hills fault was dextral with as much as 90 cm measured slip including afterslip (Sharp et al., 1989). The smaller, initial earthquake on the sinisitral cross faults is interpreted to have triggered the larger M 6.6 earthquake on the master dextral fault (Hudnut et al., 1989a; Sharp et al., 1989). The same event triggered slip on other major dextral faults in the region, including the Imperial fault (Hudnut et al., 1989a) (Fig. 5).

The Elmore Ranch fault array is defined here as comprised of all the left-lateral faults that had some surface rupture in 1987, regardless of the length of the ruptured part of each fault (Fig. 5). The Kane Spring and Lone Tree faults are the outermost faults of this array (Fig. 7). The Elmore Ranch fault zone is at the center of the array and overlies the aligned planar microseismicity and aftershock sequences. Photogeologic mapping suggests that the Elmore Ranch fault may have the largest separations of any fault within

Figure 6: Seven simplified possible relationships between the Clark fault zone and the Extra-Elmore fault array. Actual strikes are used to represent the fault zones. The Clark and Extra fault zones are shown with single, solid lines but in reality are fault zones of varied widths. Figures A-D are cases that have been determined as not likely or impossible and include complete truncation of one fault zone against another (B and C) and one fault zone being completely inactive and cut by the other fault zone (A and D). E, F, and G illustrate possible and likely contributors to understanding the actual relationship of the two fault zones. E) A checkerboard pattern resulting from contemporaneous slip on both the Extra and Clark fault zones. F) The Clark fault as a blind fault (dashed line) with an area of resulting dextral rotation. G) An older left-laterally offset Clark fault and then a nascent section that cuts the Extra fault zone dextrally.

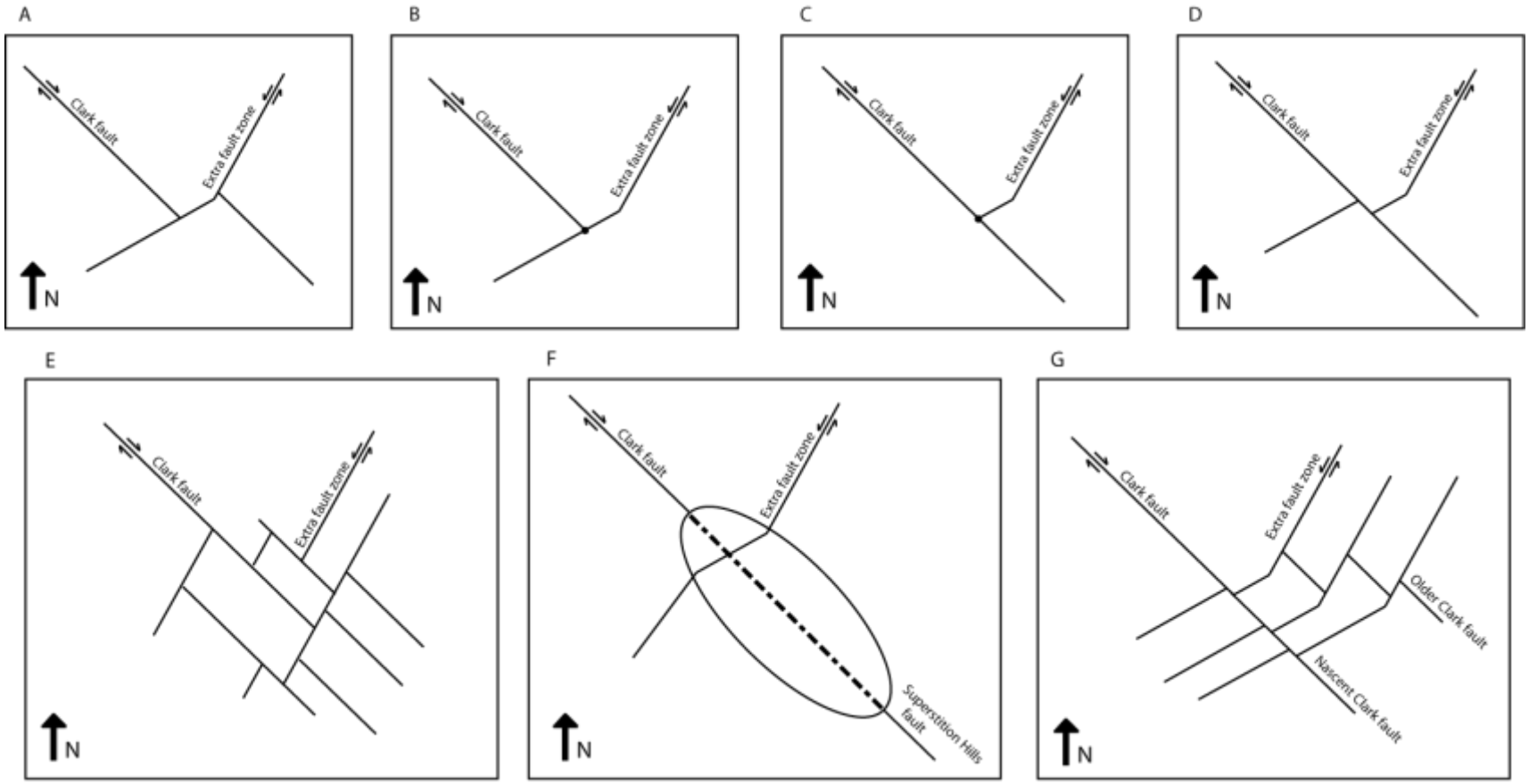
A
Clark fault
Extra fault zone
N
B
Clark fault
Extra fault zone
N
C
Clark fault
Extra fault zone
N
D
Clark fault
Extra fault zone
N
E
Clark fault
Extra fault zone
N
F
Clark fault
Extra fault zone
Superstition Hills fault
N
G
Clark fault
Extra fault zone
Older Clark fault
Nascent Clark fault
N

TABLE 1: SUMMARY OF KEY OBSERVATIONS, POSSIBLE EXPLANATIONS AND PREFERRED INTERPRETATIONS

Observation 2	Possible Explanations	Critical tests	Results of critical test, if available	Preferred interpretation
Faults in the Extra fault array have more easterly strikes along the projected trace of the Clark fault than other sections of the Extra fault array to the	Dextral motion along the Clark fault causes clockwise rotation of originally northeast-striking faults.	Paleomagnetic data should show significant clockwise rotation in the central zone. Also, rotation should be localized along the projection of the Clark fault zone.	Paleomagnetic data of Kirby et al. (2007) show 8° clockwise rotation in the transitional domain of the field area where some rotation is predicted by this interpretation (Fig. 16). No data are available in the central domain (fig. 16). Different strikes are spatially associated with the projection of the Clark fault zone.	More paleomagnetic work is needed in the central and western part of the Extra fault array to be
	The lateral differences in strike may be the original geometry of the Extra fault array	Paleomagnetic data would show no rotation about vertical axes anywhere. No consistent spatial relationship between the more easterly striking faults and the Clark fault zone	Paleomagnetic data of Kirby et al (2007) show some clockwise rotation where this model predicts none. The location of the strike change along the central part of several adjacent left-lateral faults is too regular to be a coincidence.	

northeast and southwest (Fig. 16)	The sections of the Extra fault array east and west of the more easterly striking faults were rotated counterclockwise relative to unrotated faults in the middle zone	Paleomagnetic data would show counterclockwise rotation in the east and west and none in the center. A structural explanation for this pattern is required	Rotations are mildly clockwise (Kirby et al., 2007) where counterclockwise rotations are expected in this model. There is no structure that would cause counterclockwise rotation	certain, but the available data are consistent with dextral rotation of the central domain.
	Some combination of processes produced the observed pattern	Limited amounts of rotation would be evident along strike of the Clark fault. Remaining geometry would be due to some other mechanism or origin.	This is difficult to assess without paleomagnetic data from several domains.	

Observation 3	Possible Explanations	Critical tests	Results of critical test, if available	Preferred interpretation
A concentrated zone of northwest-striking faults is southeast and along strike of the	These structures represent a nascent strand of the Powerline fault that will eventually mature into a continuous structure	Perhaps the zone is better developed in the subsurface. Geophysics might reveal some indication of the fault at depth	A swarm event in the subsurface activated a dextral northwest-striking fault that is almost along strike of the Powerline fault zone.	The fault zone represents a nascent strand of a northwest-striking fault that is

Powerline fault (Fig. 23)	The fault zone represents a concentration of small cross faults that is mostly unrelated to the larger Clark fault zone.	The faults would be oriented roughly similarly but would not necessarily share dip direction or be spatially concentrated.	The faults are spatially concentrated southeast of the Powerline fault in a higher density than surrounding areas.	more continuous at depth.

Observation 4	Possible Explanations	Critical tests	Results of critical test, if available	Preferred interpretation
Some groups of northwest-striking faults step left, southeast toward the Imperial fault. Photogeologic mapping suggests some dextral faults that are consistent with this geometric model are present along the east side of the Superstition Hills. A pair of those dextral	These zones represent an overall series of left steps toward the southeast	These fault zones would have formed independent of the northeast striking fault	The northwest-striking fault zones seem to terminate into the northeast-striking faults and are probably genetically related to them.	It is difficult to fully support the first interpretation, but the second is unlikely to be correct. More data are needed.
	These northwest-striking fault zones were once a continuous fault zone that has been deactivated and cut by younger, more active northeast-striking faults.	The reconstruction of offset along the northeast-striking faults would re-form the original continuous northwest-striking fault.	The individual northwest-striking fault zones vary too widely in their spacing, slip amount, and number of faults to have originally been one continuous fault.	
	There is a random pattern of dextral faults that does not involve stepping left between	Geologic mapping	More mapping is needed to fully characterize the geometry of this fault	

faults slipped in 1987 during the Superstition Hills and Elmore Ranch earthquake sequence (Sharp et al., 1989) (Fig. 24)	the northernmost tip of the Imperial fault and the Clark fault zone		zone	

Observation 5	Possible Explanations	Critical tests	Results of critical test, if available	Preferred interpretation
There are very few small earthquakes	The Extra fault array is locked so effectively that small earthquakes do not form within the damage zone.	Monitor the area for future small to large earthquakes. Only large earthquakes, followed by aftershocks, are predicted. Young Holocene fault scarps are predicted along the Extra fault array.	Other fault zones nearby have exhibited similar relationships of quiescence before large earthquakes (Hauksson et al 2010). The Extra fault array has many offset Holocene deposits.	The Extra fault zone has strong evidence for sizable paleoseismic events in the late Holocene
	The greatly reduced amount of activity might be due to abandonment of this section of the Extra fault zone array in favor of other structures.	No Holocene fault scarps are expected along the Extra fault array	This hypothesis is false because there are many places where the Extra fault array displaces Holocene sediment in the field area and it was active as recently as about 1000 years ago along	

beneath most of the Extra fault array (except in the southwest (Fig. 28)). This quiet zone is in marked contrast to adjacent areas. Both sinistral and dextral faults in the area have produced microseismicity (Fig. 30; Lin et al., 2007; Yang et al., 2012)			Bondit Wash (Fig. 5). The offshore continuations of the Extra fault array show compelling evidence for multiple, closely spaced Late Holocene earthquakes under the Salton Sea (Brothers et al., 2010).	(see observation 1). The quiescent part of this fault array is likely in a late stage of its evolution before an earthquake occurs. The best model for this future earthquake is the 1987 Elmore Ranch and Superstition Hills earthquakes, which were characterized by two earthquakes on conjugate, intersecting faults.
	The Extra fault array may be creeping in this area instead of producing microseismicity.	Geophysical tests including InSAR and geodetics would indicate motion even without seismic slip	InSAR does not reveal creep within the field area along northeast-striking faults of the Extra fault array (Lyons and Sandwell, 2003; Mellors and Boisvert, 2003; Van Zandt et al, 2004; Lundgren et al., 2009; Wei et al., 2009). Colluvial wedges along Bondit Wash are diagnostic of large paleoearthquakes along the Extra fault array and are not expected if creep was the dominant process along the fault array.	

Observation 6	Possible Explanations	Critical tests	Results of critical test, if available	Preferred interpretation
Aligned small earthquakes in the field area define northwest-striking and steeply dipping fault planes. Swarms activated the faults (Fig. 29). They are in a region dominated by northeast-striking faults.	Dextral faults of the Clark fault zone are active in the deep subsurface on fairly continuous planes but upward the strain is dispersed along detachment horizons and finally to northeast-striking faults.	Geophysical analyses might show evidence for or be consistent with subsurface faults with northwest strikes, dextral slip, that persist northwest and southeast of nearby and overlying sinisitral faults. A) InSAR could show strain on northwest-striking structures. B) Gravity and C) magnetic data might show a structural boundary aligned with the dextral fault zone instead of aligned with the sinistral fault zone. D and E The crest and southwest edge of the Sebastian uplift should align with the dextral fault zone instead of with the sinistral Extra and Elmore Ranch fault arrays.	A) InSAR indicates the location of a northwest-striking fault but does not necessarily confirm recent strain accommodation. B) Gravity in particular suggests a structure that is along trend of the Sebastian uplift toward the northwest and magnetic data shows a similar structure more subtly (e.g. Biehler and Rothstein, 1979; Langeheim and Jachens, 1993). D and E are confirmed (Fig. 32).	There is probably a continuous northwest-striking fault zone at depth but its location and relationship with the northeast-striking faults remains unclear.

	The dextral faults may be short connector faults between the more continuous sinistral faults of the Extra and Elmore Ranch fault arrays, and may not reflect the subsurface connection of the Clark fault and the Superstition Hills fault.	Swarms are expected to end at major sinistral faults and to define a checkerboard pattern of activity	The two primary swarms of microseismicity from 2007 and 2008 are continuous under as many as 6 NE-striking sinistral fault zones (Fig. 29)	

Observation 7	Possible Explanations	Critical tests	Results of critical test, if available	Preferred interpretation
The Sebastian uplift is centered on the southwestern strand of the Clark fault zone in the San Felipe Hills and persists southeast to the Superstition Hills and Superstition Mountains fault (Fig. 32)	The Sebastian uplift is a direct result of motion along the San Jacinto fault zone	The uplift should have a strong spatial relationship to the San Jacinto fault one	The prediction is met, see figure 32	The Sebastian uplift is genetically related to the Clark-Superstition Hills fault zone
	The Sebastian uplift is a regional transpressional feature of a different origin that only appears to be related spatially to the San Jacinto fault zone.	Some other structure produced the uplift	No other structure exists to produce the uplift	

Observation 8	Possible Explanations	Critical tests	Results of critical test, if available	Preferred interpretation

San Felipe Wash has a disproportionately small delta at the shore of the Salton Sea compared to its large drainage basin. This is even more out of proportion when one considers the adjacent and much smaller Tule and Arroyo Salada drainage basin and their associated delta (Fig. 33)	The Sebastian uplift traps sediment of San Felipe Wash on the southwest, restricting flow over the uplift to only small amounts of fine-grain sediment. Clay dominates the Salton Sea floor down slope of the San Felipe delta. Tule Wash and Arroyo Salada flow mostly down the east flank of the Sebastian uplift.	Determine the sediment accumulation rate on the west side of Sebastian uplift. Also, compare the amount of sediment being eroded in the San Felipe drainage basin with the amount being deposited within the delta.	Erosion and accumulation rates are not available. Gravity data shows, however, that the basin upstream of the Sebastian uplift is especially deep and thick (Langeheim and Jachens, 1993 gravity map of Borrego Valley quad). There is almost no exposed pre-Holocene sediment in Lower Borrego valley. Sediment from San Felipe Wash is fine grained in the delta.	Based only on the hydrologic unit sizes, the San Felipe Wash is depositing most of its sediment load before reaching the Salton Sea. Although there are several sediment traps along its course, the large Lower Borrego Valley, upstream of the Sebastian uplift, probably traps a lot of sediment and allows only clay escape to reach the Salton Sea.
	Other factors (like the steepness of the basin or the erodability of the bedrock) could explain this disparity	Topographic and geologic maps could provide a first-order estimation of erodability and steepness of the basin.	The geologic map shows that San Felipe Wash drains across more weakly to unconsolidated material than Arroyo Salada and Tule Wash. San Felipe Wash is less steep near the Salton Sea. These factors alone are unlikely to produce the large discrepancy between the deltas.	

	The San Felipe delta exhibits an expected aerial extent and the Tule and Arroyo Salada delta is anonymously large due to rapid erosion of the San Felipe Hills.	Determine the erosion rate within the San Felipe Hills and the relative amount of sediment transport of the Tule Wash with the San Felipe Wash.	Pediments in the drainage basin of Arroyo Salada and Tule Wash in the San Felipe Hills and near Truckhaven are roughly 22 to 62 ka and lie tens of meters above the active washes (Janecke et al., 2008). Erosion rates are not particularly high there.	

Observation 9	Possible Explanations	Critical tests	Results of critical test, if available	Preferred interpretation
Left-lateral faults appear to be spaced at semi-regular intervals (Fig. 17).	This geometry might be typical of conjugate cross faults between master dextral faults.	Cross fault and faults in strike-slip damage zones would typically be spaced regularly and be antithetic	They are typically antithetic but do not necessarily form in regular intervals.	Need more data to compare this section of the Extra fault array with other sections with a more northerly strike. The fairly regular interval is probably an original geometry, unrelated to rotation.
	The left-lateral faults might represent edges of clockwise-rotating blocks due to deeper dextral motion	Identify any clockwise rotation in the area and compare this geometry with other rigid, rotating blocks in strike-slip systems.	Kirby and others (2007) report some rotation in the field area but more work is needed to determine the role of left-lateral faults as rigid block boundaries.	

Figure 7: Northeast-striking left-lateral fault zones in the field area. Each NE-striking fault zone is labeled as discussed in the text. No NW-striking faults are shown. The Kane Spring fault indicates the start of the Elmore fault array toward the SE. Fault traces include USGS Quaternary faults and unpublished mapping from Janecke and Thornock. Basemap is of 2012 Digital Globe imagery from Google Earth.

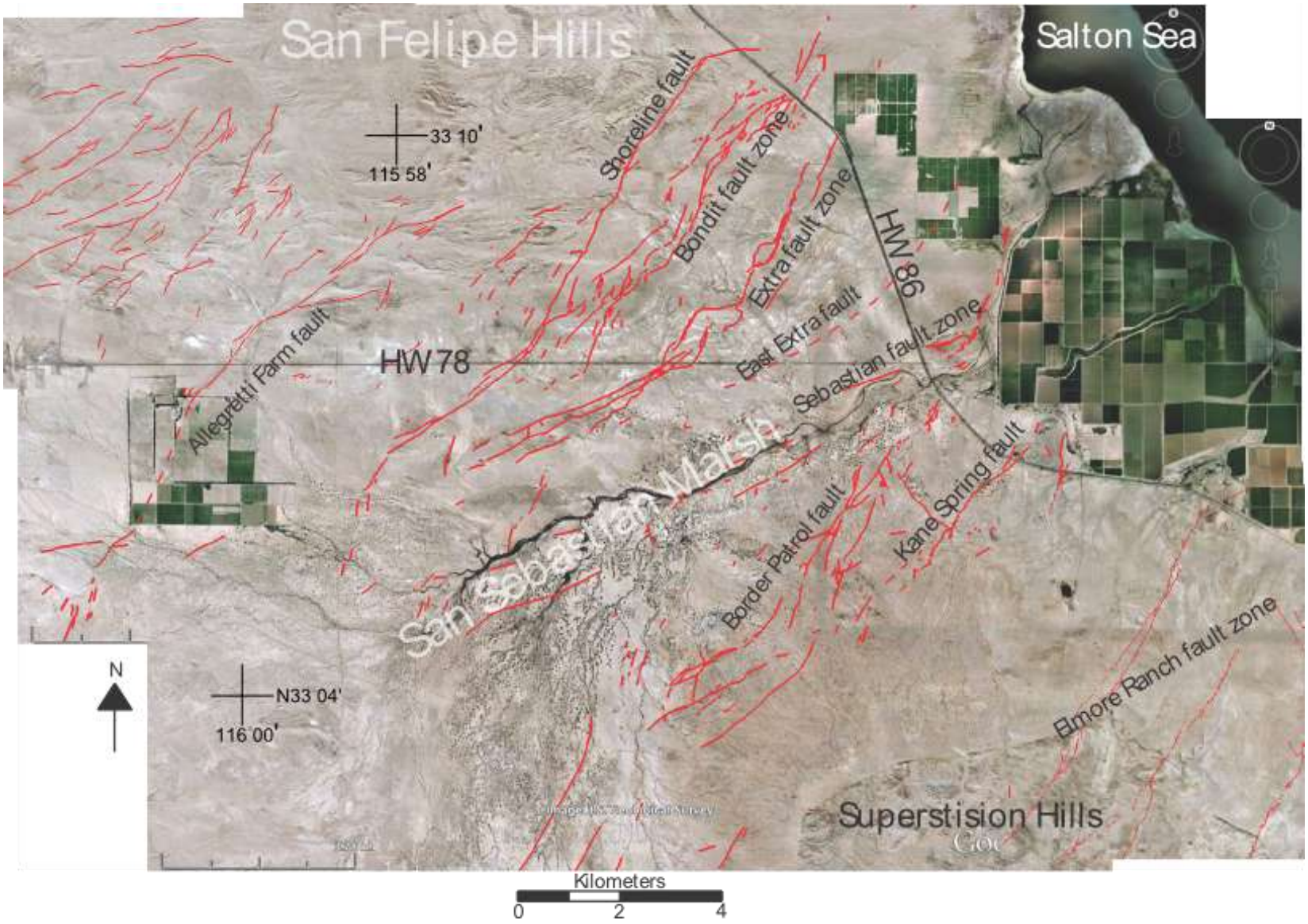
San Felipe Hills
Salton Sea
33 10'
115 58'
Shoreline fault
Bondit fault zone
Extra fault zone
HW 86
East Extra fault
Sebastian fault zone
HW 78
Allegretti Farm fault
San Sebastian Marsh
Border Patrol fault
Kane Spring fault
Elmore Ranch fault zone
N
N33 04'
116 00'
Superstision Hills
Kilometers
0
2
4

the Elmore Ranch fault array (Janecke, unpublished mapping). None of the other faults in the Elmore Ranch fault array produced aftershocks at depth (Lin et al., 2007). In the absence of the 1987 Elmore-Superstition Hills earthquakes, it would have been very difficult to separate the coordinated faults of the Elmore Ranch array from faults of adjacent arrays (Fig. 5).

The main zone of pervasive cross faults on the floor of the Salton Trough connects the Brawley Seismic zone to the San Jacinto fault zone farther to the west (Hudnut et al., 1989a; Sharp et al., 1989) (Fig. 7). Since these two bounding faults converge to the south, the left-lateral cross-faults become progressively shorter, and potentially less hazardous southward. Many cross faults in the Salton Trough are too short to produce large earthquakes, particularly near the Imperial fault (Hauksson et al., 2012). The Extra fault array, at ~43 km long, is the northernmost array between the Brawley seismic zone and the San Jacinto fault zone and has the longest trace of cross faults in this area (Hudnut et al., 1989a; Brothers et al., 2009, 2011). It is longer for two reasons: 1) it is the northernmost of the cross faults in the triangular area west of the Brawley seismic zone, and 2) its southwest branchpoint with the San Jacinto fault zone appears to be the Coyote Creek fault rather than the Superstition Hills fault (Fig. 7; Hudnut et al., 1989a; Brothers et al., 2009, 2011). The branchpoint adds 4-9 km to its length. The Elmore Ranch fault ruptured along 25 to 30 km and generated a M6.6 earthquake; at 40 to 45 km long, the Extra fault has the potential to produce a somewhat larger earthquake.

The 1987 Elmore Ranch and Superstition Hills sequence and other similar events reveal the dynamic relationship between smaller sinistral cross faults and master dextral faults and highlight the possibility of triggering sizable earthquakes on adjacent faults. Even small seismic events could trigger more significant events on the Clark or other master faults in the region (Sharp et al., 1989; Hudnut et al., 1989a). Early rupture on a sinisitral cross fault may have triggered the rupture on primary strands of the dextral San Jacinto fault zone during the M 6.4 1968 Borrego Mountain earthquake (Clark, 1972; Wesnousky, 2006) and 1979 Imperial Valley earthquake (Sharp et al., 1982). Another major purpose of this study, therefore, is to determine whether the Extra fault array has evidence for Holocene slip, sizable earthquakes, and type of geometric branch points with adjacent dextral faults that could lead to triggering a sequence of earthquakes similar to the Elmore Ranch and Superstition Hills earthquakes.

METHODS

FIELD METHODS

Field data were collected over the course of two field seasons in January-March and November-December 2011. A 1:24000 geologic map was produced from the field data and compiled using Google Earth as the final platform (Plate 1). Google Earth was chosen as the platform for several reasons. Being freeware, the map is accessible to the public. All data can include descriptions simply by clicking on the feature. Google Earth provides georeferenced, high resolution aerial and satellite imagery from many different periods of time. Dozens of images can be viewed using the history button in Google Earth. All imagery is pre-registered and free to access, and newer, more detailed imagery is added periodically.

Four sets of imagery were most useful for geologic mapping and analysis. The oldest imagery from June 2nd, 2002 from the US Geological Survey in Google Earth has very little color and was collected on a mid-summer morning. The resulting long shadows highlight fault scarps and other geomorphic features, resulting in imagery that mimics LiDAR and reveals many active structures. The identification of marker units and specific beds in the sedimentary section are easily identified in photography acquired by Digital Globe on November 23rd, 2005. The colors of the rocks are bright, varied, and high in contrast and there is some multispectral enhancement of the images in this set. The most recent imagery has the highest resolution but lacks bright, contrasting color. The fourth data set from September 4th, 2004 was very useful for its tonal contrasts and excellent definition of bedding traces. It does not have distinct colors and beds alternate

between light and dark, making them easy to trace. Unfortunately, this dataset was registered very poorly and features are shifted about 20 meters northwest with respect to the other imagery. The three other sets of imagery were registered into Google Earth very accurately with only 1-2 meters lateral offset between them and between features in the image and on the ground. There was excellent registration and rectification of the imagery in Google Earth, confirmed by the Toughbook computer GPS signal that showed the computer location on the Google Earth image at all times. Digital Orthophoto Quarter-Quadrangle (DOQQ) imagery from CalAtlas (atlas.ca.gov) was enhanced for color and contrast in Adobe Photoshop and printed at high resolution for use in the field.

We used and modified some data sets from published sources including Kirby (2005) and Google Earth (Key Markup Language) data from the United States Geological Survey Quaternary fault and fold database (http://earthquake.usgs.gov/hazards/qfaults/google.php last accessed Sep. 5, 2012). Photogeologic mapping was performed using Google Earth and orthophotographic imagery. We identified specific locations and lineaments that required field checking to confirm the presence of a structure and to make field measurements along it. Field data were collected in field notebooks, locations determined with a Garmin GPS, field maps with Universal Transverse Mercator (UTM zone 11) overlays and a Panasonic Toughbook computer (Panasonic Toughbook model U1 ultra). Each evening data were compiled into Google Earth and Microsoft Excel spreadsheets, combined with all previous data. The GPS data was collected using the North American Datum (NAD) 1983 and data points were transferred to Excel spreadsheets.

Planar and linear measurements were collected using a Brunton compass and recorded in a notebook with a corresponding UTM location and waypoint number. The right-hand-rule was used for most measurements for greater ease in data manipulation. In total 300 bedding planes and 152 fault planes were measured along with any slickenlines that included 16 reliable and reported measurements. Photographs were taken using a Canon Powershot A3000IS. Photographs were numbered in the camera (e.g. IMG_233) and retained their number when imported to a computer. This number was recorded in a notebook along with other data for each location. A shovel was used to expose fault surfaces and to reveal a third dimension for many measurements. In some locations this was not possible and only a two dimensional measurement of bedding or fault strike could be recorded. The flatness of most of the field area makes these two dimensional measurements unusually reliable.

Individual colored map units are used for exposures of the Ocotillo Formation, Holocene dune fields, and undifferentiated lacustrine and fluvial sediment. Because the Brawley Formation is so extensive in the area, it is in all other locations that are not specified. Conglomerates of at least 1 m thickness or a thick series of thinly bedded conglomerates distinguishes the Ocotillo Formation. Dune fields are identified as a concentration of large dunes that form a dune field expansive enough to be identified at 1:24000. Fluvial and lacustrine deposits are undifferentiated with some exceptions including a spit and some beach deposits (Plate 1).

Any photographs from the field that were used to create mosaics were combined using Adobe Photoshop. Photographs of the same outcrop or screen shots with overlap

were all opened with Photoshop. The tool in File>automate>photomerge was used and the default settings applied to the photomerge. New images were flattened and saved for editing in Adobe Illustrator.

Structural Analysis

Fault and fold data were recorded using colored lines on both paper and digital maps. All data were compiled into Google Earth. Imagery of the field area is of such high quality and shows the structural geology in such detail that photogeologic mapping formed the bulk of the structural map of the area (Plate 1). Susanne Janecke's field work and photogeologic mapping at the margins of the area, particularly in the northern and northwest part of the field area, were added to mapping by both Thornock and Janecke in the central areas. Modifications to the photogeologic map were made, in some cases, after field checking but persistent difficulties with the resolution and geographic grid of the basemap during the main field season limited the opportunity to do so. In most cases, field mapping confirmed photogeologic interpretations. There is such great complexity in this field area that the current geologic map (Plate 1) probably missed some structures.

Geologic and structural mapping methods were designed to answer our working hypotheses. Therefore, differentiating dextral faults from sinistral faults, and Holocene deformation from older structures was paramount. There are many north-south-striking normal faults in the field area but for simplicity we assigned these into dextral or sinistral groupings based on their local structural patterns (Plate 1). Red lines represent northwest-striking dextral faults and orange lines represent northeast-striking sinistral faults. Symbols and patterns are not available to modify the lines in Google Earth so

fault traces that are well exposed, partly covered or approximate are not differentiated (Plate 1). The great complexity of structures in the field area and difficulty of importing applicable symbology also contributed to our decision to map all faults with one continuous pattern. Folds were mapped using light blue lines for synclines and darker blue for anticlines. Monoclines were mapped with parallel anticline and syncline symbols along the fold axes.

An early set of strike and dip symbols exported from ArcGIS to Google Earth were too small and thin to see at the resolution needed for our study. A larger bold-lined strike and dip symbol was created in Illustrator, saved as an .svg file and imported into ArcGIS. The new symbol was applied to the strike and dip data in ArcGIS and rotated clockwise based on the strike of the bedding plane and labeled with the dip value. Once exported the strike and dip symbols appear in Google Earth in the correct location. Those symbols that did not rotate correctly, possibly due to input errors, were removed.

Faults are expressed in the field area in several ways. Some exposures reveal three-dimensional fault surfaces that can be measured while others only suggest the presence of a fault. Fault expressions that allow for direct measurement of a fault surface include linearly truncated beds, linear changes in strike or dip, and fault scarps that typically allow for both strike and dip to be measured or at least estimated. Other indirect evidence may indicate the exact location of a fault but provide little information about the dip direction or dip amount. Examples include aligned features such as vegetation, dunes, drainages, and changes in cover (like color or type of sediment that is not directly faulted). Because of the flat topography and the steep dip of most faults, the trends of

lineaments are accurate measures of fault strike. Dip measurements cannot be obtained from these features with a few exceptions of low angle faults.

Other evidence suggests the presence of faults but does not reveal the precise location of a fault. Examples include folds, changes in topography, and changes of sediment or bedding attitude across a broad boundary like a wash. These features typically form immediately adjacent to faults but in some cases the faults are not visible. Folds are particularly useful in determining where a fault might be. In some cases where faults have produced adjacent folds, the faults are roughly perpendicular to the fold axes. Stepovers along strike-slip faults have this geometry (Fig. 8). Another common association between faults and folds is a monocline or fold with at least one unusually steep limb that lies parallel to a strike-slip fault.

Another line of evidence that has variable reliability for locating faults is the presence of deformation bands in the Brawley Formation. Deformation bands are often found associated with and have a similar orientation to a larger fault. Sometimes there is no identifiable fault near the deformation bands.

Folds are initially identified by a lateral change in dip and/or strike of bedding from either imagery or field measurements. Faults can cause the strike and dip changes as well, so the only reliable method for locating folds is by tracing continuous bedding as it wraps around the fold axis and collecting strikes and dips. Most easily identifiable folds in the area are anticlinal folds such as domes. Structural lows are often more subtle due to sediment fill and cover. Some synclinal axes are assumed to exist between structural highs. For example, two domes that are near each other probably have a

Figure 8: Schematic figure showing how contraction develops between en echelon strands of strike-slip faults. Contraction occurs at locations of overlap between strands of sinistral right-steps or dextral left-steps. A) Map of the Extra fault zone that shows examples of contraction forming folds between strands of right-stepping left-lateral faults. B) A map of the Extra fault zone showing the location of part A. C) A 3D cartoon illustrates a simplified possible relationship of en echelon fault strands. The blue section is a more typical example of a fault dipping toward and into the main strand at depth. The yellow limb may dip or be vertical but encounters a detachment horizon and connects with the main fault at a normal angle. Over time the primary fault surface at depth may grow to the surface and cut the folding and subsidiary faults. See also Sharp (1967). D) Map view of part C.

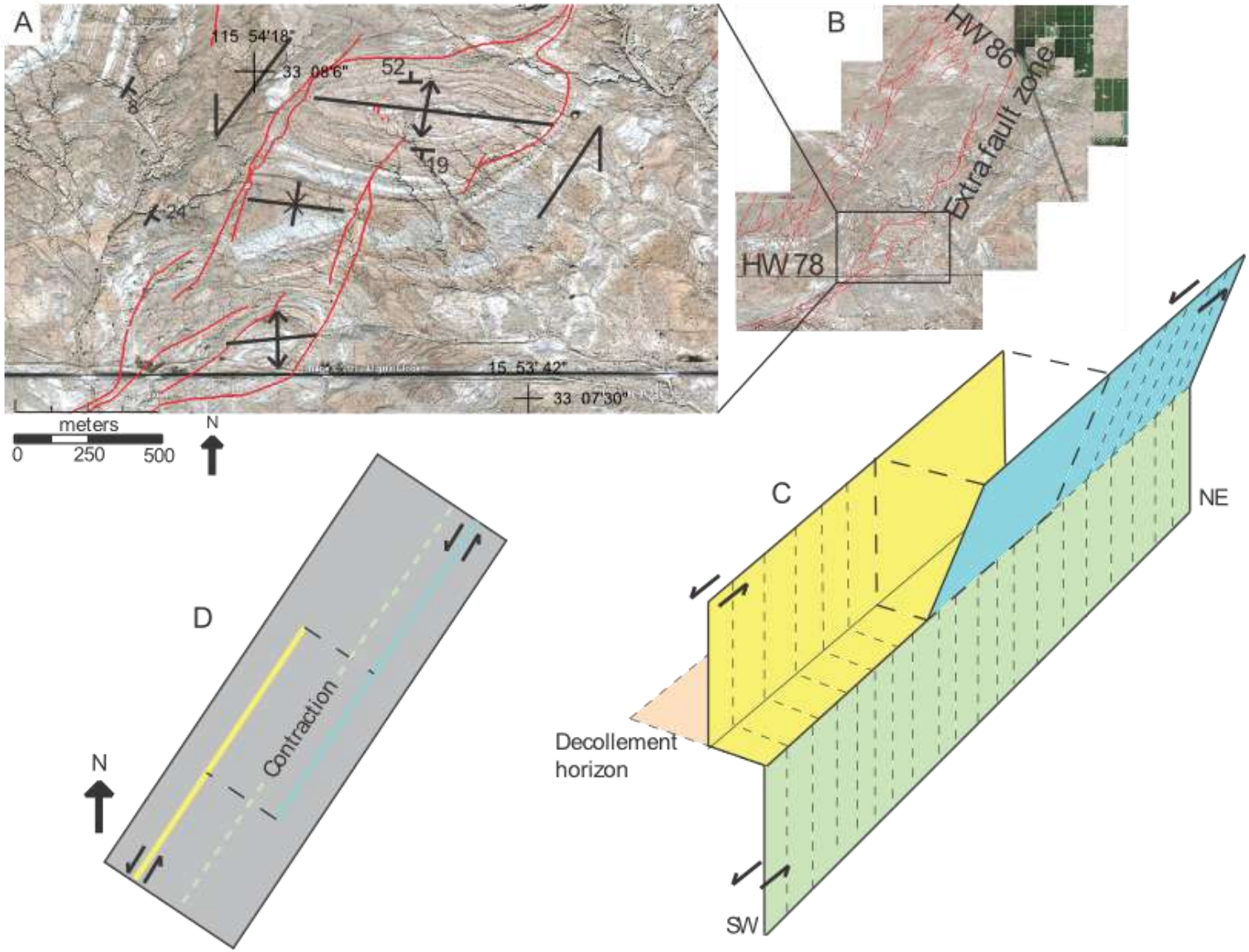
A
115 54'18"
33 08'6"
52
19
24
15 53' 42"
33 07'30"
meters
0 250 500
N
B
HW 86
Extra fault zone
HW 78
C
NE
SW
Decollement
horizon
D
N
Contraction

synclinal axis separating them. Alternatively, adjacent anticlines may be separated by a fault.

Marker beds were critical for differentiating folds, fault and for measuring separations across faults. Strike and dip measurements show whether the fold is a synform or an antiform. Abrupt terminations in marker bed also reveal the location of faults. Detailed mapping of marker beds is an essential aspect of structural mapping in this area, particularly because of the flat topography and light cover that obscure the structures in the field. Bedding is traced using aerial and satellite photography, primarily in Google Earth. Beds are most easily traced along sharp contacts at the top or bottom of the bedding surface with beds of a different sediment type. The two respective beds should be thick enough that they are laterally extensive and distinctive enough to follow through various structures. Most marker bed contacts are between light color, fine-grain marl beds and darker color mudstone or sandstone all in the Brawley Formation. Yellow lines are used as a default color for any marker bed in Plate 1. Some distinct and unique markers are easily traceable through many structures. To distinguish those marker beds from others, other colored lines are used.

Variation in strike direction of fault zones was first identified in photogeologic interpretation. Variations were also identified in the field with strike measurements on fault planes. Measurements for the rose diagrams and determining region boundaries were collected in Google Earth using the ruler tool. The ruler tool was drawn over sections of previously mapped faults and the azimuth direction for that section was recorded. Measured sections of the faults were a minimum of 500 meters long in an

attempt to avoid minor subsidiary structures that are unrelated to the fault zones. Regions were identified by dominance of strike direction.

Elevation and distance estimates were all made in either GeoMappApp or Google Earth. Both programs report location and elevation data for the current position of the cursor. Distance was primarily determined with the measure tool in Google Earth. Length units can be selected from a drop-down box and the user draws either a straight line or a line with several nodes and the distance is reported.

Geophysical Data and Analyses

Various types of geophysical data were compiled and analyzed in this study. No original geophysical data were collected, however, much of the data display and analysis is original. Data used in this study include earthquake focal data, aeromagnetic, gravity, Landsat and Interferometric Synthetic Aperture Radar (InSAR) data (Lyons and Sandwell, 2003; Mellors and Boisvert, 2003; Van Zandt et al., 2004; Lundgren et al., 2009; Wei et al., 2009). Gravity, magnetic and InSAR data were analyzed in pre-processed image format (Biehler and Rothstein, 1979; Langeheim and Jachens, 1993; Lyons and Sandwell, 2003; Mellors and Boisvert, 2003; Van Zandt et al., 2004; Fialko et al., 2005; Lundgren et al., 2009; Wei et al., 2009).

Microseismic data in this study are used primarily from Hauksson et al. (2012) and focal mechanism data from Yang et al. (2012). Yang et al. (2012) analyzed a large catalog of relocated focal mechanisms for southern California using the HASH method (Hardebeck and Shearer, 2002, 2003). Data were collected from 1981 to 2012 and processed using cross-correlation and a double-difference approach (Yang et al., 2012).

The recording stations were unevenly distributed, consisting of 160 broadband stations and 132 short-period stations by the end of 2008 (Hutton et al., 2010; Yang et al., 2012). The Hauksson et al. data set has been submitted to Bulletin of the Seismological Society of America (BSSA) but details of processing are currently unknown.

The focal mechanisms and microseismic relocated epicenter data were downloaded from the Southern California Earthquake Center (SCEC) as text data (available at http://www.data.scec.org/research-tools/alt-2011-yanghauksson-shearer.html) (Yang et al., 2012). Data were unzipped and opened in Notepad, a text-editing program. Data was then copied and a special paste applied to Microsoft Excel to set cell widths, separating the data into columns. Most of the cells were deleted leaving only the location data for both data sets and year, magnitude and depth for the seismic data and only the year, strike, dip and rake for the focal mechanisms. The data were cropped to the region around the field area for easier processing. The focal mechanisms span from 1984 to 2003 (Yang et al., 2012).

Data analyses were performed primarily in two programs, Environmental Systems Research Institute's (ESRI) Geographic Information System (GIS) and GeoMapApp. In both programs the spreadsheet data are easily entered and the location data read by the program; automatically displaying point vector data. Symbology modification was complicated and took significant amounts of time because of the large quantity. Both programs can also export to .kml Google Earth format but the GeoMapApp does so as a single image that retains its size and background. ESRI's GIS exports it with each point as its own entity that can be selected and modified. However the symbology becomes

corrupted in the conversion process. The most reliable export is of image files directly from GIS that retain all symbology and background.

The software Abel3 was used to plot epicenters in three dimensions. Epicenters were plotted with latitude and longitude for X and Y coordinates and depth in the Z direction in kilometers. However depth was dramatically compressed so the plot was not to scale vertically. To measure dip direction of epicenters on seismic lineaments, the latitude/longitude and depth scales were resolved and the depth plot stretched accordingly. Lines were then drawn in Adobe Illustrator that constrained the maximum and minimum of possible dip directions.

Landsat images from the Landsat 7 satellite before 2003 were downloaded and processed to highlight different kinds of rock and sediment. Images were edited for color variation using Adobe Photoshop 4.0. Multiple combinations of color bands were used in an effort to find the best combination to differentiate rock types and landforms. Most units within the field area are similar enough that only a few colors represent all the rock units. The images are used primarily as base maps since the resolution is not sufficient for most aspects of this study.

MORPHOMETRIC DATA SETS

Variations in the landscape play a crucial role in interpreting the structure of the field area because active deformation of the smooth bed of Lake Cahuilla has produced many tectonic uplifts, drainage anomalies, and dune fields on and adjacent to faults and folds. Data were collected from locations based on relation to a fault or fault zone and were not collected everywhere. Data include heights of dunes and dune fields, aerial

expanse of dune fields, incision of gullies, lengths of drainages controlled by faults, offset amount of faulted gullies, and thickness of lacustrine and plutonic beach deposits.

Identifying Holocene faulting can be difficult because most of the Quaternary rocks and sediments in the field area are unconsolidated or weakly consolidated (Dibblee, 1954, 1984; Kirby et al., 2007; this study). The best evidence of Holocene tectonic activity is made evident by fault scarps, offset streams, and faults that cut suspected or dated late Holocene sediment (Figs. 9, 10, 11). Stream terraces and anomalous stream paths and deltas indicate Holocene uplift in the area (see Sebastian uplift below).

Several criteria were used to identify the presence of Holocene sediment. The stratigraphic position at the top of the exposure, an angular unconformity with underlying tilted Pleistocene sediment, minimal tilts, localization along modern washes as terraces or along topographic contours as nearshore or beach deposits, and the character of the sediment itself are the most reliable ways to identify probable Holocene deposits. Most Holocene deposits are very poorly consolidated in contrast to the Pleistocene Brawley Formation, which varies from poorly to well consolidated. Accumulations of rounded plutonic pebbles are among the youngest Holocene deposits, and probably formed in beaches along the shores of Holocene Lake Cahuilla. Small pebble deposits can be up to a meter thick and are moderately extensive. Identifying structures in these deposits is difficult because they are not cemented. In some cases the pebble deposits are truncated against fault scarps but determining if the pebble deposit was faulted or deposited against the older fault scarp can be difficult.

Figure 9: Tectonic control of geomorphology. A) A section of the Bondit fault zone that exhibits examples of tectonic geomorphology. B) The same location as A but with interpretive annotations. There are several linear features indicating fault control on drainage patterns but two sections of washes show good examples of abrupt bends and linear control by faults. The fault is evident between the two linear sections, beheading or disrupting drainage patterns but is not as easily identifiable. Solid red lines are drawn on linear sections of gullies. Dashes lines are drawn where other, less prominent linear features are evident. Blue lines are drawn in some gullies to show beheading or changes in incision across the fault.

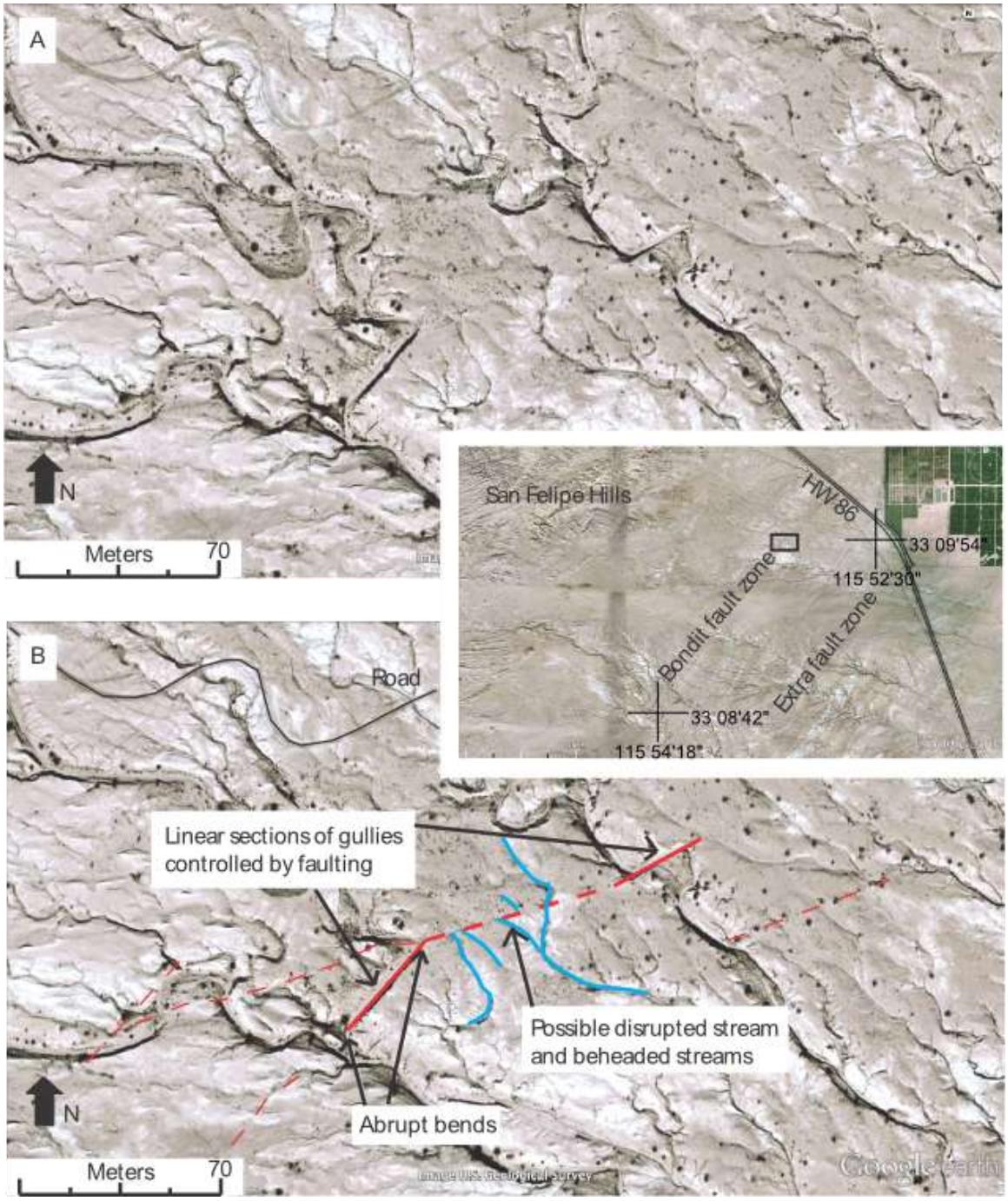
A
N
Meters
70
San Felipe Hills
HWY 86
33 09'54"
115 52'30"
Bondit fault zone
Extra fault zone
33 08'42"
115 54'18"
B
Road
Linear sections of gullies
controlled by faulting
Possible disrupted stream
and beheaded streams
Abrupt bends
N
Meters
70
Google Earth

Figure 10: Three examples of the Extra fault zone that show Holocene activity. Red lines indicate faults, yellow for bedding surfaces and green for unconformities. A) Photograph from N 33°08'53.5" and W 115°53'08.8" and is the most obvious fault that cuts Holocene sediments. Note the dip of the angular unconformity and Holocene sediments. Also an older fault terminates into the unconformity. B) A location of the fault about 150 meters south of highway 78 and, similar to part A, shows slight reverse motion on the fault. C) An exposure at 8-mile wash that has been an age constraint from radiocarbon and OSL results (Table 2).

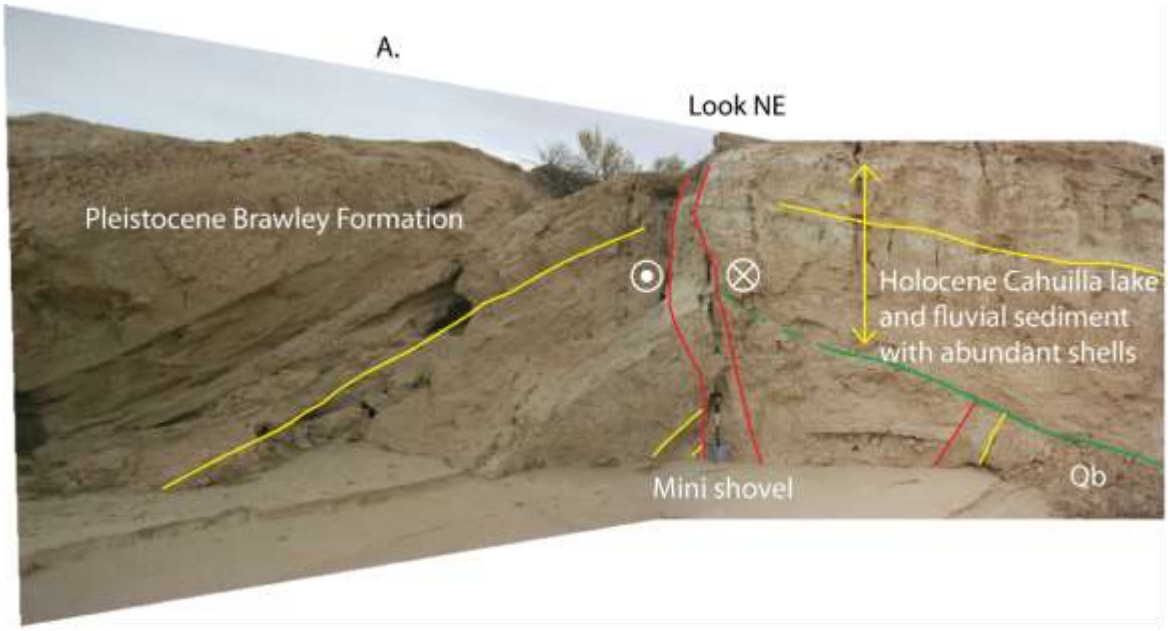
A.
Look NE
Pleistocene Brawley Formation
Holocene Cahuilla lake and fluvial sediment with abundant shells
Mini shovel
Qb

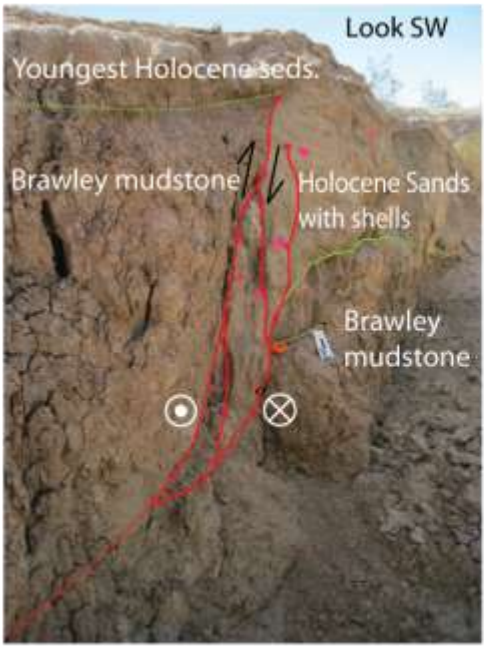
Look SW
Youngest Holocene seds.
Brawley mudstone
Holocene Sands with shells
Brawley mudstone

B.


Look SW
C.
Holocene Dunes
Cahuilla lakebed
colluvial wedges
Holocene Dunes
Brawley Mudstone

Figure 11: Optically Stimulated Luminescence (OSL) sample collection locations. A) OSL sample number USU 932 that was collected from the footwall of an Extra fault strand using standard OSL collection procedures. Notice the light L-suite sands of the collection site that sits in angular unconformity above the Brawley Formation darker mudstone. B) The collection location of sample number USU 933 collected from a horizon that directly overlays last offset of this strand of the Extra fault and near the radiocarbon sample location. Part C is a location map of the two samples.


look SE
A
OSL sample number USU 933

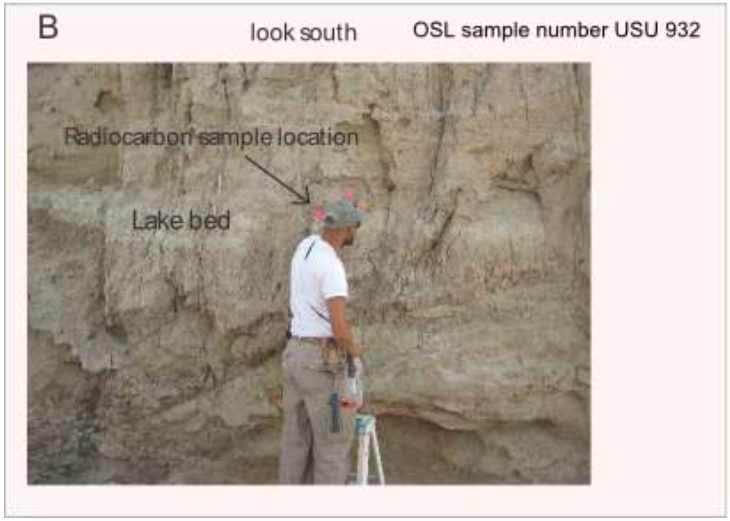
B
look south
OSL sample number USU 932
Radiocarbon sample location
Lake bed

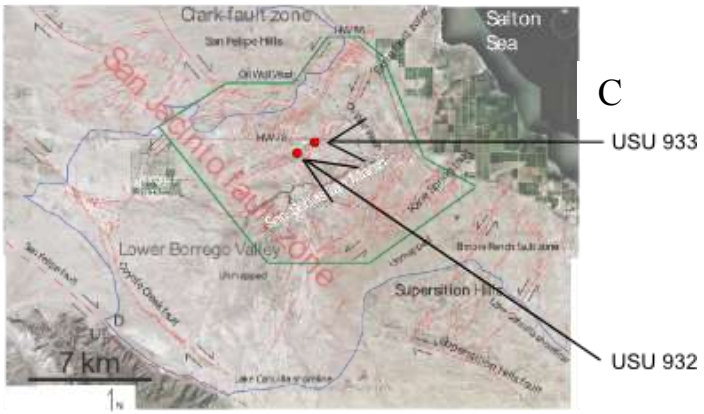
Clark fault zone
Salton Sea
C
USU 933
USU 932
Lower Borrego Valley
Superstition Hills
7 km

Gastropod shells are common in the Holocene sediment in the area and nearly absent in the underlying Pleistocene deposits, possibly due to dissolution of calcite in the older lacustrine sediment. Mollusk and other types of fossil shells are far less abundant but also present. The shells were deposited during cycles of Holocene Lake Cahuilla and are one of the key ways to identify Holocene deposits. The shells are generally small and easily confused with large light grains of sand or pieces of evaporites. Shells are reworked into younger fluvial deposits along washes and shells are often concentrated in paleo-stream deposits. Therefore, deposits with shells in them must be the same age or younger than the lake that was home to the gastropods. We were careful to ensure that the shells are imbedded into the sediment before assigning a Holocene age. Most Holocene deposits in the area do not have readily obvious shells.

Color can also be helpful in determining Holocene sedimentation since Lake Cahuilla interbeds often have a green-grey hue and most Holocene dune sediments are dominated by light-colored L-suite sand and the Brawley Formation is generally darker with a subequal mix of L-suite and orange to red C-suite (Kirby et al., 2007). The Cahuilla lacustrine interbeds are typically about 15 cm thick and alternate with the mica rich L-suite sand interbeds.

Cross-bedding structures in thick-bedded sand with concentrations of mica on the slip surfaces that highlight the steep cross beds (Kirby et al., 2007) indicate dune deposits. Sand dunes are uncommon in the Brawley Formation in this area (Kirby et al., 2007), sand dunes are more likely to be Holocene, especially if there are modern dune fields nearby. Mostly thick sand deposits are related to very young dune fields.

In almost every case the Holocene deposits are flat lying and undeformed. When cut by younger faults, the Holocene sediment is typically offset only a small amount and remains horizontal. Along some faults with large amounts of Holocene activity, like the Extra fault zone, Holocene sediments are tilted slightly near the faults and bend back to horizontal within several meters from the fault. Besides these subtle folds near the most active faults, we identified no other evidence for folding of Holocene sediments. Any faults within these flat lying, L-suite-dominated, unconsolidated sediments are assumed to be active in the Holocene. Thick units of unconsolidated sand are also considered Holocene and any faults that cut them have been active in the Holocene.

Most of the Holocene sediments from both Lake Cahuilla and sand dune interbeds are felsic (Winker and Kidwell, 1996) and unconsolidated. The very young age of the sediment and high concentration of quartz in the dune sand makes Optically Stimulated Luminescence dating ideal for the region. Only Holocene sands were dated to determine the age of most recent offset in fault zones.

Optically Stimulated Luminescence and radiocarbon samples were collected in some locations to confirm Holocene activity of the Extra fault zone (Fig. 11 and Table 2). Opaque aluminum tubes with rubber caps were used to prevent exposure to light. The tubes were hammered in until they were filled to capacity with sand-sized sediment. A sandwich bag and film canisters were also filled with sediment within 30 cm of the sample site. Photographs document the collection process and localities. Sampling

methods followed instructions provided by OSL lab personnel at Utah State University. Samples were prepared at the Utah State University OSL lab by lab assistants and myself. The sand was isolated and cleaned using appropriate lab techniques and tests were performed using small aliquots to determine the amount of time since last exposure to light.

TABLE 2: OSL AND RADIOCARBON DATES

OSL Age Information						
USU num.	Sample num.	Num. of aliquots 2	Equivalent Dose, De (Gy)3	Overdispersion (%)4	Dose Rate (Gy/ka)	OSL Age (ka)5
USU-932	EFZ-1	22 (32)	26.63 ± 4.18	31.9 ± 5.3	2.50 ± 0.13	10.64 ± 1.98
USU-933	EFZ-2	22 (58)	2.13 ± 0.86	39.8 ± 11.4	3.04 ± 0.16	0.70 ± 0.29

Evidence for faults in drainage networks

In areas of extensive Holocene cover, evidence of tectonic control in fluvial geomorphology contributes critical insights into structural relationships. We assume that faults that control geomorphology are relatively young and active in the late Pleistocene and maybe in the Holocene depending on their geomorphic expression. Overall, drainages within the area flow toward the San Sebastian Marsh in an irregular dendritic network. Deviations from a dendritic network indicate topographic, tectonic, eolian, or hydrologic barrier. Dune fields and topographic high areas mostly form on active

structures, and hydrologic barriers result from faulting and fracturing. Since topography is so smooth in the field area, we interpret most drainage anomalies as resulting from tectonic features. Anomalies include offset sections of drainages, beheaded streams and unusually straight and kinked drainages (Fig. 9). Drainage anomalies are most prevalent in fault zones with significant Holocene cover such as the northeast section of the Bondit fault zone and sections of the Sebastian fault zone (Figs. 7 and 9).

Deflected drainages can occur when a pre-existing fault creates a natural hydraulic barrier that changes the path of the drainage for some distance. Similarly, linear sections of washes can also be the result of a fault that strikes in the direction of general water flow that forms a linear segment of a gully without deflection. Although fault controlled, these linear sections of washes are secondary and only reveal the presence of the fault and do not require Holocene activity.

Beheaded drainages are different in that most cases they reveal a young relative age of the fault to the stream. A beheaded stream is a stream that is moderately well formed but abruptly terminates (Burbank and Anderson, 2001). Often these terminations are observed along a line, affecting several small drainages. The endpoints of the gullies typically form a line that represents a fault. Since the drainages are not controlled, simply cut, they are older than last activity on the fault. Sometimes the beheaded streams can be correlated and offset direction and magnitude determined; but more often there are too many small gullies that correlations are uncertain.

Aggradation and incision patters are also useful for identifying Holocene activity. Active faulting and folding within fault zones or on individual faults controls the amount

of incision of nearby gullies. In most areas with minimal faulting drainage incision is also minimal. The relationship may be directly related to the amount of dip direction offset on the fault zones. Single drainages can change from incision to aggradation laterally depending on proximity to different faults with varied amounts of dip slip.

RESULTS

Our results are organized into three main sections in order of structural, geophysical and morphometric findings. First, we document that the field area is dominated by northeast-striking left-lateral faults of the Extra fault array and the north-westernmost faults of the Elmore Ranch fault array (Fig. 5). We present first-order characterizations of the fault zones and present data about their dominant sense of slip. Other data were collected specifically to test the hypothesis that the Clark fault continues southeastward and to provide the critical tests of the hypotheses. The hypotheses and tests are laid out in Table 1 and Figure 6. Not all possible interpretations are tested equally because the available and growing data sets clearly contradicted some of our initial hypotheses. Further analysis was not needed in those instances. In other cases insufficient data were collected to uniquely interpret the data. Results of critical tests and preferred interpretations are more fully treated in the Discussion section.

The results are presented in the following order. We characterize the geometry and kinematics of the left-lateral faults in the field area and explore possible interactions with the Clark fault. After discussing the northeast-striking left-lateral faults, we present data from the small number of dextral faults in the field area. We then present geophysical results from the area including relocated seismic epicenters and hypocenters, focal mechanisms, InSAR data, and gravity data. Each geophysical data set indicates that a northwest-striking fault exists in the subsurface, below the faults of the Extra fault array. Finally we present morphometric findings from the field area that reveal a broad uplift that coincides with the Clark and Superstition Hills faults. Altogether the data

show that the Clark fault is active and continues to the Superstition Hills in the subsurface.

STRUCTURAL RESULTS

Northeast-striking left-lateral cross faults

The principal observation made during field mapping is that the northeast-striking left-lateral faults greatly outnumber the northwest-striking dextral faults in the field area (Plate 1). Fieldwork revealed that there is no continuous dextral fault that connects the Clark fault through the field area in the San Sebastian Wash area to the Superstition Hills fault (Plate 1). The only way for the Clark fault to continue to the southeast is as a blind fault in the subsurface or as a complex transrotational domain. The geometry could be something like the ones shown in figure 6 G. Critical tests and data, principally geophysical, constrain whether there is a large dextral fault zone at depth beneath the field area. Geophysical results are presented below.

Strike and dip measurements were made on almost every exposure of a fault plane uncovered or discovered in the study area (N=93) (Fig. 12). To the first order, the proportion of different fault strikes in this data set represents the proportion of each fault set in the field area (Fig. 12). Some bias is introduced by the dominant N-S trend of gullies on either side of San Felipe Wash because northeast-striking faults are more obvious in the gullies than northwest-striking faults. Some of the latter may have been overlooked in oblique exposures in gullies. The pronounced meanders in many gullies are likely to counteract this modest bias. Fault exposures that were only visible on gully

Figure 12: Stereographic representation of the orientation of measured faults planes from the field area. Points are the poles to each plane. Contour lines are plotted using the Kamb contouring method. The strongest orientations of the fault planes are shown with dark lines and a box showing the strongest point. One representative great circle is shown for NE- and NW-striking faults. A) All measured faults in the field area. B) All NE-striking fault measurements and C) shows NW-striking fault planes.

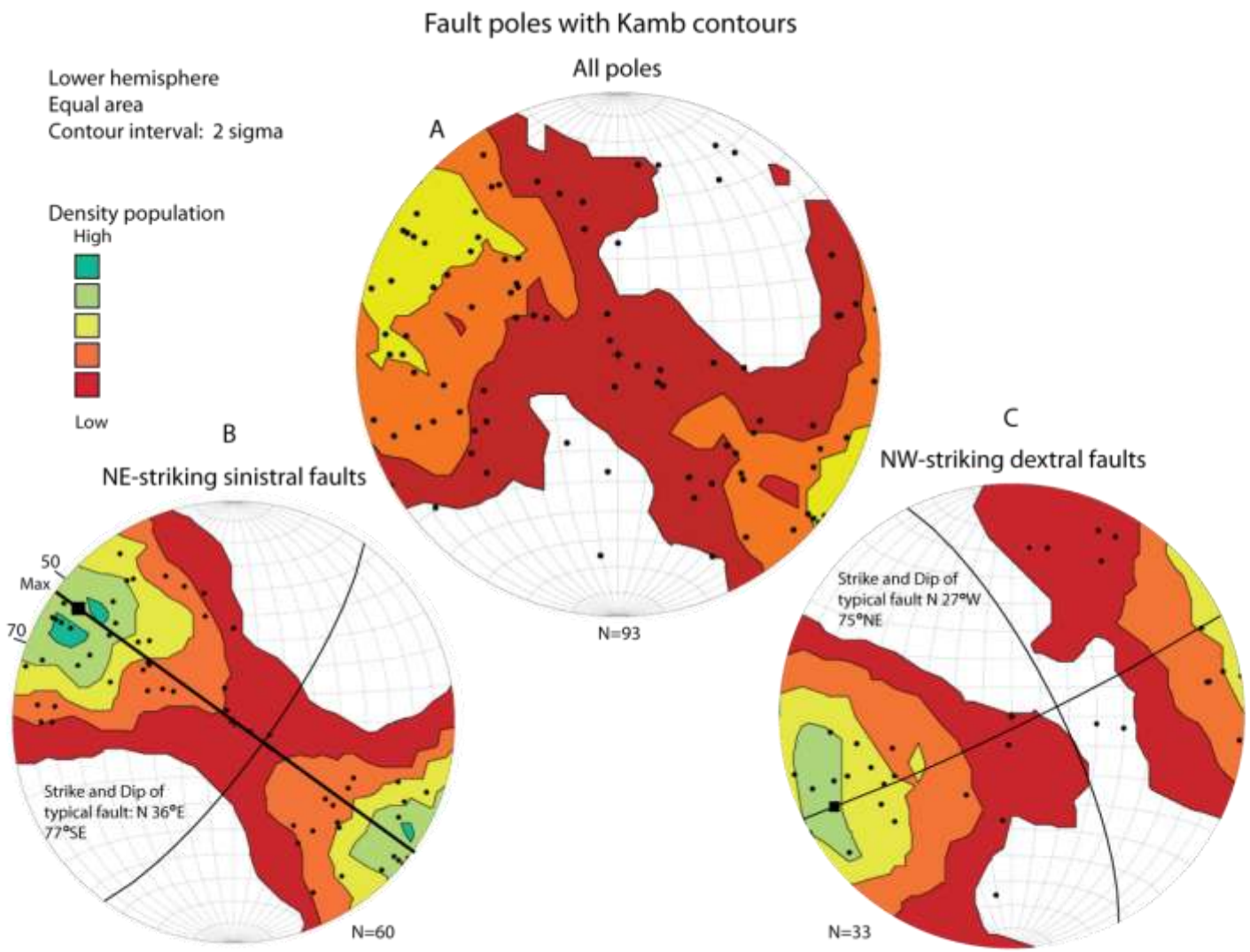
Fault poles with Kamb contours
Lower hemisphere
Equal area
Contour interval: 2 sigma
Density population
High
Low
All poles
A
N=93
B
NE-striking sinistral faults
50
Max
70
Strike and Dip of
typical fault: N 36°E
77°SE
N=60
C
NW-striking dextral faults
Strike and Dip of
typical fault N 27°W
75°NE
N=33

walls or on the pavement surface were not included in the following analysis due to lack of 3-dimensional characterization of the faults.

All the attitudes of fault planes were compiled and analyzed using OSX Stereonet (http://www.ux.uis.no/~nestor/work/programs.html). Of the 93 measurements with both strike and dip, 17 strike between 345-15° (Fig. 12). Those are distinct from the northeast and northwest-striking faults. Fifty-two have a strike between 15 and 80° azimuth and are considered "northeast-striking left lateral or left-oblique faults"; that is 56% (Fig. 12). The dominance of the left-lateral faults is also shown by the continuity of the fault zones of the Extra fault array. Northwest-striking faults in the area are discontinuous, truncated by the northeast-striking faults and are more sporadically distributed than the northeast-striking faults. The northwest-striking faults comprise 26% of the measured fault exposures (Fig. 12).

We split the northeast-striking left-lateral faults in the field area into three fault arrays referred to as the Extra, Elmore Ranch and Tarantula Wash fault arrays (Fig. 5). The three fault arrays are named for the most continuous and active faults zones within each array, namely the Extra fault zone and the Elmore Ranch fault zone, and for Tarantula Wash, which meanders through the eastern part of the Tarantula Wash array. The Extra and Elmore Ranch fault zones are separated across strike by ~12 km from one another but their subsidiary faults come within 1 km of one another (Fig. 5). Only a few left-lateral fault zones of the Elmore Ranch fault array are within the field area but the entire width of the Extra fault array is in the field area (Fig. 5). The Elmore Ranch and Extra fault arrays are similar in spanning large lateral distances (along strike) whereas the

Tarantula Wash array connects adjacent strands within the Clark fault zone and is therefore a much more local fault array.

The mode of faulting within the fault arrays appears to be primarily sinistral slip that is conjugate and subsidiary to the northwest-striking dextral faults in the region (Sanders et al., 1986; Hudnut et al., 1989a; Sharp et al., 1989; Yang et al., 2012; this study). Evidence for this left-lateral sense of slip includes focal mechanisms, offset features, structural relationships, slickenline measurements, and the minimal topography across the fault zones (Hudnut et al., 1989a; Sharp et al., 1989; Kirby, 2005; Yang et al., 2012; this study). The Extra and Elmore Ranch fault arrays appear to be continuous between the Coyote Creek, Superstition Hills fault and the Brawley seismic zone, but Holocene cover sequences and the Salton Sea obscure about 4-8 km of the Extra fault zone (Fig. 5; Hudnut et al., 1989a; Sharp et al., 1989; Brothers et al., 2009; this study). We report on each left-lateral fault array and fault zone from northwest to southeast.

The Tarantula Wash fault array

The Tarantula Wash fault array is a series of northeast-striking sinistral cross faults around the Tarantula Wash (Fig. 5; Kirby, 2005; Janecke, unpublished mapping). The faults form cross structures between the Squaw Peak strand of the Coyote Creek fault strand (Steely, 2006; Janecke et al., 2010) and the central Powerline strand of the Clark fault (Plate 1; Fig. 5). The Tarantula Wash fault array is southwest of the San Felipe Hills strand of the Clark fault and it probably absorbs strain from the San Felipe Hills fault in a manner shown in Figure 13. If so, this is an example of a single dextral fault trace changing along strike into a ladder-like fault array (Fig. 13). There is a similar

Figure 13: Various geometries of cross fault relationships observed and hypothesized in the field area. Most of the cross faults represent structures that transition from one major dextral fault to a different dextral fault. Most cross faults form between master faults and develop a geometry that somewhat resembles a ladder.

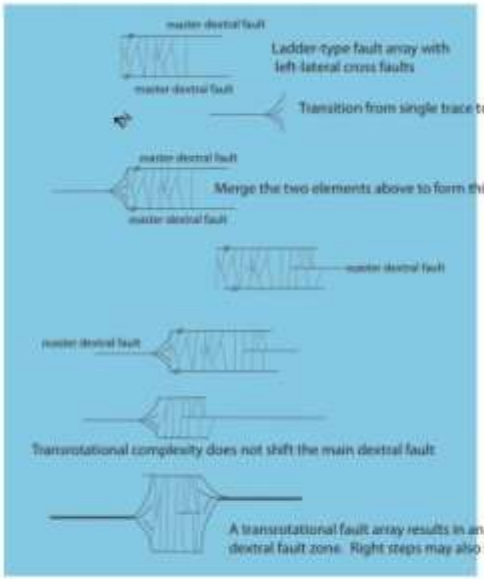
master dextral fault
Ladder-type fault array with left-lateral cross faults
master dextral fault
Transition from single trace to a ladder fault array
master dextral fault
Merge the two elements above to form this network of faults
master dextral fault
master dextral fault
Transrotational complexity does not shift the main dextral fault
A transrotational fault array results in an overall left step in the dextral fault zone. Right steps may also form in this way.


master dextral fault
subordinate dextral fault


A sheared version of the fault array in the left hand column that produces a deactivated upper dextral fault but retains an active lower dextral fault.
master dextral fault
master dextral fault
A sheared version of a fault array in the left hand column
master dextral fault

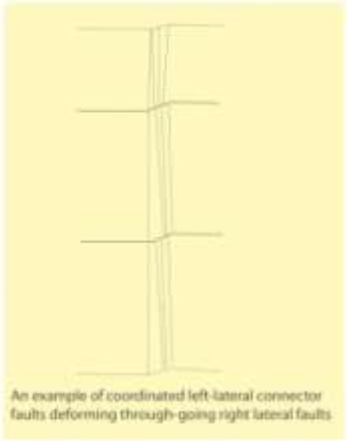
An example of coordinated left-lateral connector faults deforming through-going right lateral faults

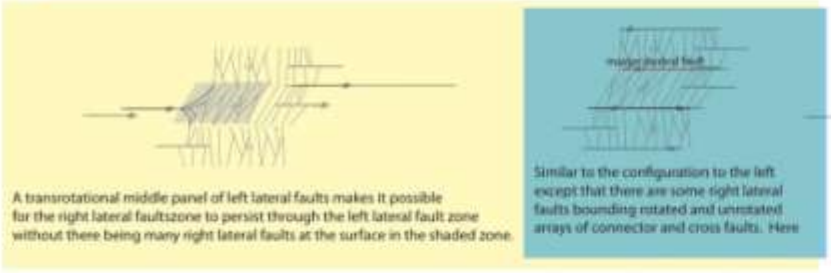
A transrotational middle panel of left lateral faults makes it possible for the right lateral faultszone to persist through the left lateral fault zone without there being many right lateral faults at the surface in the shaded zone.
master dextral fault
Similar to the configuration to the left except that there are some right lateral faults bounding rotated and unrotated arrays of connector and cross faults. Here


Left steps and then one right step along a dextral fault zone

Arrays with shearing and rotation of connector/cross faults


Arrays with through-going master faults

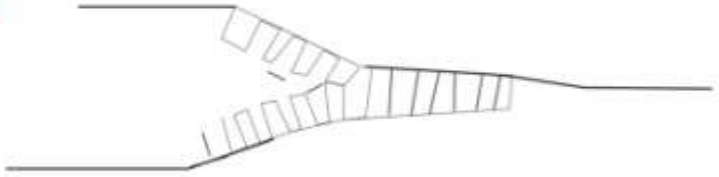
Zipper-style branch zone between two dextral fault zones

ladder-like fault array directly northeast of the Tarantula Wash fault array that lies between the dextral Powerline and Sand Dune faults (Fig. 1; Kirby et al., 2007; Janecke et al., 2010).

Microseismicity is dispersed beneath the eastern part of the Tarantula Wash fault array (Hauksson et al., 2012) (Figs. 5 and 14) and there is an alignment of small earthquakes with a northwest strike that crosses beneath several sinistral faults in the northern half of the array (Fig. 14). The spatial relationship between this possible dextral fault at depth and the fault that produces the Tule Wash dextral microseismic alignment farther north (Belgarde, 2007; Belgarde and Janecke, 2007), is right stepping.

The largest and most continuous left lateral fault of the Tarantula Wash fault array is the Allegretti Farm fault zone along its southeast margin. The Allegretti Farm fault is unique to this array in that it shows evidence for continuing southwest of the Squaw Peak fault zone for 4-5 km as far as a northwest-striking strand of the Coyote Creek fault zone that we here name Rockwell's fault (Fig. 7).

The Allegretti Farm fault is one of the more prominent left-lateral faults in the field area and the third of its fault trace that lies north of highway 78 was mapped by Reitz, (1977); Lilly, (2003); Heitmann, (2002); and Kirby (2005) (Fig. 15). It appears to intersect with and terminates into strands of the Coyote Creek fault at its southwest end but exposure there is poor and more field validation is needed to validate this preliminary interpretation from outside of the map area (Fig. 2). Northeast of the intersection with the Coyote Creek fault it consolidates into a narrow fault zone with only one or two strands evident north of Highway 78. It strikes about N 46° E toward the Powerline fault

Figure 14: Focal mechanisms in the region. A) All focal mechanisms in the region from Yang (2012). A distinct halo surrounds the field area with a stark lack of activity. Focal mechanisms that are present reveal strike-slip motion on faults during seismic rupture. B) Focal mechanisms created from data from Hauksson et al. (2011) online catalog available at http://www.data.scec.org/research-tools/alt-2011-yanghauksson-shearer.html. Only mechanisms near or related to the area are shown. Size varies relatively by magnitude with larger radii representing a larger magnitude earthquake. Focal mechanisms were made in a combination of OSX stereonet and Adobe Illustrator.

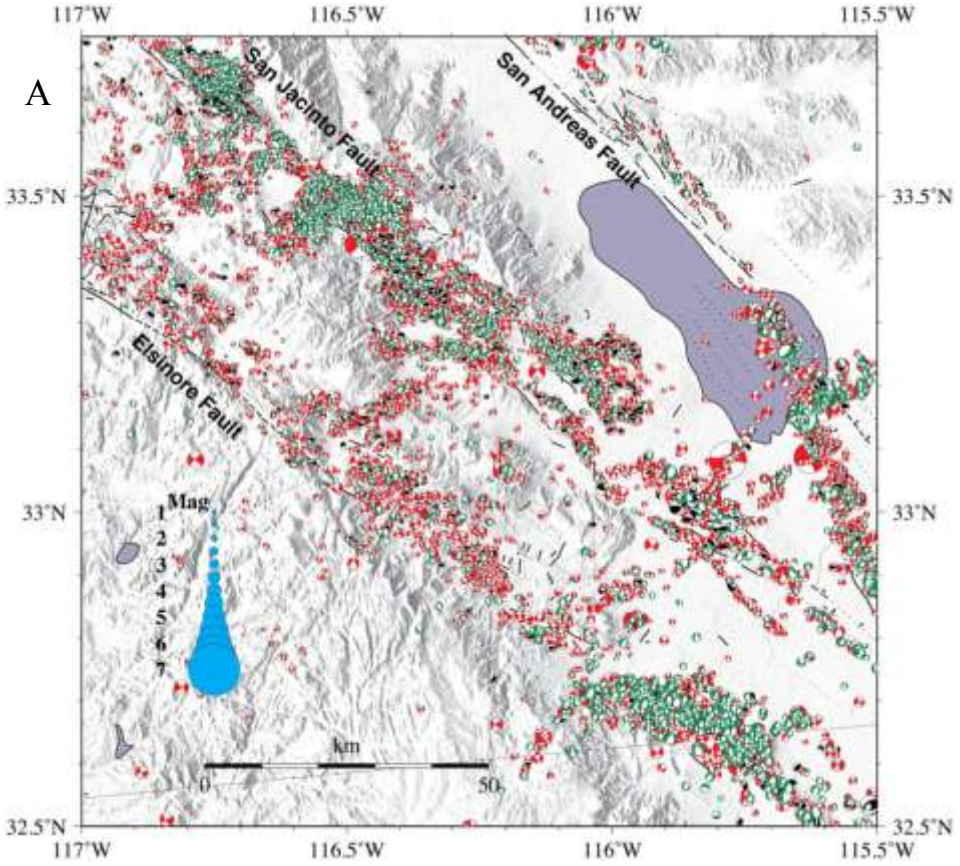
A
117°W
116.5°W
116°W
115.5°W
33.5°N
33°N
32.5°N
San Jacinto Fault
San Andreas Fault
Elsinore Fault
Mag
1
2
3
4
5
6
7
km
0
50

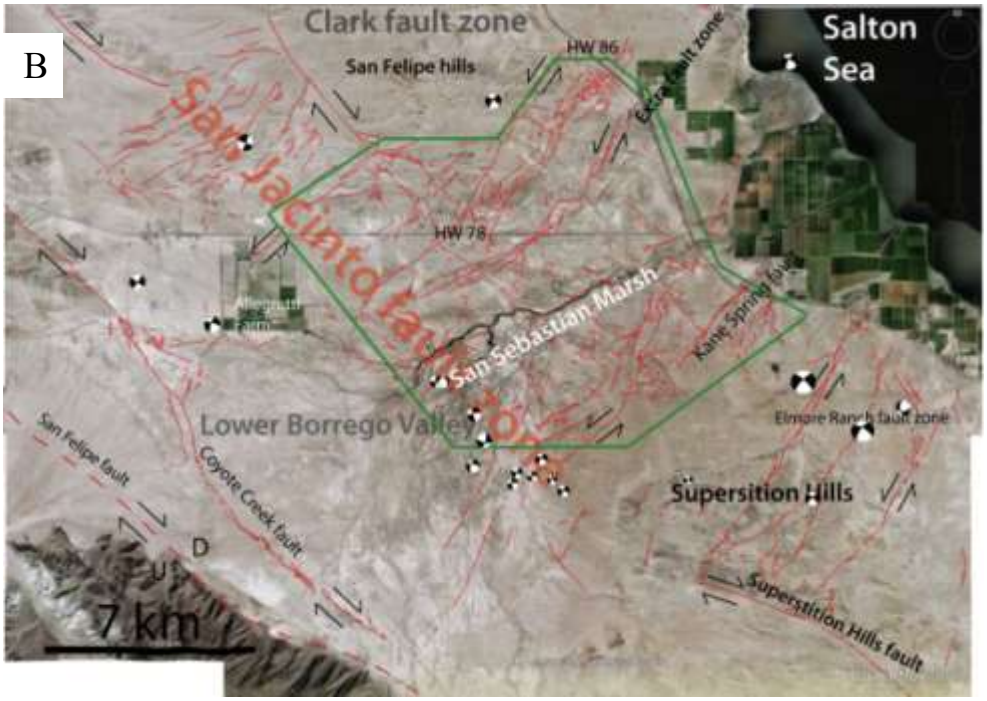
B
Clark fault zone
San Felipe hills
HW 86
Extra fault zone
Salton Sea
San Jacinto fault zone
HW 78
San Sebastian Marsh
Kane Spring fault
Elmore Ranch fault zone
Lower Borrego Valley
San Felipe fault
Coyote Creek fault
Superstition Hills
D
U
7 km
Superstition Hills fault

Figure 15: Interaction between the Powerline and Allegretti faults. The Powerline fault is in red and the Allegretti Farm fault is in blue. A) A reference map showing the location of the Extra fault zone and Allegretti Farm. B) Approaching each other the fault zones become less distinct, forming multiple synthetic strands in a branch geometry. Light blue and orange faults are smaller, representative faults of the Allegretti and Clark faults continuation respectively. C) The two faults intersect in the subsurface but propagate with only a portion of the strain they expressed as longer, more continuous strands.

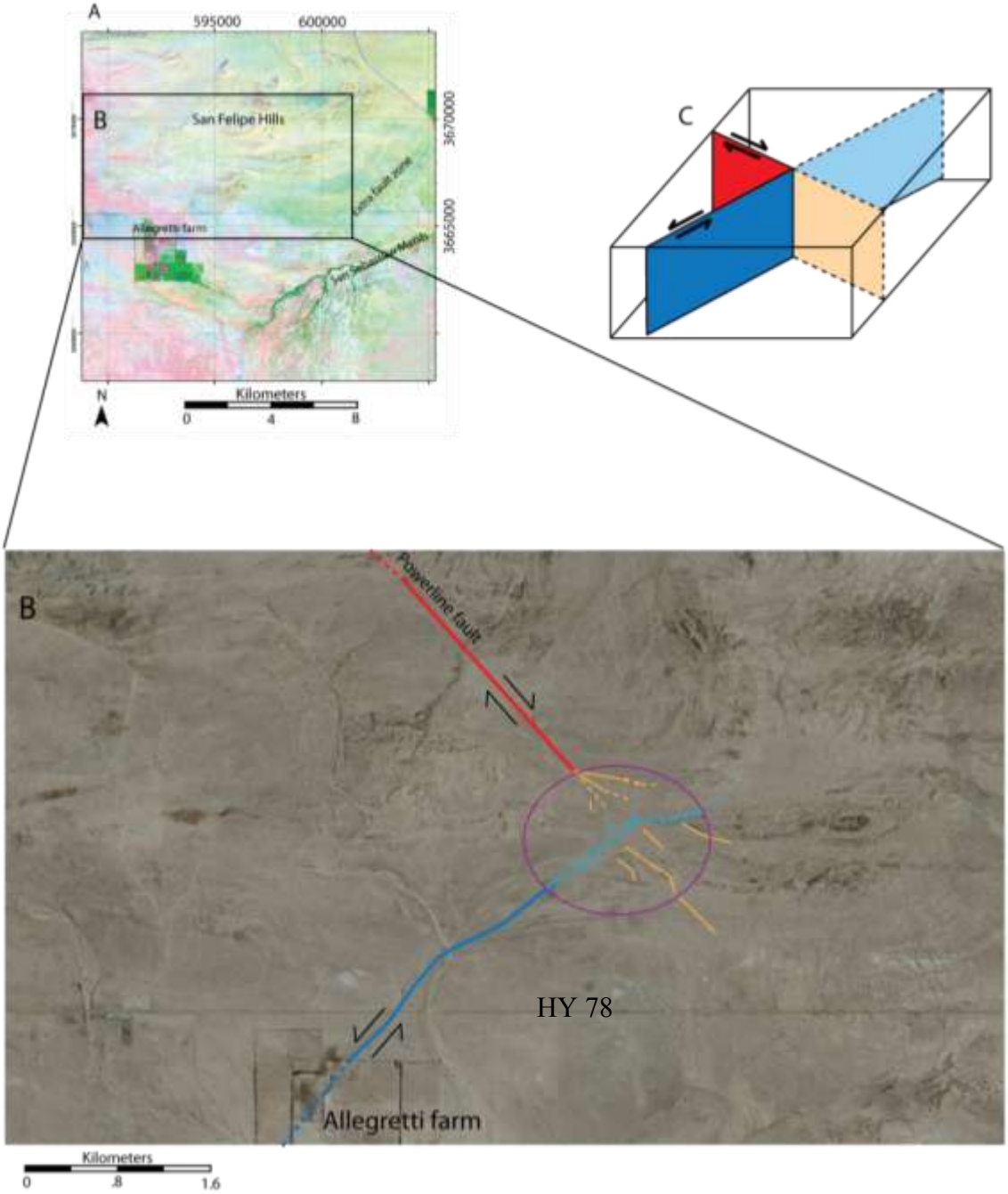
A
595000
600000
B
San Felipe Hills
Allegretti farm
3670000
3665000
N
Kilometers
0
4
8
C
B
Poppertine fault
HY 78
Allegretti farm
Kilometers
0
.8
1.6

up to a point within about 1 kilometer of the intersection of the two faults (Fig. 15). The relationship between the Allegretti Farm fault and the Powerline fault is discussed in more detail below.

The Extra fault array

The Extra fault array, between the Elmore Ranch fault array and the Tarantula Wash fault array, has a similar width and geometry to the Elmore Ranch fault array (Fig. 5). The only previously named fault zone within the Extra fault array is the Extra fault zone (Hudnut et al., 1989a; Kirby et al., 2007), and the only detailed map of the Extra fault zone was by Kirby (2005). He mapped 10 km of the fault zone between the Salton Sea and Highway 78. No other faults or sections of the Extra fault array were identified on previous maps.

There are six anastomosing fault zones in the Extra fault array and six in the Elmore Ranch fault array with enough continuity to be named (Fig. 7). Photogeologic mapping and the presence of aligned epicenters of earthquakes (Shearer et al., 2005; Lin et al., 2007; Yang et al., 2012) show that there are many NE-striking faults southeast of the Elmore Ranch fault array. The deep parts of these fault arrays were activated by the Westmoreland and Brawley earthquake swarms of 1981 and 2012, respectively (Fig. 14). The available reconnaissance maps of Dibblee (1984) did not identify the surface expression of the left-lateral faults there but Sharp et al. (1989) located a few of the fault traces. Earthquakes of the Brawley swarm of August 26th 2012 activated what may be the southernmost cross-fault array within this structural domain (Hauksson et al., 2012;

http://earthquake.usgs.gov/earthquakes/eqinthenews/2012/br awleyswarmAug/, accessed Jan 2, 2013).

The Extra fault array, like the Elmore Ranch fault array, is composed of northeast-striking left-lateral fault zones that span a length of ~7 kilometers perpendicular to its dominant strike. The Extra fault zone is the best developed and exposed of the faults in the Extra fault array and lies in the middle of the array (Fig. 7). The Extra fault zone is marked by at least a dozen en echelon structural highs whereas many of the adjacent left lateral faults have lower densities of domes along them (Dibblee, 1984a; Kirby et al., 2007; plate 1). An apparent exception to this rule is the Kane Spring fault, which has many domes along its trace. Other newly mapped and named left-lateral faults of the Extra fault array are (from northwest to southeast) the Shoreline fault, the Bondit fault zone, the East Extra fault, the Sebastian fault zone, and the Border Patrol fault (Fig. 7). Below are unique characteristics of several of these fault zones.

Shoreline fault

The Shoreline fault is one of the smaller-offset faults of the Extra fault array and defines the northwest edge of the array. It is a single fault with few subsidiary structures and a damage zone of varied width but no more than ~10 meters. The Shoreline fault is 6.5 to 8 km long and exhibits a fairly consistent strike of ~30° until it dies out into a fold close to Highway 86 in the northeast (Fig. 7). Exposures toward the southwest retain the 30° strike and parallels a long section of the ancient Lake Cahuilla shoreline (Fig. 2), providing the name for the fault. The Brawley mudstone and faults of the Shoreline fault are typically well exposed in the northeast until ~800 meters north of Highway 78 where

it intersects the Bondit fault zone (Fig. 7). At the intersection the Shoreline fault changes strike to follow the strike of the Bondit fault zone at ~55° (Fig. 7). The Shoreline fault is not a separate fault zone southwest of this branch point (Fig. 7).

Oil Well Wash provides one of the two excellent exposures of the Shoreline fault (Fig. 16A). The main fault parallels the strike of the stratigraphy on the west and obliquely truncates the folded beds to the east (Plate 1). The upper section of the beds on the east is vertical but shallows within about 3 meters, retaining a consistent dip toward the east. Most subsidiary structures are to the east of the main fault within the folded rock (Fig. 16A). The fault damage zone is ~3 meters wide at this location with some antithetic and synthetic faults (Fig. 16A). A second good exposure is about 1 km west of Highway 86 (Fig. 16B)

Bondit fault zone

Southwest of highway 86 the Bondit fault zone differs from other sections of the fault zone and from other fault zones in the Extra fault array. The Bondit fault zone has a thicker blanket of Holocene sediments covering part of its trace than the other fault zones of the Extra fault array with the exception of the Sebastian fault (Fig. 9). Along this section of the Bondit fault zone the geomorphic gully features are prominent and particularly important for fault identification (Fig. 9) (Plate 1). Most of the faults in this area deflect drainages and truncate bedding (Fig. 9) without developing many fault exposures at the surface. In areas where the fault zone is well exposed there are several prominent folds - mostly anticlines – that are typically cut by younger faults (Fig. 17A). The stratigraphy in the area consistently dips shallowly to the southeast when not folded

Figure 16: Three photographs of the Shoreline fault at different locations (see appendix A). A) View looking NE at an outcrop in Oil Well Wash. B) View looking NE near highway 86. C) View looking SW taken from the same location as B. All photographs are taken looking down strike of the fault. Red lines represent faults, yellow lines are bedding planes and blue circles are for highlighting scale items.

A

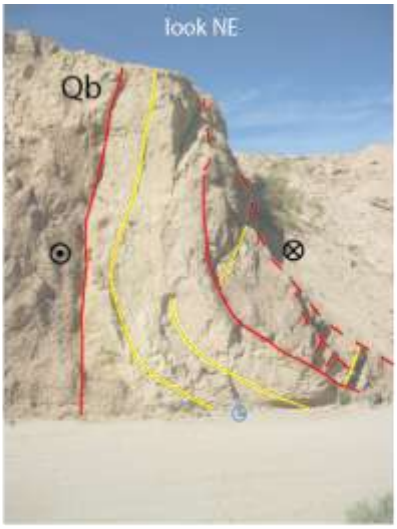

B

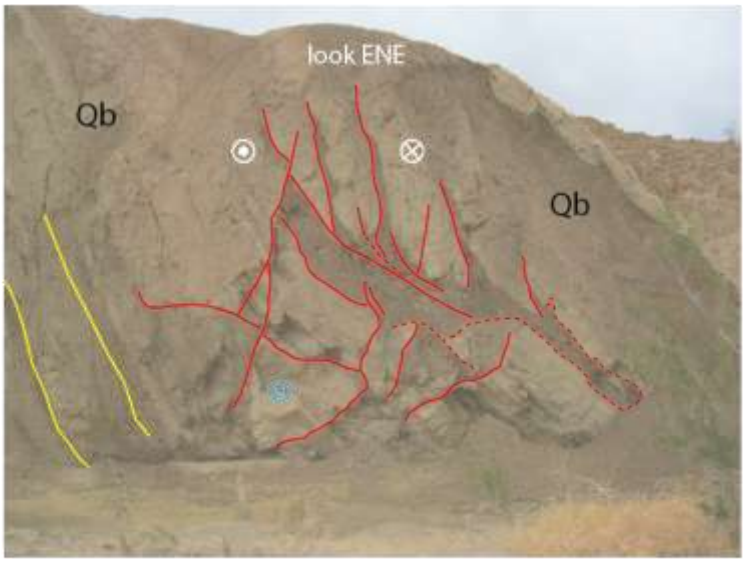

C

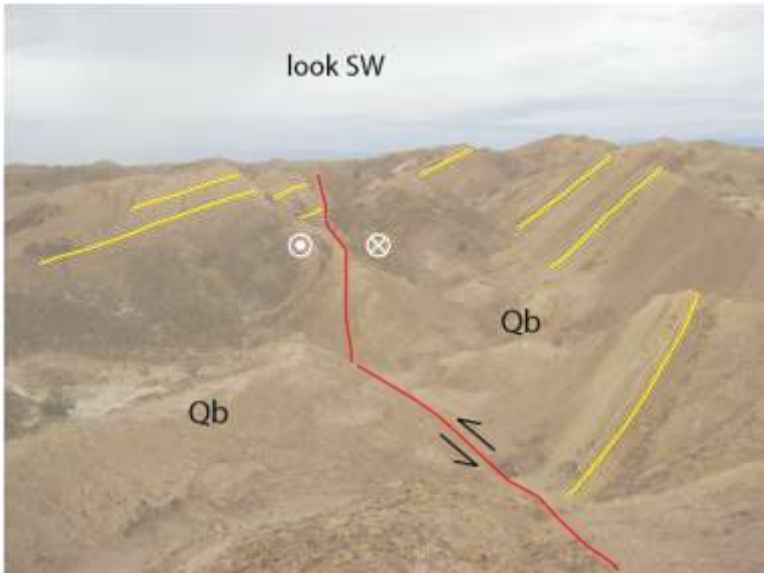

Figure 17: Cross section of the Bondit fault between HW 86 and HW 78. A) Location of the cross section line that trends NW, perpendicular to the Bondit fault zone. This area is highly faulted but only four prominent faults cross the line; other faults are insignificant or do not cross the line and are not included in the cross section. The aerial photograph is from Google Earth but is modified for color. B) Location map within the Bondit fault zone. C) A cross section of the Bondit fault zone with colors of strata that correlate to units in this cross section only. There is no vertical exaggeration on the cross section.

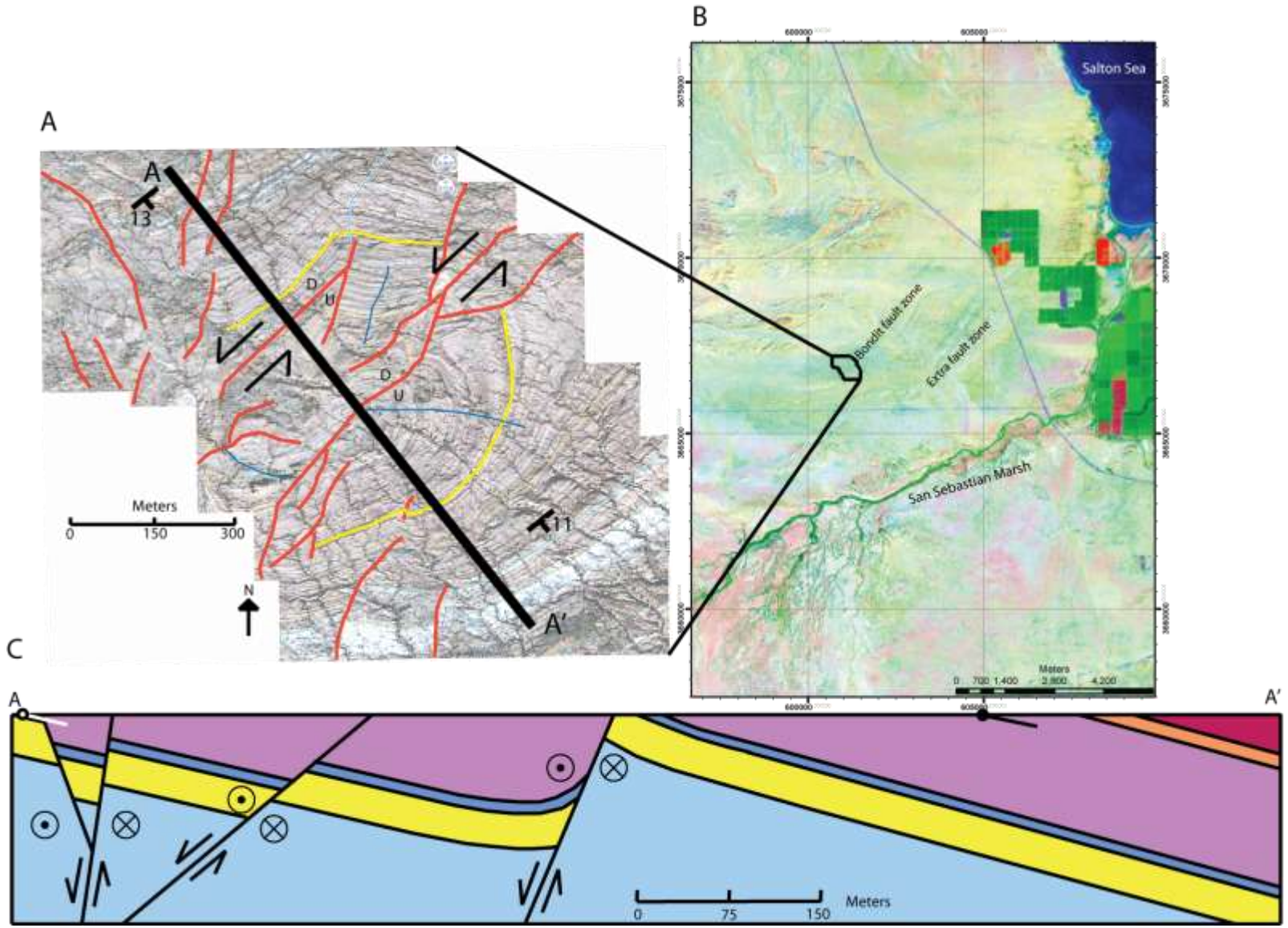
A
A
13
D
U
D
U
Meters
0
150
300
N
11
A'
B
Salton Sea
Bombay fault zone
Extra fault zone
San Sebastian Marsh
Meters
0
700
1,400
2,800
4,200
C
A
A'
Meters
0
75
150

(Fig. 17A). Most faults are easily identifiable between Highway 78 and Oil Well Wash but almost all exposures require digging a hole to determine dip direction due to only shallow incision of the gullies.

Pavement exposures remain clear until ~400 meters south of Highway 78 (Fig. 7; Plate 1) where the fault zone narrows into fewer strands that are parallel to the southwestern section of the Extra fault (Fig. 7). Holocene sediment obscures the faults toward the southwest but sand dune, drainage and vegetation lineaments indicate that it continues (Plate 1). Exposures of the fault zone are straighter and much more continuous than fault exposures northeast of Highway 78 (Plate 1). Anticlines that form in the southwest section are much smaller than those formed north of Highway 78 and are generally cut by the faults (Plate 1).

The trace of the Bondit fault is difficult to locate on the surface southwest of Tarantula Wash, however there is an obvious continuation in InSAR datasets. Vincent (2000) and Wei et al. (2009) show the southwestward continuation of the Bondit fault for another 4.5-6 km. Analysis of this InSAR images shows that the Bondit fault produced a barrier to groundwater and defines a strong N40°E-striking boundary of subsidence that is centered on water wells in Allegretti Farm (Vincent, 2000; Fialko, 2006; Wei et al., 2009) (Fig. 2 and 18 A). The Bondit fault ends in the southwest where it intersects the Rockwell's fault (see Fig. 32 A).

Within the Bondit fault zone is a noteworthy large strike-slip fault that dips shallowly to the southeast in Oil Well Wash (Fig. 19 A). Offset markers are difficult to locate on either side of the fault because it is grossly parallel to bedding in both the

Figure 18: InSAR images over the field area. A) An InSAR image modified from Mellors and others (2005). B) An InSAR image from Fialko (2006). These authors placed original hypothesized active faults between the Superstition Hills fault (SHF) and the Clark fault (labeled as SJF or San Jacinto fault). A map of epicenters that correlates with both reference boxes on the InSAR images (A and B). Notice in C how well the hypothesized location of the fault from InSAR and the fault revealed by the earthquake epicenter swarm (D) agree spatially. D) A zoomed map view of the 2008 swarm event outlined on C.

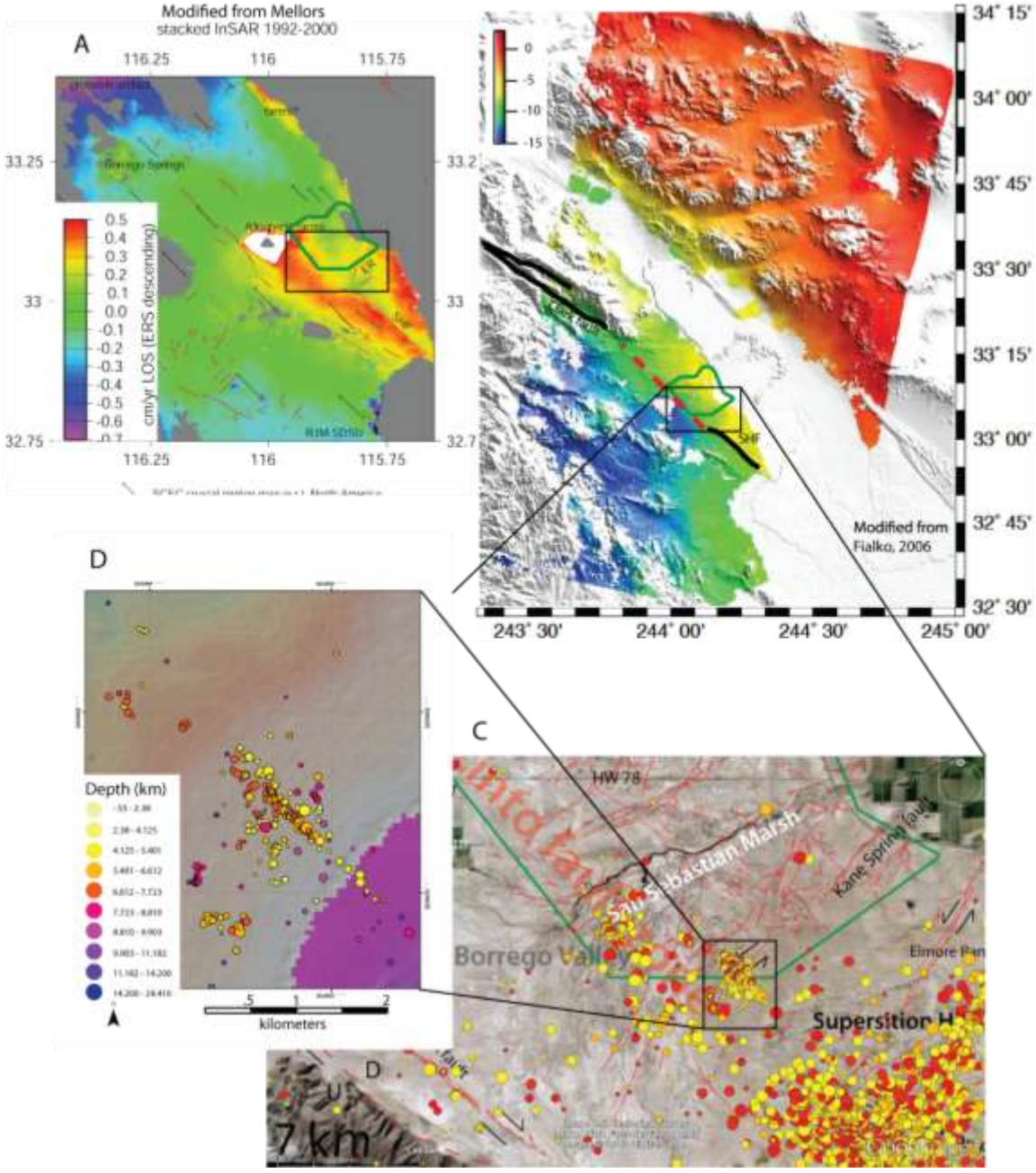
Modified from Mellors
stacked InSAR 1992-2000
A
116.25
116
115.75
33.25
33.2
33
32.75
32.7
cm/yr LOS (ERS descending)
0.5
0.4
0.3
0.2
0.1
0.0
-0.1
-0.2
-0.3
-0.4
-0.5
-0.6
0
-5
-10
-15
34° 15'
34° 00'
33° 45'
33° 30'
33° 15'
33° 00'
32° 45'
32° 30'
243° 30'
244° 00'
244° 30'
245° 00'
Modified from
Fialko, 2006
D
Depth (km)
kilometers
C
HW 78
Borrego Valley
Kane Spring fault
Elmore Ran
Supersition H
D
7 km

Figure 19: Photographys of a shallowly dipping fault. A) Photograph mosaic of the shallowly dipping fault in Oil Well Wash. Susanne Janecke is on the left of the photograph for scale. Red lines indicate fault surfaces. Many more faults are evident in the mudstone above the main trace that are not indicated on the photograph. Photograph was taken looking down strike to the NE. B) The same fault that is in A but taken near highway 86. The photograph is taken looking SW just a little oblique of strike. A hammer is used for scale and is circled in green.

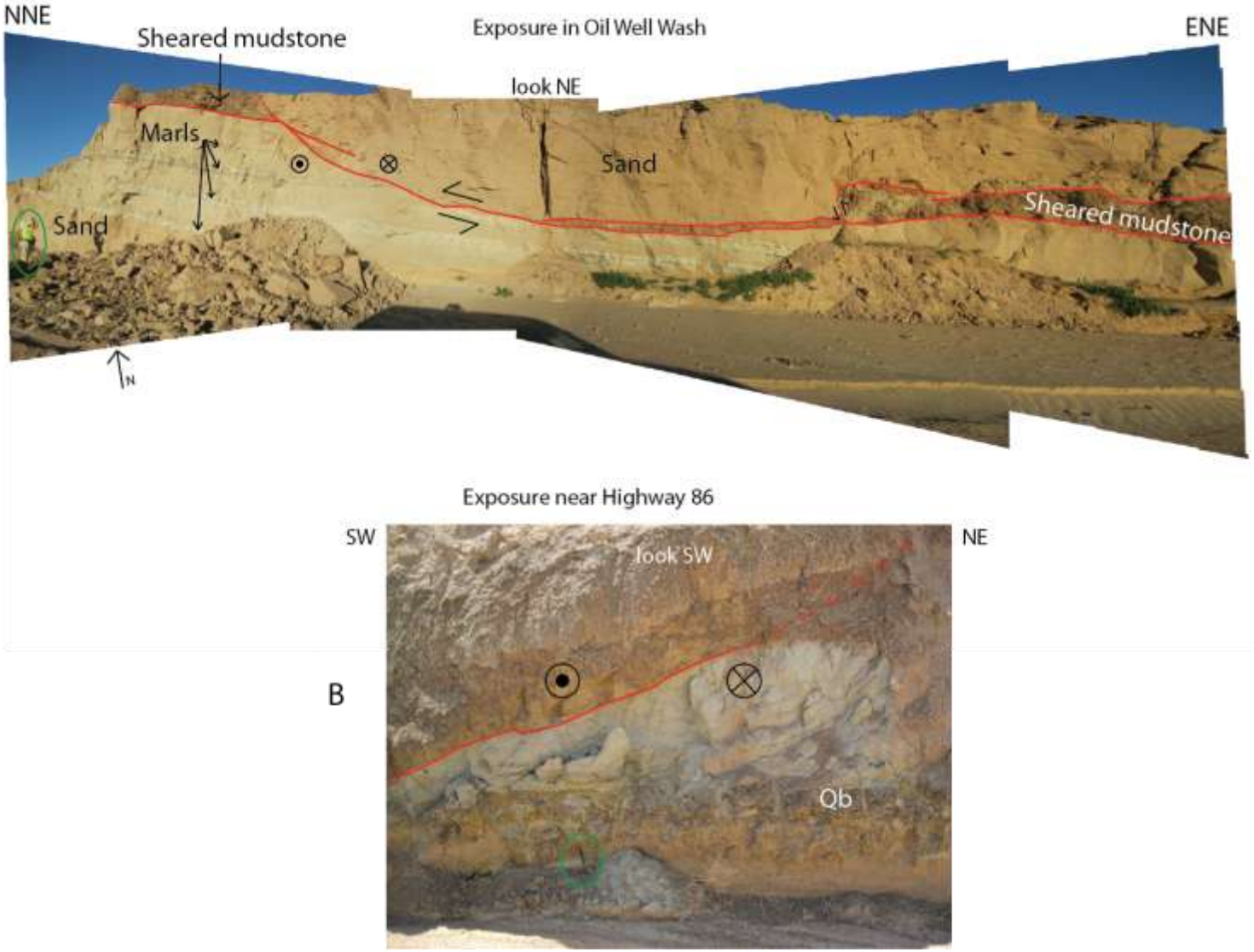
A
NNE
Sheared mudstone
Exposure in Oil Well Wash
look NE
ENE
Marls
Sand
Sand
Sheared mudstone
N
Exposure near Highway 86
SW
NE
look SW
B
Qb

footwall and hanging wall. Another clear exposure near Highway 86 is in the man-made ditch (Fig. 19 B) with several other poor exposures of the fault between Oil Well Wash and the ditch (Fig. 19; Plate 1). The exposures in the ditch dip shallowly to the southeast.

Extra fault zone

The Extra fault zone differs from the other faults in the array because it links directly to the southernmost tip of the San Andreas fault according to Hudnut et al. (1989) or may come close enough to modulate the stress there (Brothers et al., 2009, 2011). The Extra fault zone is the most prominent and identifiable of faults in the Extra fault array (Plate 1) and cuts Holocene sediment in more places and has more fault scarps than any other strands in the Extra fault array. It is consistently a structural and topographic high (Fig. 20).

Northeast of highway 78 and southwest of highway 86 the Extra fault zone is ~0.8 km wide, well exposed, exhibits doubly-plunging anticlines, deep (~6 meters) incision into the Brawley Formation and several en echelon right step-overs (Plate 1, Fig. 21). At least six anticlines and four very well formed domes are expressed in this short span between the two highways (Plate 1; Fig. 21). Between highway 86 and the Salton Sea there are another 4-5 domes along the continuation of the fault zone. Exposure is spotty there and this limits detailed structural analysis of the northeasternmost part of the Extra fault zone onland.

Three washes within the field area provide good exposures of the Extra fault zone. One location ~150 meters south of highway 78 shows all the major strands of the Extra fault zone shows several smaller faults close together within a single gully (Fig. 22). At

Figure 20: A DEM over the Extra and Bondit fault zones. Notice the several topographic highs along the Extra fault zone. The topographic highs correlate with the structurally high Extra fault zone. The contour interval is 5 meters and the DEM was exported from GeoMapApp into Google Earth for combination with faults.

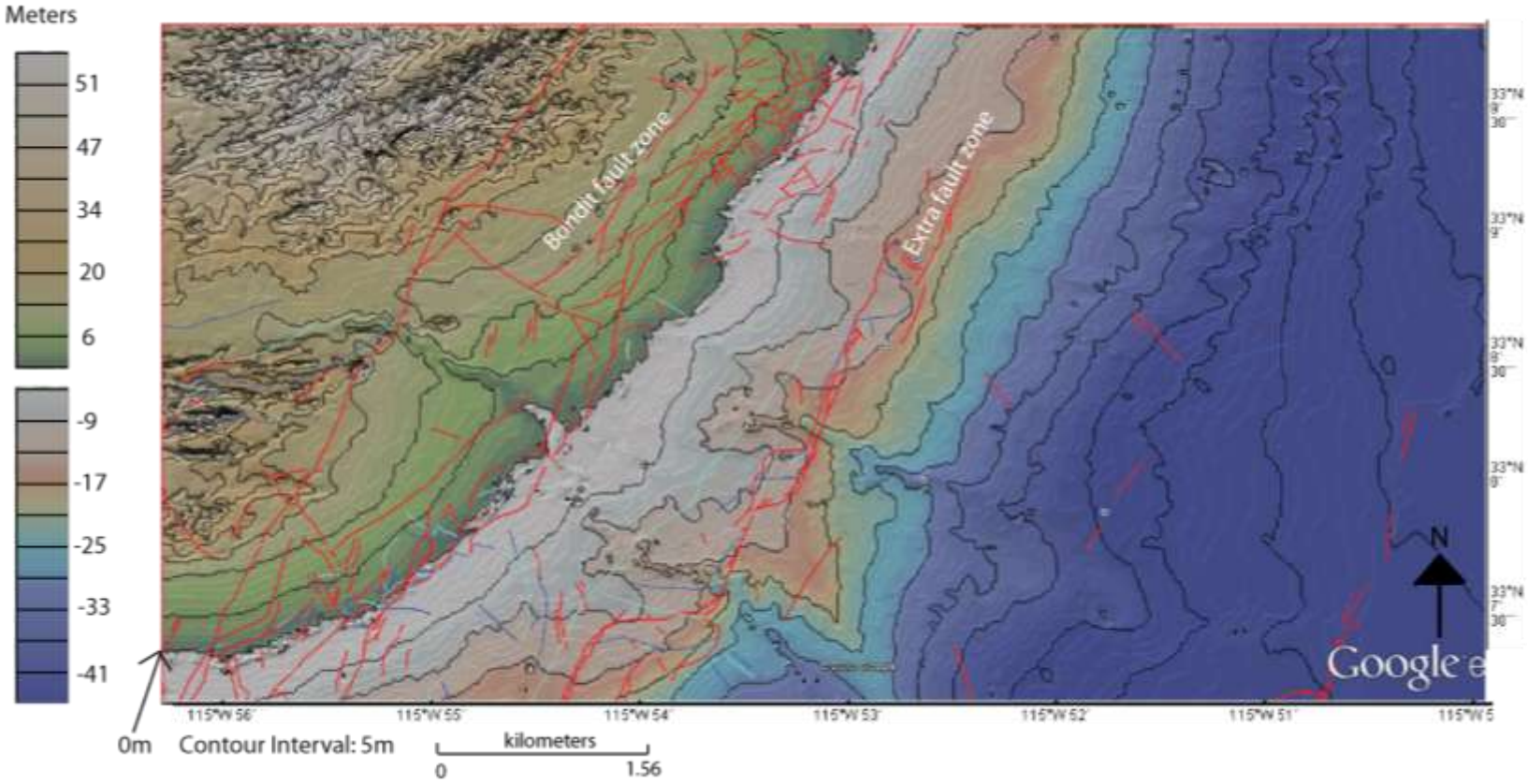
Meters
51
47
34
20
6
-9
-17
-25
-33
-41
Bonanit fault zone
Extra fault zone
N
Google e
115°W 56'
115°W 55'
115°W 54'
115°W 53'
115°W 52'
115°W 51'
0m
Contour Interval: 5m
kilometers
0
1.56

Figure 21: A cross section in the Extra fault zone. A) A map showing the location of part B. B) Annotated Areal image indicating the location of the cross section perpendicular to the Extra fault zone. The four largest faults are represented on the cross section. Other smaller faults are not included because of minimal effect on the stratigraphy at this scale. C) A cross section of the Extra fault zone. Notice the reverse motion on the faults as opposed to most other faults in the region that exhibit normal-oblique motion. Units and colors are used to correlate stratigraphy in this cross-section only and the tan color below is undifferentiated Brawley Formation. There is no vertical exaggeration on the cross section.

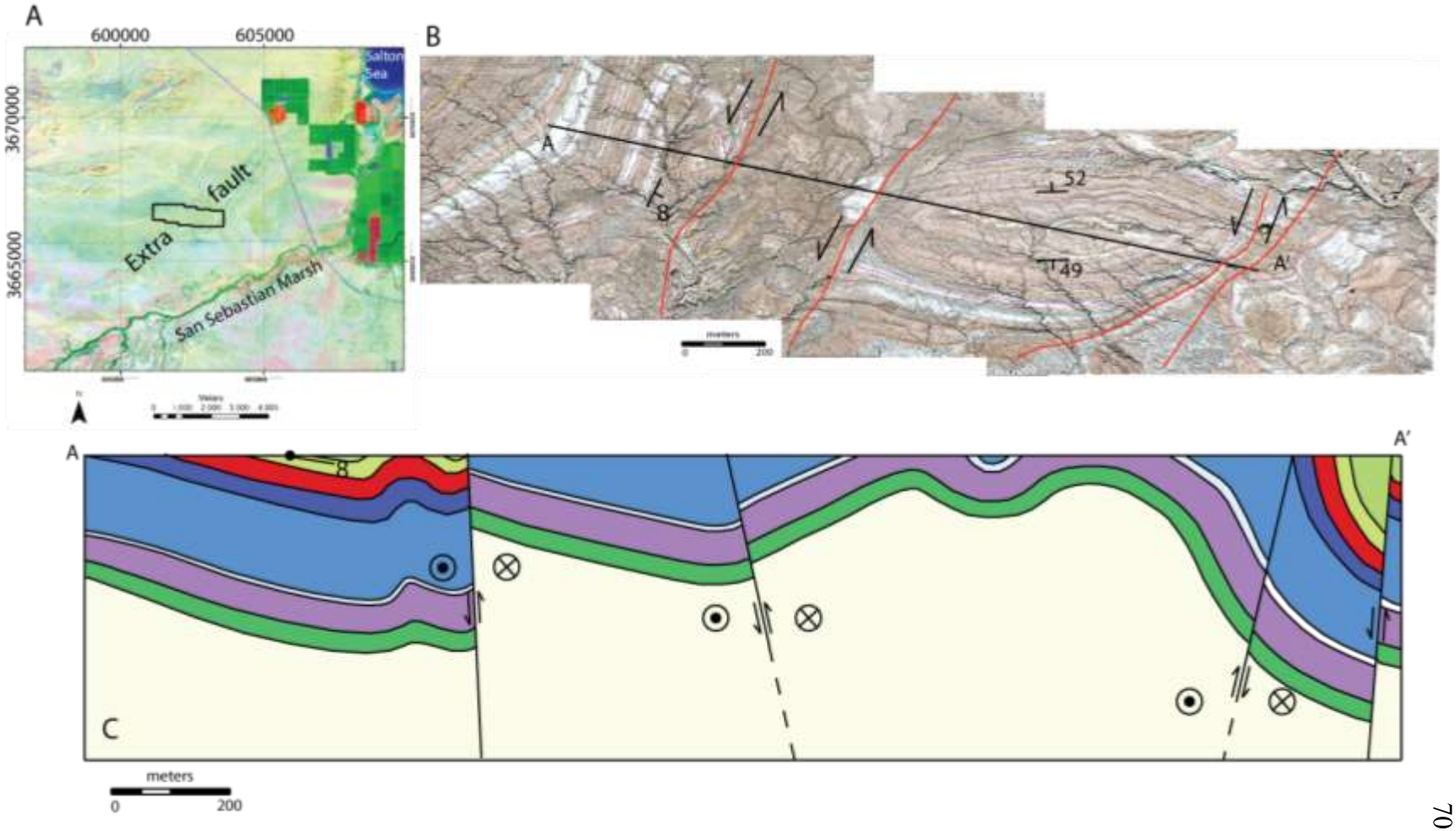
A
600000
605000
3670000
3665000
Salton Sea
Extra
fault
San Sebastian Marsh
B
A
8
52
49
A'
meters
0
200
A
A'
8
C
meters
0
200

Figure 22: A series of photographs of the Extra fault zone that were all taken within a short distance in one gully about 150 meters south of Highway 78. A) A reference map that shows a grading color line from 0 meters to 155 meters with boxes that show locations of photographs. B) Photographs view looking toward the south with lines connected to boxes that are at the same location on the color line as the boxes in part A. C) Photographs view looking at the north side of the gully with lines connecting to the remaining boxes on the distance (color) line.

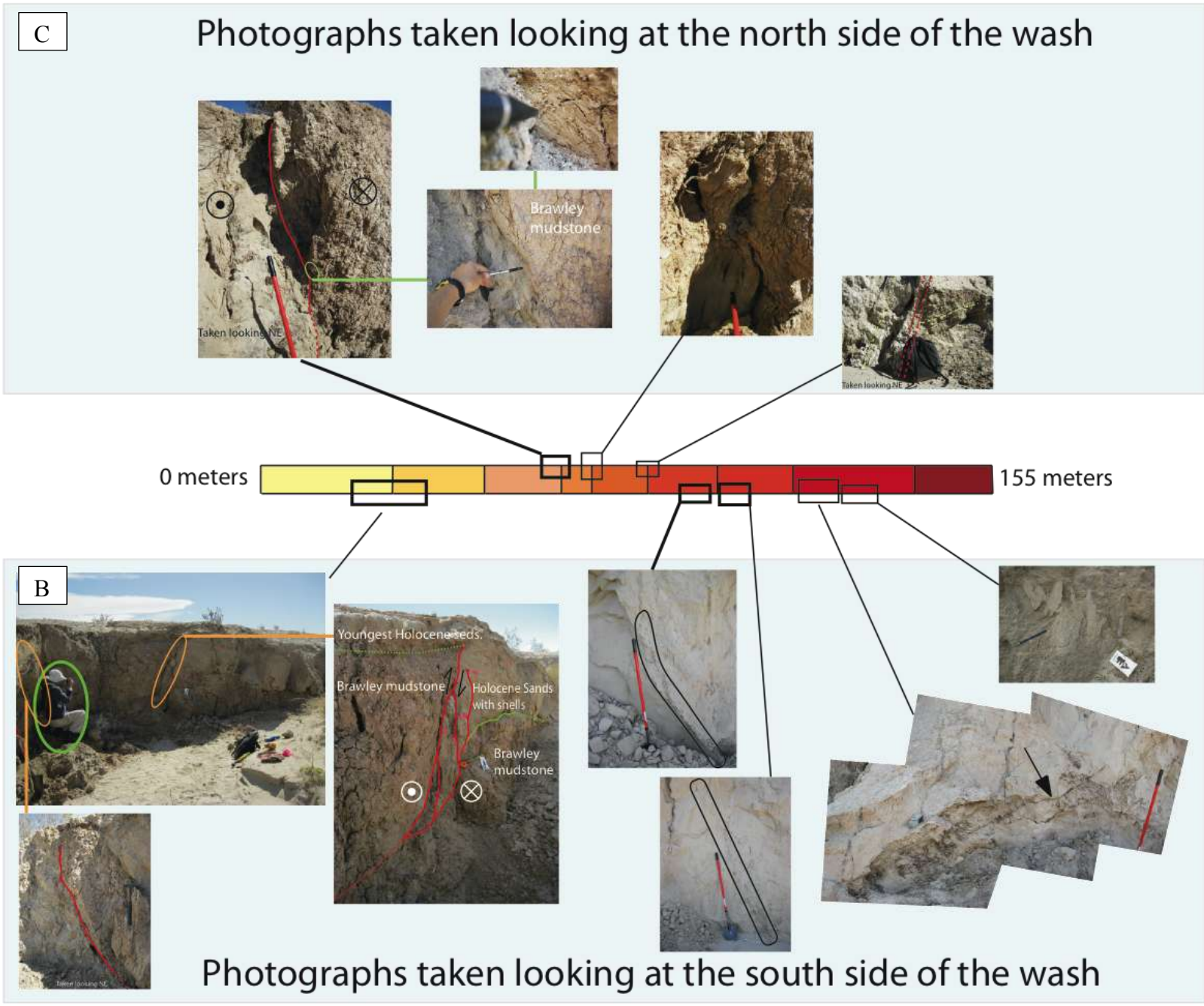
C
Photographs taken looking at the north side of the wash
Brawley mudstone
Taken looking NE
0 meters
155 meters
B
Youngest Holocene seds.
Brawley mudstone
Holocene Sands with shells
Brawley mudstone
Photographs taken looking at the south side of the wash

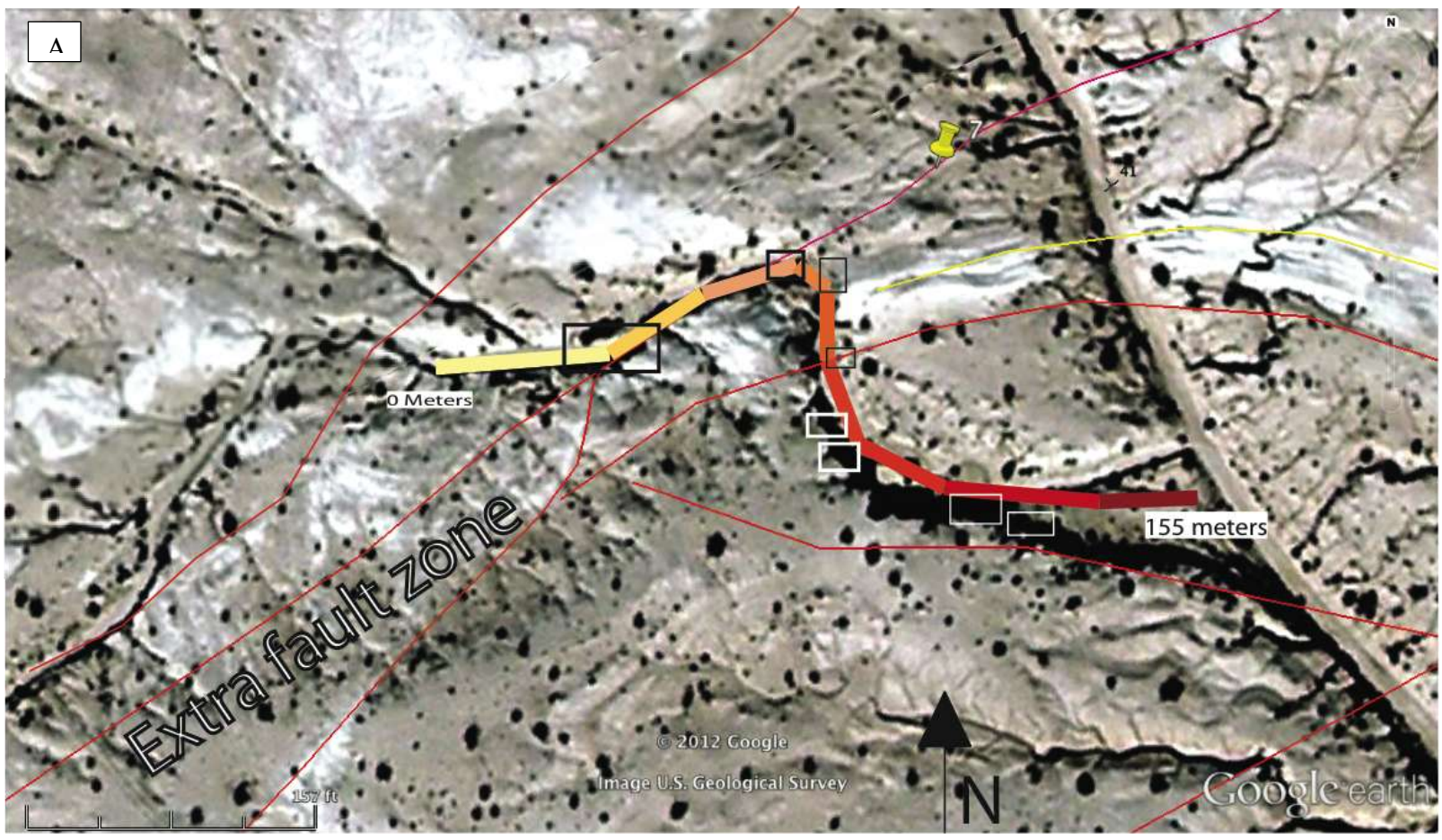
A
0 Meters
155 meters
Extra fault zone
© 2012 Google
Image U.S. Geological Survey
157 ft
N
Google earth

this gully and in several other locations, we confirmed Holocene activity on the Extra fault zone (Fig. 10). Two locations were identified with faulted Holocene deposits with shells in them (Fig. 10A and B). Two locations with OSL or radiocarbon dating and others with offset beds from Lake Cahuilla (Figs. 10 and 11). One OSL date provides a minimum of 0.7 +/- 0.29 ka since last slip on one strand of the Extra fault zone. Another OSL date provides a maximum of 10.64 +/- 1.98 ka since last slip on another strand of the Extra fault zone (Table 2; Fig. 11).

In the center of the field area, southwest of Highway 78, the Extra fault zone narrows slightly to ~0.6 km and is typified by three mostly parallel continuous faults (Plate 1). The only prominent dome along this part of the fault zone is cut in half and most faults are located northwest of the dome (Plate 1). Other small folds form between strands of the Extra fault south of Highway 78 and their fold axes tend to parallel the adjacent faults. The Extra fault zone is clear and obvious for about 5 km southwest of highway 78 (Fig. 7). Thin Holocene sediment gradually increases in thickness southwest until the Extra fault zone is mostly covered by Holocene sediment southwest of Tarantula Wash (Fig. 2). The InSAR data show the fault continuing southwestward at a N30°E strike as far southwest as Rockwell's fault (Mellors and Boisvert, 2003; Mellors et al., 2005).

Although the fault is difficult to verify farther southwest, we tentatively project it 3.5 km around a small fault block of uplifted basin fill centered at 33.063707°N and 115.989102° and then to the Coyote Creek fault (Fig. 2). This fault block of uplifted basin fill is about the characteristic size of the mini-domes that formed elsewhere along

the Extra fault zone (Fig. 2) and it may have strands of the Extra fault zone on both the southeast and northwest side.

East Extra fault zone

The east Extra fault is an incompletely mapped structure 1-2.5 km southeast of the Extra fault zone. It is related to a minidome in the center of a citrus farm that is 3.1 km north-northeast of the intersection of highway 78 and highway 86 (Fig. 2). In the southwest the fault steps into the Holocene sediment along San Felipe Wash and becomes difficult to trace. This area is structurally low between the Extra and Sebastian fault zones that accumulated more sediment during episodes of Lake Cahuilla. Displacement is probably small across this ~ 15 km long left-lateral fault.

Sebastian fault zone

The Sebastian fault zone parallels San Sebastian Marsh and merges with the more northerly striking Border Patrol fault near Highway 86 to bound an elongate lozenge-shaped block of rocks (Fig. 23). This fault is localized in flat-lying Holocene sediment in terrace deposits on the south bank of San Felipe Wash. No exposures are known from this fault but it is inferred on the basis of very linear, prominent, and numerous vegetation lineaments.

Border Patrol fault zone

The Border Patrol fault splays off the Sebastian fault and retains the original strike of about 25° north-northeast through most of the field area toward the southwest

Figure 23: Generalized Extra fault array and the Kane Spring faults of the Elmore fault array. The annotations are overlain on figure 5. Black lines are representative of primary fault zones. Dashed lines indicate sections of the faults that are covered by Holocene sediment. The various colored solid lines indicate where distances were measured between each fault zone. Distances remain fairly similar between fault zones except in locations of splaying and form overall lozenge shapes as they splay.

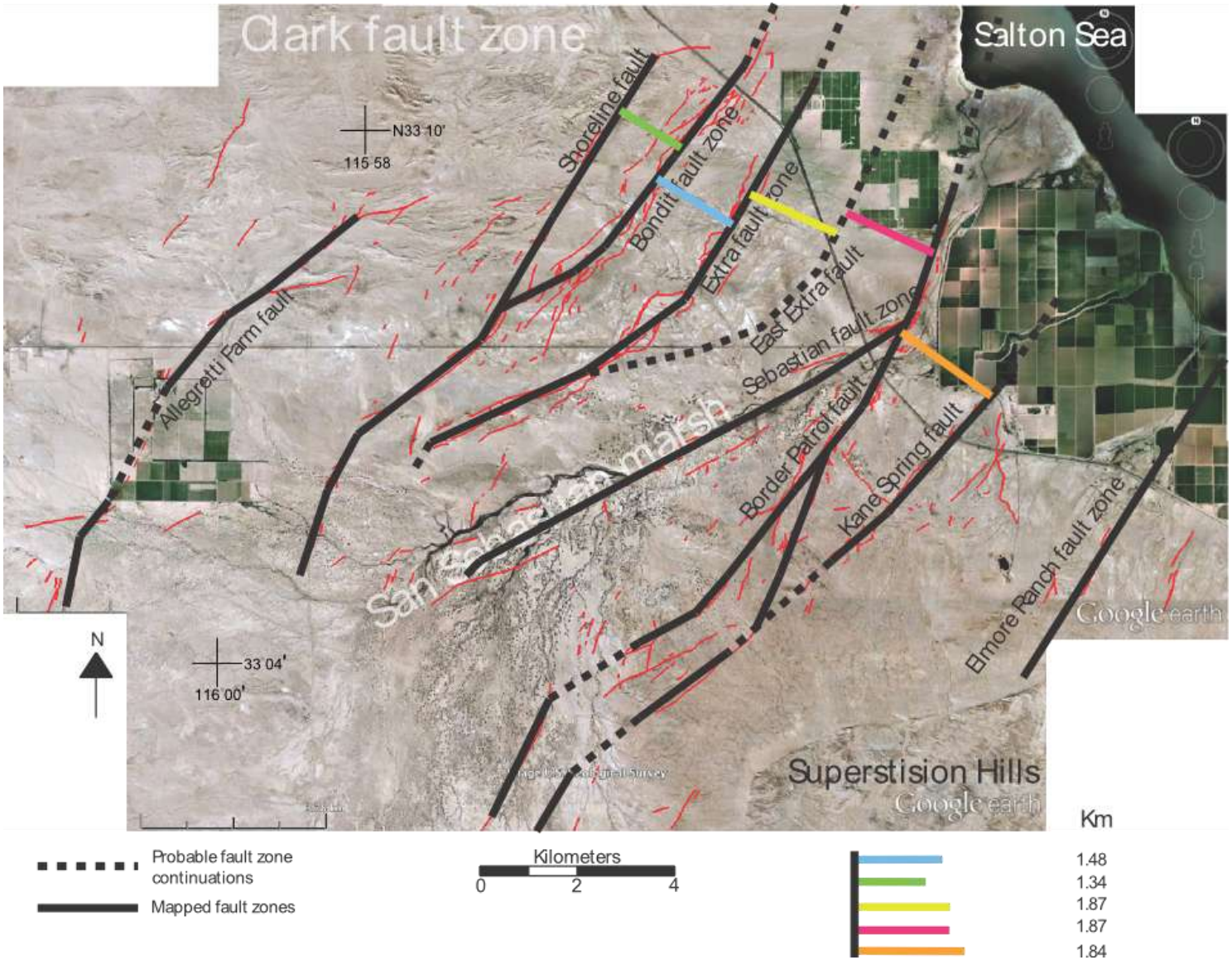
Clark fault zone
Salton Sea
N33 10'
115 58
Shoreline fault
Bondit fault zone
Extra fault zone
East Extra fault
Sebastian fault zone
Allegretti Farm fault
Border Patrol fault
Kane Spring fault
Elmore Ranch fault zone
N
33 04'
116 00'
Superstision Hills
Google earth
Probable fault zone continuations
Mapped fault zones
Kilometers
0
2
4
Km
1.48
1.34
1.87
1.87
1.84

until its intersection with the Kane Spring fault and then the Border Patrol fault zone changes strike to match that of the Kane Spring fault (Figs. 7 and 23).

The faults are mostly obscured by Holocene sediment that covers the fault for about 150 meters southwest of Highway 86 (Plate 1). Evidence for faults within the short 150-meter stretch is primarily geomorphic and very few exposures of the fault itself were observed. Southwest of this stretch is an area of good exposure and deeper incision than other areas along the fault zone (Plate 1). Folds in this section are small and cut by faults, similar to other fault zones in the Extra fault array. The Border Patrol fault then intersects the northwest-striking dextral Powerline fault zone that causes mutual interference and complex folding discussed later on. Neither fault zone is perfectly continuous through the intersection but the left-lateral Sebastian fault does appear more continuous (Plate 1). The fault dips to the southeast and has a normal-oblique component (Fig. 24).

The Elmore Ranch fault array

The faults of the Elmore Ranch fault array ruptured in 1987 as a result of the M 6.2 and M 6.6 Elmore Ranch earthquakes (Hudnut et al., 1989a; Sharp et al., 1989). Surface slip extended 9 kilometers northeast from the Superstition Hills fault on 6 parallel strands spanning about 7 kilometers from northwest to southeast (Fig. 5; Hudnut et al., 1989a; Sharp et al., 1989). Surface ruptures from the event were not mapped northeast of highway 86 because of the presence of active farm fields and the Salton Sea (Fig. 5), but the continuation of the Elmore Ranch fault array as one deep vertical strand

Figure 24: A cross section along the Border Patrol fault. A) A reference map showing the location of the cross section. B) Annotated aerial image of the cross section location. C) The cross section of the Border Patrol fault. Notice the significant amount of normal displacement to the SE on this fault. This strand is only one of many diffuse strands of the Sebastian and Border Patrol fault zones in this area that intersects a NW-striking fault zone. Colors correlate to this cross-section only. Pink is used for undifferentiated Brawley Formation. There is no vertical exaggeration on the cross section.

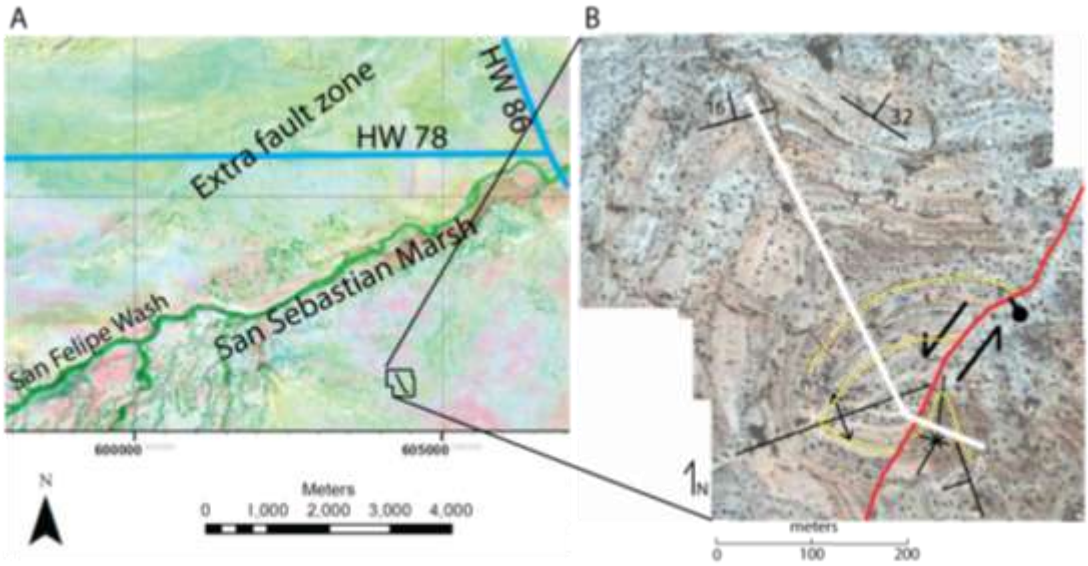
A
B
Extra fault zone
HW 78
HW 86
San Felipe Wash
San Sebastian Marsh
600000
605000
N
Meters
0 1,000 2,000 3,000 4,000
16
32
N
meters
0 100 200

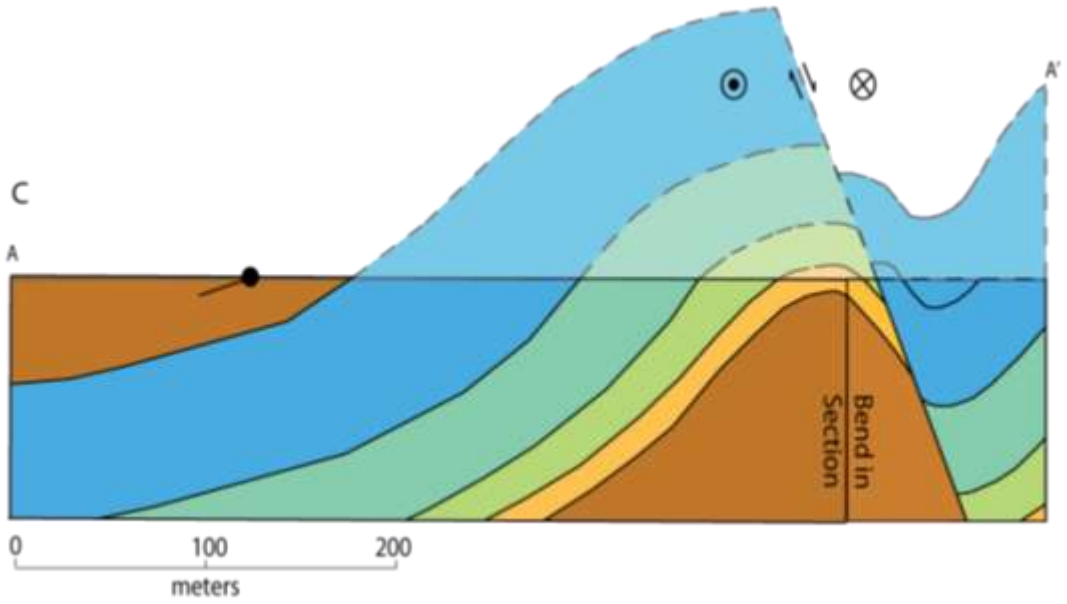
C
A
A'
Bend in Section
0 100 200
meters

is confirmed by microseismicity that persisted 15 km northeast of highway 86 (Magistrale et al., 1989; Hauksson et al., 2012; Yang et al., 2012).

The faults that comprise the Elmore Ranch fault array are the previously named and mapped Kane Spring, East Kane Spring, West Elmore Ranch fault, Elmore Ranch fault, East Elmore Ranch fault and Lone Tree fault, from the northwest to southeast (Fig. 5; Hudnut et al., 1989a). The 1987 ruptures were mapped on each fault zone in the array in moderate to good detail (Sharp et al., 1989; Hudnut et al., 1989a). The faults in the Elmore Ranch fault array are curved, bound lozenges of rocks, and contain bends and steps, particularly in the southwest where the fault zone interacts with the Superstition Hills fault (Fig. 5; Hudnut et al., 1989a and b; Sharp et al., 1989). Although the surface exposure of the Elmore Ranch fault array is complex with multiple sub-parallel strands, at depth beneath the Elmore Ranch fault array a single fault slipped and one subvertical zone of aftershocks developed (Yang et al., 2012).

Cross-sectional geometry of some strike-slip fault zones

The different structure of the Elmore Ranch fault array at the depth of the aftershocks and at the surface must reflect some kind of upward widening fault zone. We propose that the abundant mudstone in the Superstition Hills area makes a pitch-fork-type geometry the most likely explanation for the relationships along the Elmore Ranch fault array. Detailed analysis in the San Felipe Hills showed that pitchforks develop where decollements can localize along a weak layer, like a mudstone (Belgarde, 2007; Janecke and Belgarde, 2008).

Decollements in strike-slip fault zones may be arranged in a fault network that resembles the tines and handle of a pitchfork in cross-section (Fig. 8 B; Belgarde, 2007; Janecke and Belgarde, 2008). A pitchfork model is like a flower or tulip structure in that it disperses fairly localized strain at depth across a broader zone at shallower depths. The geometry of a pitchfork type strike-slip fault zone differs significantly from a tulip or flower structure in cross section, however, because strike-slip faults retain their near-vertical dip and link to coordinated decollement zones along weak bedding planes. In a pitchfork system strike-slip faults below the main decollement levels are singular sub-vertical structures. These master faults give way at shallower depths to multiple smaller-displacement strike-slip faults. Thus strain is more dispersed by activating numerous sub-vertical and sub parallel or anastomosing strike-slip faults above the main decollement levels (Janecke, unpublished model; Kirby, 2005; Belgarde, 2007). Strike-slip faults above and below the main decollement levels would be coordinated and have roughly the same orientation. Strike-slip faults can be even more complex where ramps and flats form in weak rheologies (Belgarde, 2007; Janecke and Belgarde, 2008).

The pitchfork model probably explains the subsurface relationships of the Extra fault array and might also explain some of the Clark fault zone in the San Felipe Hills. The Extra fault zone is the best developed and most active part of the Extra fault array and therefore seems to be analogous to the Elmore Ranch fault within the Elmore Ranch fault array.

Decollements also allow conjugate strike-slip faults to cross through one another or for individual dextral (or sinistral) faults at depth to be expressed by sets of sinistral (or

dextral) faults in the shallow crust instead of by more dextral (or sinistral) faults. These complexities are explored below.

Lateral strike change of the northeast-striking left-lateral faults

Although the 6 fault zones of the Extra fault array dominate the surface fault traces, there may be evidence for clockwise block rotations in the field area. Each of the cross faults of the Extra fault array exhibit a change in their strike along strike of the Clark fault, with more northerly strikes on either side of the projected fault (Fig. 25). The Extra fault array was identified to the northeast of the field area under the Salton Sea using seismic reflection (Brothers et al., 2009). The Extra fault array under the sea is split into two domains referred to as the north-northeast domain with faults that strike more north-south and the northeast

domain with faults that strike between 10-30° northeast (Fig. 25; Brothers et al., 2009). Between the southwest shore of the Salton Sea and highway 86, the Extra fault zone strikes about 30° in a "transitional" domain (Fig. 25). The exposures of the Extra fault array fault zones in the central domain in the field area exhibit a strike between 50 and 70° northeast (Fig. 25). The change to 50-70° strike is consistent with the direction expected for dextral driven rotation. Dextral shearing concentrated in the field area might cause the change in strike observed in the central domain of the Extra fault array (Fig. 25). Some of the faults abruptly change strike with linear fault strands that meet at a definite angle while other faults exhibit a curved fault trace at the boundary. Others appear to bend at more than one location (Fig. 25). With few exceptions, all the locations of strike change occur within the transitional region (Fig. 25).

Figure 25: Structural domains showing possible dextral rotation. Five colored domains are labeled with orange for the "NNE" domain, blue for the "NE domain", yellow for "Transitional", red for the "Central" and green for the "SW domain". Each colored domain corresponds with a matching rose diagram below. The rose diagrams show the orientation of fault strikes for each region. Notice the central domain with two strong orientations, one that matches the NE-domain. Lines through largest pedals are colored to match respective domains. Bold lines highlight the Extra fault zone strike change. The dashed line roughly outlines the Sebastian uplift surrounding the Clark fault and Superstition Hills fault (this study). Dextral NW-striking faults are black and NE-striking faults are orange from Janecke and Thornock (unpublished mapping). Colored dots are of earthquake hypocenters since 1981 (Hauksson et al, 2012). The topographic map was created using GeoMappApp.

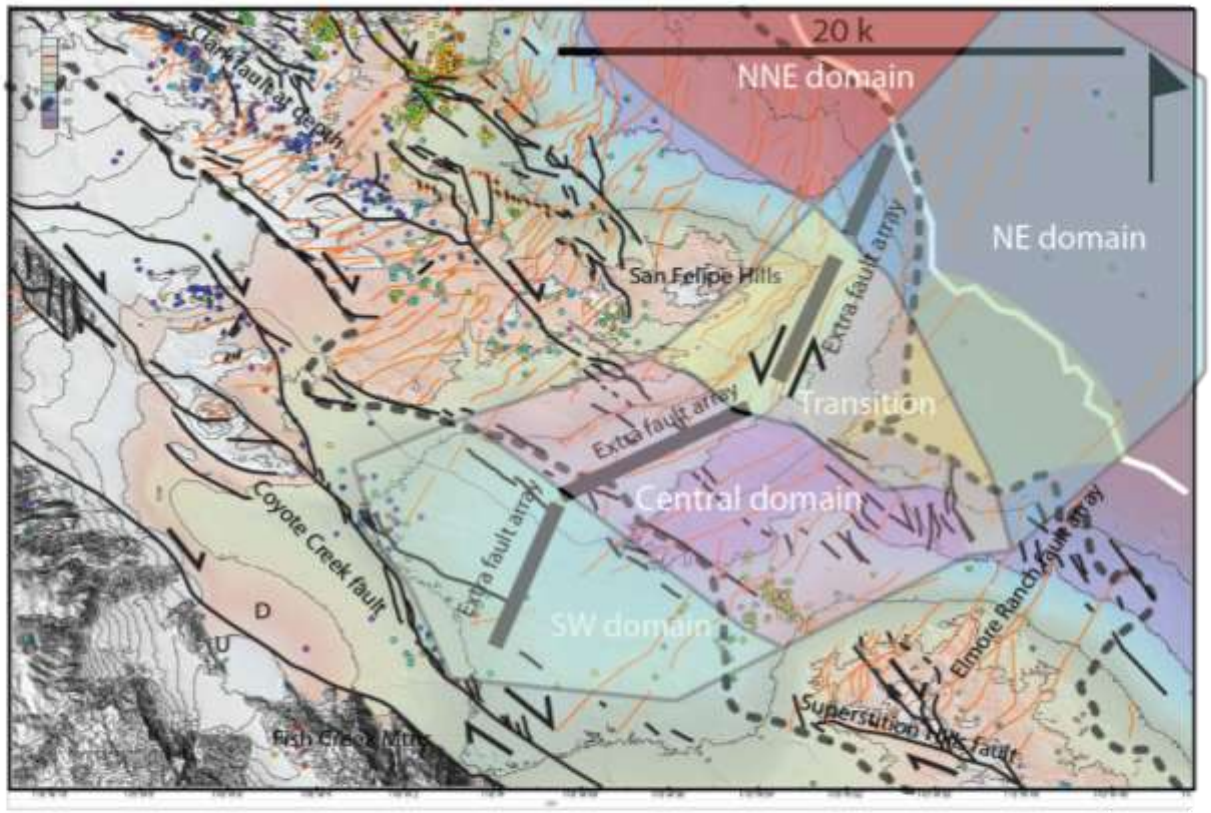
20 k
NNE domain
NE domain
Clark fault at depth
San Felipe Hills
Extra fault array
Transition
Extra fault array
Central domain
Extra fault array
Coyote Creek fault
SW domain
Elmore Ranch fault array
Superstition Hills fault
Fish Creek Mtns
D
U

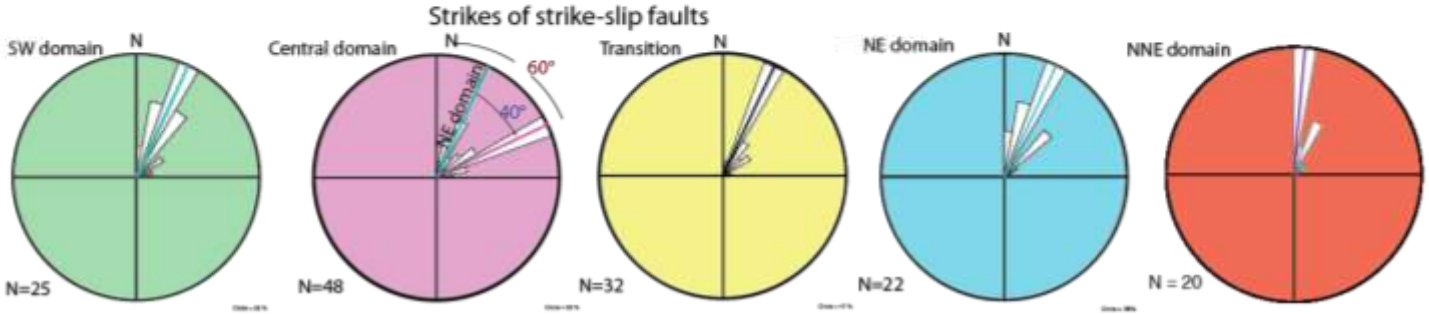
Strikes of strike-slip faults
SW domain
N
N=25
Central domain
N
60°
NE domain
40°
N=48
Transition
N
N=32
NE domain
N
N=22
NNE domain
N = 20

The left-lateral faults retain their strike of about 60° throughout the central domain in straight, relatively well-developed fault zones (Fig. 25). Near the western edge of the central region the faults of the Extra fault array seem to abruptly change their strike again, reverting back to their original strike between 0 and 30° northeast at an angle that would intersect the Coyote Creek fault orthogonally. The western strike change appears to occur abruptly, with the bend in each fault roughly forming a line that trends northwest (Fig. 25).

Faults southwest of the field area in Lower Borrego Valley were mapped in reconnaissance on imagery and InSAR data sets. No direct measurements were recorded from faults in the field. Evidence for the fault continuation toward the southeast into the thick Holocene sedimentary sequence is the unusually linear trend of some drainages, vegetation lineaments, strong to subtle anomalies on InSAR datasets, and small fault-bounded ridges mapped on Google Earth imagery and digital elevation models (Fig. 25). The most compelling evidence for the north-northeast strike of the left-lateral faults in the southwest domain is in an elongate low ridge through 33.037404°N and -115.897548°E and the southeast edge of the subsidence centered on Allegretti Farm that is imaged by InSAR (Lyons and Sandwell, 2003; Mellors and Boisvert, 2003; Mellors et al., 2005;Wei et al., 2009).

Structural expression of the left-lateral fault zones of the Extra fault array in each structural domain

The fault zones of the Extra fault array exhibit slightly different structural expressions from northeast to southwest in 4 distinct structural domains (Fig. 25). Brothers et al. (2009) describe the Extra fault zone as a series of normal faults within the

northeast domain, under the Salton Sea. Normal motion is expected in the stress field on faults that strike north-south so the 0-30° strike of the Extra fault array under the Salton Sea is expected to have normal displacement (Townend and Zoback, 2004). The reflectors appear to be subhorizontal so any apparent dip-direction offset probably represents actual dip-slip. If the strata were tilted, strike-slip motion could appear to be dip-direction instead. Normal fault throws of 1.7 to 2.7 m are measurable in the youngest sediments of the sea (Brothers et al., 2009, 2011). This two-dimensional seismic reflection data set cannot be used to measure strike-slip components that could be a significant component of the strain.

The transitional domain is slightly uplifted and has well developed complex folds along most fault zones of the Extra fault array. The Extra fault zone and Kane Springs fault zones in particular are characterized by several faulted anticlines along their traces. These structural highs typically coincide with topographic highs in the landscape. Dunes nucleate preferentially along fault zones and therefore augment the subtle rises of these positive structures. Mesquite bushes tend to colonize on higher areas, as well as along water-rich fault zones. In turn, the vegetation nucleates coppice dunes and dune fields that are common in the transitional domain. The transitional domain is also typified by multi-strand faults with complex relationships including en echelon right-step over (Fig. 25; Plate 1). Most of the faults exhibit a small strike change within the transitional domain (Fig. 25).

The central domain also contains some folds but the folds are often cut by faults or concentrated on one side of the fault zone. Fully formed domes are much smaller than

the folds that are cut by faults and they typically lie between parallel strands of the fault zone (Plate 1). Fault strands in the central domain are not en echelon but form more continuous, parallel strands (Plate 1). The fault zones in the central domain are narrower and they splay less than in the transitional domain. Coppice dunes and dune fields are as common in the central region as the transitional region (Plate 1).

The southwest structural domain primarily exhibits geomorphologic evidence for faults (Fig. 25). Multiple straight sections of drainages and aligned vegetation are parallel with the limited number of fault scarps (Plate 1). Fewer northwest trending lineaments in this domain agrees with observations elsewhere in the field area that northeast-striking faults outnumber northwest-striking faults at the surface (Plate 1).

Lozenges bounded by northeast-striking left-lateral faults with regular spacing

Structural mapping shows that some the left-lateral faults are roughly parallel to one another but there is also a tendency for the faults to branch and merge around elongate lozenge-shaped fault blocks in map view (Fig. 23). The ruptured fault traces of the Elmore Ranch fault array show this pattern particularly well because the full extent of that fault array was revealed by the earthquake. The Extra fault array also has this geometry but linkages between faults are less clear because of Holocene sedimentation that partly obscures the geometry of the faults in map view.

There is a systematic and fairly regular spacing in map view between the left lateral faults at the widest part of each lozenge-shaped fault-block (Fig. 23). Starting at the northwest-most Shoreline fault of the Extra fault array, the northeast-striking left-lateral fault zones recur toward the southeast for at least 25 km (Fig. 23). The northeast-

striking left-lateral fault zones are spaced at nearly regular intervals of ~1.5-2 km. (Fig. 23). The distance between fault zones is variable due to strike-changes and the overall lozenge shape of the fault network in map view (Fig. 23). We attempted to measure distances between the fault zones northeast of the strike change for each fault zone to remain objective, but difficulty in identifying a specific location for a strike change in some fault zones and some bias may have introduced error. The regular interval of the faults might define rigid-block boundaries that accommodate dextral rotation in the area.

Faults of the Extra fault array exhibit sinistral slip

Slickenlines in the left-lateral fault zones

We looked for slickenlines on every large strand of each fault zone in the Extra fault array to help determine overall sense of slip in the fault array and to resolve the dispute between prior studies along the Extra fault about the kinematics of the fault (Hudnut et al., 1989a; Brothers et al., 2009, 2011). Slickenlines are not abundant (Fig. 26) because the majority of faults are expressed within poorly or unconsolidated sediments that do not record toolmarks or slickenlines on the fault surface. Another issue that limited the collection of slickenline data was a small number of exposures of fault surfaces.

Slickenlines are typically preserved in faulted lithified mudstone. Often the faulted mudstones record slickenlines so well that multiple surfaces exhibit slickenlines on minor fault planes a wide range of orientations, including many that appeared to be at high angles to the dominant slip sense across the primary slip surface (Fig. 26).

Figure 26: Slickenline locations and measurements used to determine slip direction of faults in the Extra fault array. Locations of slickenline measurements are marked with letters on the location map and colored with matching letters and background colors in each photoset around its perimeter. The scaled items are circled and the unclear item in figure B2 is a ballpoint pen-tip and C2 is the tip of a mechanical pencil. The stereonet is equal area that shows all line measurements from the six locations. The one NE-trending lineament was taken from the Elmore Ranch exposure that had variable orientations. The basemap is part of fig. 2.

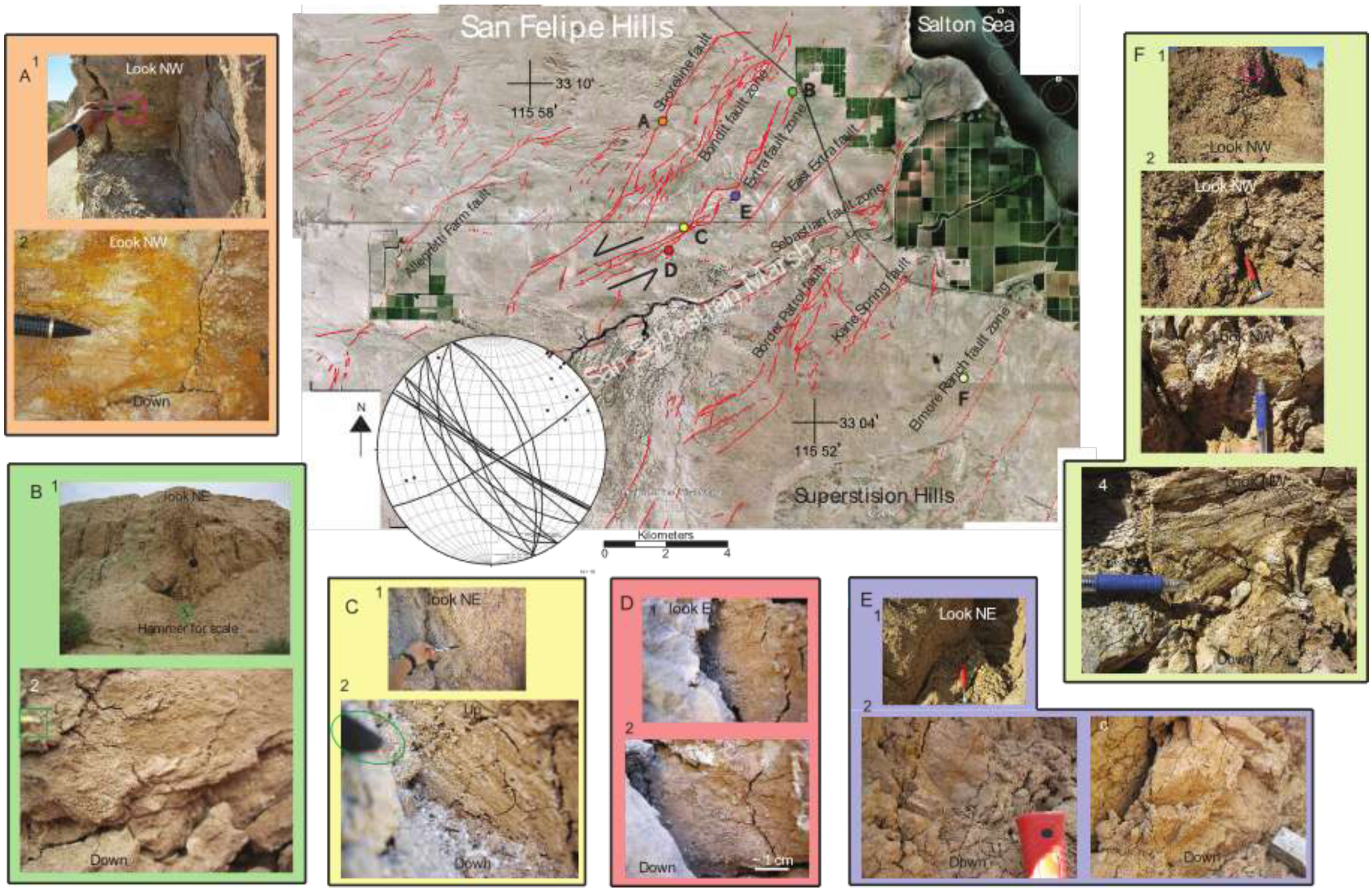
A
1
Look NW
2
Look NW
Down
San Felipe Hills
Salton Sea
33 10'
115 58'
Shoreline fault
Bandit fault zone
Extra fault zone
East Extra fault
Allegretti Farm fault
Sebastian fault zone
Border Patrol fault
Kane Spring fault
Elmore Ranch fault zone
Obsidian Butte
Salton Sea
Marsh
33 04'
115 52'
Superstition Hills
Kilometers
0 2 4
N
A
B
C
D
E
F
B
1
look NE
Hammer for scale
2
Down
C
1
look NE
2
Up
Down
D
1
look E
2
Down
~ 1 cm
E
1
Look NE
2
Down
c
Down
F
1
Look NW
2
Look NW
Look NW
4
Down

It was common for large faults to form complex damage zones, particularly when they were localized in indurated mudstone. These faults sometimes produce identifiable slickenlines on small pieces of broken-up mudstone that appear to have been re-oriented in the fault's damage zone and have lost their original orientation. All reported data measurements are from primary slip surfaces of prominent faults within a fault zone or on subsidiary faults that parallel the primary fault in the fault zone (Fig. 26).

Four locations on the Extra fault, two on the Shoreline fault and one on the West Elmore Ranch fault (Fig. 26) produced reliable slickenline populations (Fig. 26). Others were found on small subsidiary faults with variable slip directions. All six localities in the Extra and Elmore Ranch fault arrays reveal primary strike-slip motion with smaller oblique components of slip (Fig. 26). The northern-most measurement on the Extra fault shows the least amount of dip-slip with only 1-2° of plunge on most lineaments (Fig. 26 B). This same location has tool marks that indicate left-slip (Fig. 26 B). Other slickenlines in the Extra fault zone plunge as much as 25° (Fig. 26 C).

One well-exposed strand in the Extra fault ~100 meters south of highway 78 displaces Brawley mudstone in reverse sense on Holocene sand across a steep fault surface (Fig. 26 C). Slickenlines preserved in mudstone in the hanging wall plunge to the southwest. Since the fault motion is oblique-reverse, the primary slip direction must be sinistral. If the motion were right lateral it would produce normal motion instead of the observed reverse. At least one other location on the Extra fault exhibits a reverse component of slip.

The exposure of the Elmore Ranch fault (at 610608 E and 3660922 N UTM zone 11N) (Fig. 18 F) is the most complex exposure of any fault in the study area and contains many significant and closely spaced subsidiary faults in a narrow damage zone. It has slickenlines in various orientations in a highly deformed damage zone (Fig. 26 F). The dominant orientation of slickenlines is strike-slip with a small oblique component. This is true regardless of the strike of the slip surface (Fig. 26 F).

Exposures of slickenlines from the Shoreline fault were from Oil Well Wash (Fig. 26 A). The only data point used from the fault zone was from a subsidiary fault that dips more steeply than the main fault core but because it has the same strike is thought to accurately record the sense of slip across the fault (Fig. 26 A). The trend of the slickenlines matched the strike of the fault and they had ~2° plunge.

Measurements from all the fault zones were compiled from six locations with measurable slickenlines on primary slip surfaces. The mean rake of these 16 measurements is -12.7° with a minimum of 0 and maximum of -40° (Fig. 26).

Most northeast-striking left-lateral faults in the Extra fault array dip 60-90° southeast or northwest but there is a slightly larger population of faults that dip southeast (Fig. 12 C). Most exposures of larger faults within incised drainages are vertical to steeply dipping. Shallower dips also occur but are rare and typically came from small subsidiary structures within the fault zones with some notable exceptions. These faults often required digging a mini-trench across the strike of the fault into order to determine the dip direction and dip amount. The attitude of faults measured in such mini-trenches is less precise than those measured from natural outcrops.

Doubly-plunging anticlines at right steps in left-lateral fault zones

Some of the fault zones in the Extra fault array are structural highs with structural lows adjacent to them (Plate 1; Fig. 7). The Extra fault zone and the Kane Spring fault zone are particularly notable for the many structural domes and anticlines along them (Fig. 7). The highs are so important that the Elmore Ranch and Elmore Ranch East faults, in the Superstition Hills, together produce the northeast trending higher terrain in the northern Superstition Hills (Sharp et al., 1989). The Sebastian fault zone along the San Sebastian Marsh area is somewhat unusual because it is located within the lowest topography of the area and lacks identifiable doubly-plunging anticlines and domes.

Anticlines are the most pronounced and obvious folds in the field area (Plate 1). Their topographic relief is subtle but sufficient to localize sand dunes on their crests and downwind side (Plate 1; Fig. 7). The average dip measurement at the steepest part of most anticline limbs is about 45° (Plate 1). Unless complicated by northwest-striking dextral faults, fold axes within left-lateral fault zones are oriented roughly E-W between 69 and 126° azimuth (Plate 1). Dome widths vary from <0.1 km to about 1 km along trend of the axes (Plate 1). Most anticlines form symmetric limbs and are not significantly cut by younger faults. Folds in the central domain are typically more variable in the orientation of their axes and have been apparently re-folded and cut by younger faults. When northeast-striking left-lateral fault zones cross with prominent dextral faults or fault zones, fold axis azimuth orientations are much more variable and intersections with other folds and faults complicate fold relationships including elongating some folds in multiple directions (Plate 1). Box folds and crossing axes are common in these locations and axes form in any azimuth direction.

Doubly-plunging anticlines within the Extra fault array typically lie between right-stepping fault strands (Plate 1; Fig. 7). Sharp (1967) explains how en echelon fault steps produce contraction or extensional features depending on the sense of slip and geometry (Fig. 8). Namely, in right-lateral systems left steps produce contraction whereas in left-lateral systems right steps produce contraction. Because right-steps within the Extra fault zone produce contraction between the strands, we interpret the slip across the faults to have a major left-lateral component (Fig. 8).

The geometric result of the right-stepping strands of the Extra fault zone is to produce a fault zone with a trend that is about 16° clockwise of the dominant strike of individual faults in the zone. Faults within the Elmore Ranch fault array have similar complex steps and bend (Sharp et al., 1989; Fig. 5). This geometry may also explain the fact that the focal mechanism of the main shock of the Elmore Ranch earthquake was 24° more northerly than the dominant strike of the fault that is clearly defined by its aftershock sequence (Yang et al., 2012).

Northwest-striking dextral faults

Northwest striking dextral faults are much less numerous in the field area than sinistral faults. The shallow dextral faults in the field area are organized into common geometric map patterns (Figs. 13 and 27). Many dextral faults appear to be connector faults between the more laterally continuous sinistral faults, and these are present across much of the area. These dispersed dextral faults are short and have small displacements. Some slightly longer and larger dextral faults may form a rough left-stepping dextral array that project toward the northern tip of the Imperial fault zone (Fig. 27). The pattern

Figure 27: Areas of concentrated NW-striking faults that step progressively to the SE. Each fault zone is highlighted in blue and one in green. Only NW-striking faults are shown to reduce complication. Other locations have some NW-striking faults but faults in these zones are generally larger and more continuous with closer spacing. Several fault zones are outside of the main field area but most were field checked. The basemap image is from Google Earth 2012 Digital Globe.

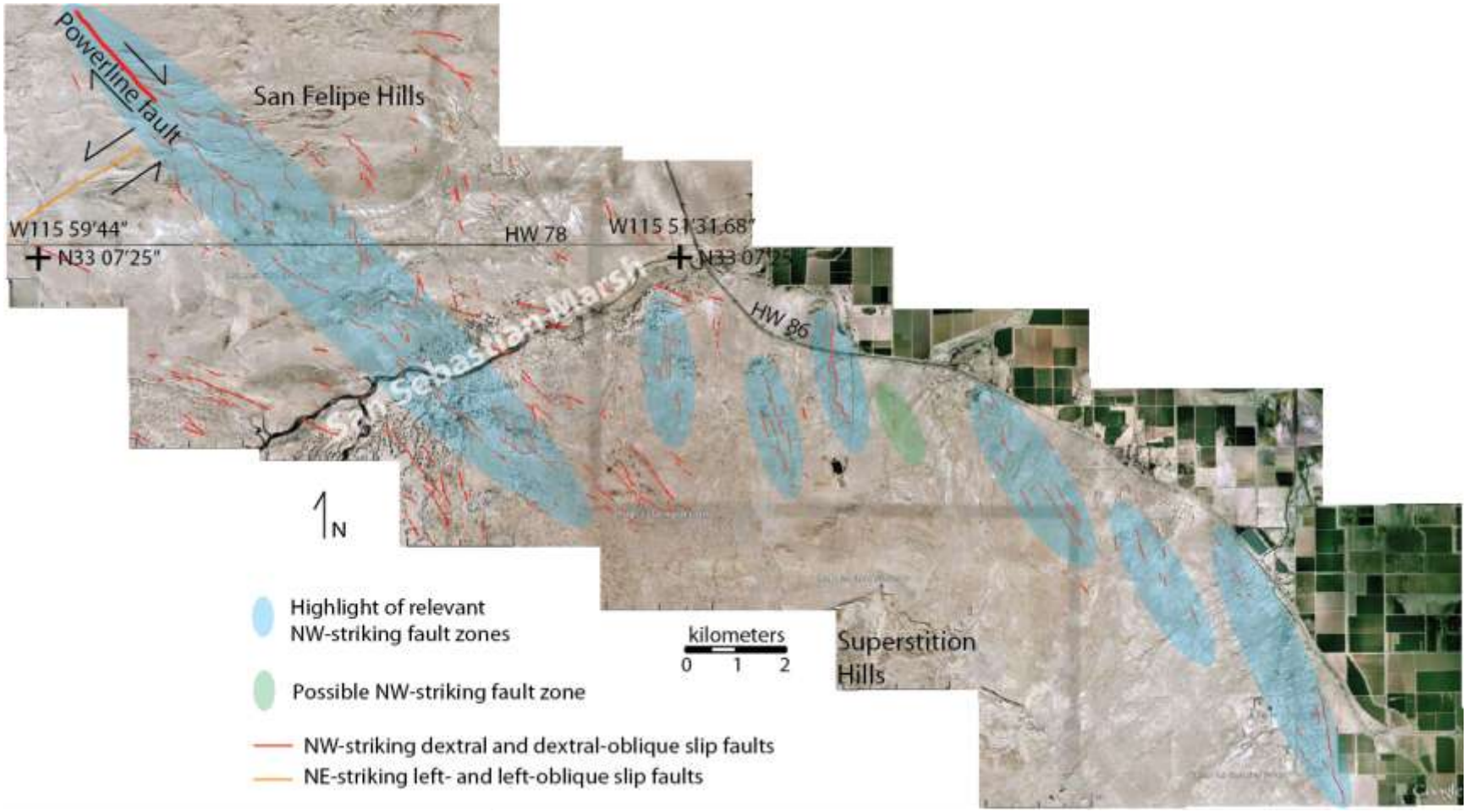
Powerline fault
San Felipe Hills
W115 59'44"
N33 07'25"
HW 78
W115 51'31.68"
N33 07'25"
San Sebastian Marsh
HW 86
N
Highlight of relevant NW-striking fault zones
Possible NW-striking fault zone
NW-striking dextral and dextral-oblique slip faults
NE-striking left- and left-oblique slip faults
kilometers
0 1 2
Superstition Hills

includes some normal dextral faults that ruptured at the earth's surface during the Elmore Ranch earthquake and a number of suspected faults based on microseismic data southeast of the field area (Hudnut et al., 1989a; Sharp et al., 1989) (Fig. 27). Another group of small-offset dextral faults connect fairly directly between the Powerline strand of the Clark fault and the Superstition Hills fault, albeit with some unfaulted areas along the way (Fig. 28). The only potentially sizable dextral faults in the field area at the surface are buried at the southwest margin of the Sebastian uplift and within Lower Borrego Valley (Fig. 2). The two potentially larger dextral faults are Rockwell's fault, which ruptured at its northwest end in the 1968 Borrego Mountain earthquake (Sharp and Clark, 1972) and the hypothesized fault zone along the southwest margin of the Sebastian uplift in the field area. Rockwell's fault is clearly a barrier to the flow of groundwater and bounds a subsiding area around Allegretti Farm (Mellors and Boisvert, 2003)

Cross faults between dextral faults and sinistral fault arrays

Some right-lateral faults are scattered throughout the field area (Plate 1). Most appear to be secondary cross faults formed by motion along the left-lateral faults of the Extra fault array. Dextral faults northwest of the field area associated with the Clark fault become dispersed, ending or transferring strain into other structures (Fig. 13). Kim et al. (2004) reviews damage zones of strike-slip faults and describes relationships very similar to observations in the field area (Fig. 29). At the tips of strike-slip faults two common features are synthetic branch faults and antithetic faults (Figs. 13 and 29). The southern extension of the Clark fault into the San Felipe Hills widens into a zone of synthetic branches and some increase in abundance of antithetic faulting, potentially representing

Figure 28: Southeastward continuation of the Powerline fault zone. A) The black-outlined polygon highlights the Powerline fault zone along strike of the Powerline fault. Only NW-striking faults are displayed on the map. The solid green line represents average strike direction of the faults. The dashed green line is a hypothetical pre-rotation continuation of the fault zone. The dashed orange line represents the Bondit fault zone and also where the NW-striking fault zone changes strike entering the Extra fault array. B) A closer view of the intersection of the Powerline fault zone with a strand of the Sebastinan fault showing complex folding and fault orientations. Yellow and blue lines are marker units and fold axes respectively

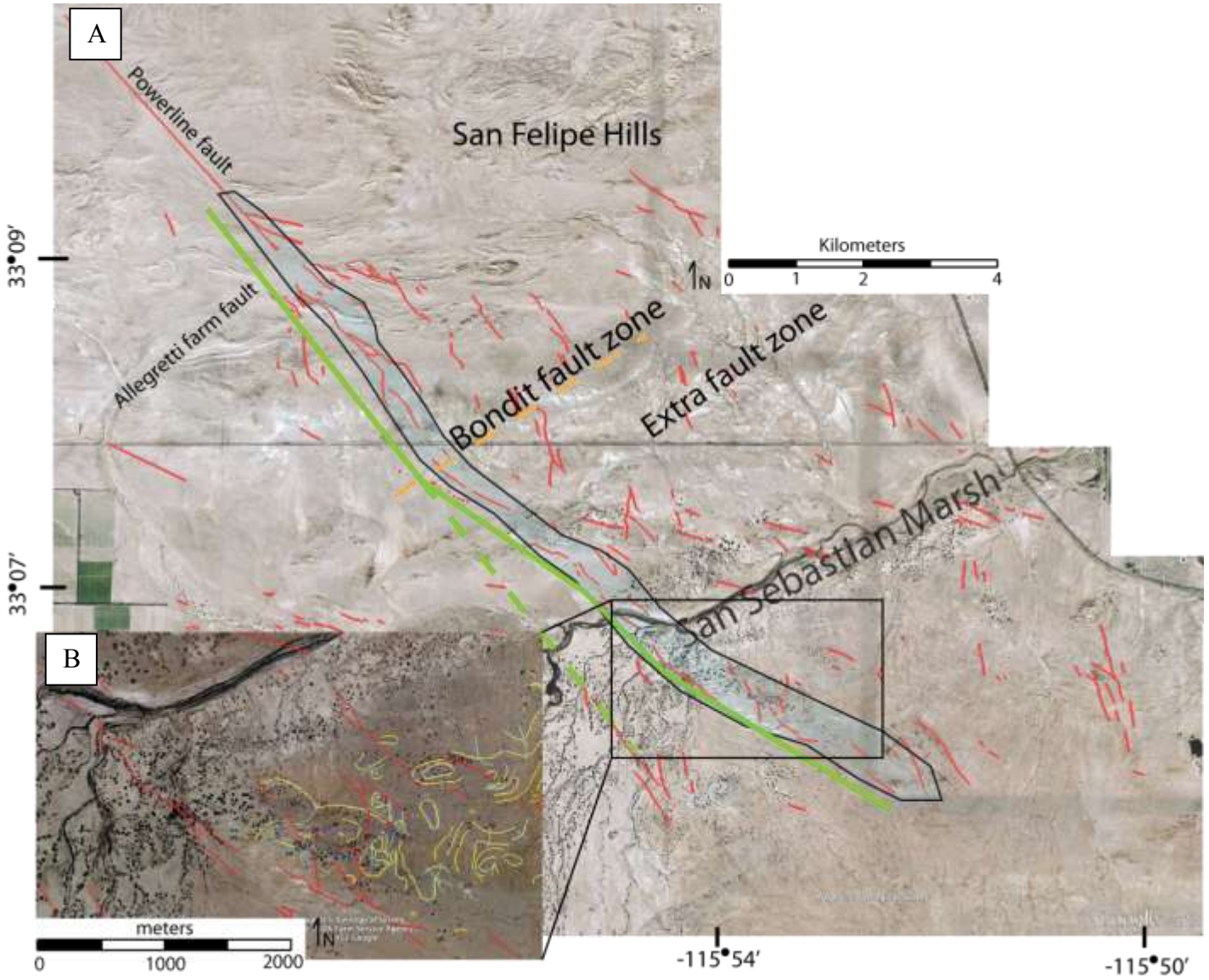
A
Powerline fault
San Felipe Hills
Kilometers
0 1 2 4
N
33°09′
Allegretti farm fault
Bondit fault zone
Extra fault zone
San Sebastian Marsh
33°07′
B
meters
0 1000 2000
N
-115°54′
-115°50′

Figure 29: Examples of strike-slip fault damage zones from Kim (2004). Only some pieces of each original figure are represented. All included figure captions are also from the original article but only contain relevant information for pieces of each figure shown.

Examples of wall damage zones around strike-slip faults. (d) Normal faults within the strike-slip Lake Basin Fault Zone, Montana, USA (Dobbin and Erdman, 1955; Wilcox et al., 1973). (f) Antithetic and synthetic faults at Dasht-e Bayaz, Iran (Tchalenko, 1970; Tchalenko and Ambraseys, 1970).

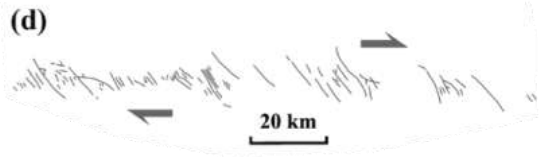

An example of linking damage zones in strike-slip fault zones. (b) Extension fractures and strike-slip duplexes at Dasht-e Bayaz, Iran (Tchalenko and Ambraseys, 1970).

Schematic illustrations of the main types of tip damage zones. The tip damage zones are divided into four major types (b–d), and some combined or mixed tip damage zones occur (e–f).

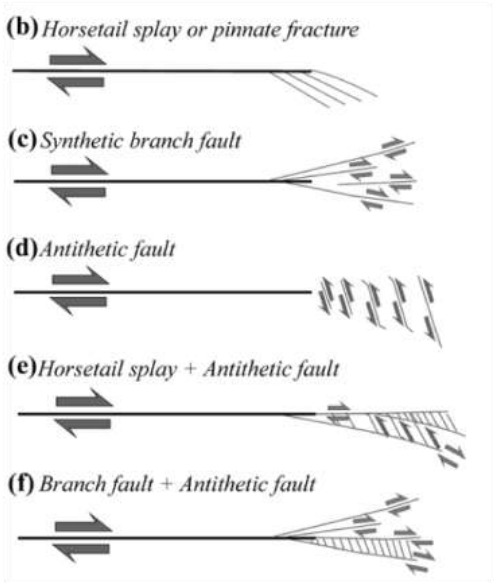

Examples of damage zones at the mode II tips of strike-slip faults. Sinistral examples are reflected into a dextral sense for ease of comparison. Thick line ¼ major fault, thin line ¼ minor fault, shading ¼ vein, which is part of the damage zone. The dotted shadings indicate tip damage zones. (c) Horsetail fractures in schists and Carboniferous sedimentary rocks at Villefort's region, France (Granier, 1985). (h) Antithetic faults at Dasht-e Bayaz, Iran (Tchalenko and Ambraseys, 1970).

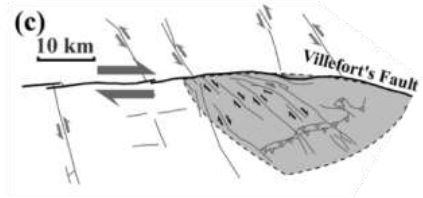

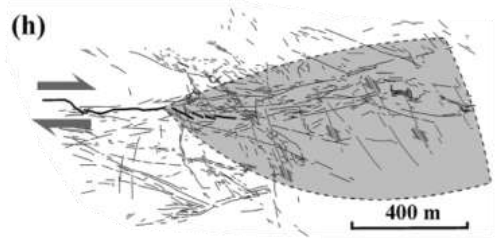

the initial southeastern damage zone of the Clark fault (Figs. 13 and 29). Southeast of the termination of the synthetic dextral faults they are replaced by the antithetic faults of the Extra fault array. The Extra fault array could be an incipient extension of the Clark faults southern-tip damage zone.

Southern Clark fault zone

The southern Clark fault damage zone consists primarily of four dextral faults with abundant intermixed folding and antithetic faulting (Kirby, 2005; Kirby et al., 2007; Belgarde, 2007). Most of the dextral faults terminate within the southern San Felipe Hills (Fig. 2). From west to east the main strands are the San Felipe Hills, Powerline, Sand Dune and Dump faults (Janecke and Belgarde, 2008). The Powerline fault is the larger of the two central strands in the southern Clark fault zone (Kirby, 2005; Kirby et al., 2007). The surface trace of the Powerline fault is straight and continuous for ~6 kilometers in the central San Felipe Hills and is probably a major structure because it separates different formations along several kilometers of its trace (Fig. 28 A)

Of the four larger strands of the Clark fault in the San Felipe Hills, the Powerline fault is the one most likely to persist to the southeast. Other strands clearly end in the San Felipe Hills or transfer their slip to adjacent structures (Kirby et al., 2007; Belgarde, 2007).

Detailed mapping at the southern tip of the Powerline fault shows that it exhibits fault splays in a small-scale synthetic branch fault zone northwest of the intersection with the sinistral Allegretti Farm fault (Fig. 15). Southeast of the intersection the Powerline

fault exhibits only minor faults on multiple dispersed strands that we refer to as the Powerline fault zone (Fig. 28).

Several hundred meters southwest and northwest of the intersection of the Allegretti Farm fault with the Powerline fault respectively, the surface traces of both faults are continuous and well developed (Fig. 15). About 1 km northwest or southeast before the intersection, the Powerline and Allegretti Farm faults respectively change from continuous strands to synthetic splays (Fig. 15). For several hundred meters near the intersection of the two faults, faults striking both northeast and northwest mutually interfere in a complicated transition zone (Fig. 15). The Allegretti Farm fault seems most continuous through the intersection but northwest-striking right-lateral faults intertwine and appear on both sides (Fig. 15). After the intersection the Powerline fault zone is longer and more easily identifiable as a fault zone than the Allegretti Farm fault, perhaps because the Allegretti Farm fault parallels stratigraphy (Fig. 15). The overall geometry thus is one of conjugate faults mutually cancelling one another where they meet. The relationship between the Powerline and Allegretti Farm fault might indicate what is happening to the Clark fault in a broader sense with the Clark fault transitioning strain into other structures.

Mapping did not reveal a robust continuation of the Powerline fault to the southeast of the intersection with the Allegretti Farm fault (Fig. 28). Instead, the Powerline fault seems to lose displacement and continue as a pair of smaller splaying faults, the East Powerline and West Powerline fault. The East and West Powerline faults

can be traced southeast with some confidence to the Bondit and Extra fault zones but beyond that there is great uncertainty about its continuation.

Part of the cryptic character of the Powerline fault southeast of its intersection with the Allegreti Farm fault may be due to thicker Holocene cover there. For example, in the San Felipe Hills where the Powerline fault zone projects, the top of the Brawley is thinly covered by evaporites and other Holocene sediment, obscuring some relationships (Plate 1). South of Highway 78 there is more Holocene sediment, providing even less evidence for small faults (Plate 1; Fig. 28). Nevertheless, larger sinistral faults in these same areas, like the Bondit, Extra and Border Patrol fault zones are more obvious and mappable, so we infer that no sizable dextral faults were overlooked in this area.

Southeast of San Sebastian Marsh there are more dextral faults that could possibly be part of the Powerline fault zone in the Brawley mudstone (Fig. 28), but it is impossible to be certain because they lack lateral continuity, they have small or unknown displacements, and resemble small dextral faults that occur all over the study area. In the Superstition Hills, Pendelton and Janecke (unpublished mapping for a Senior Thesis at USU) identified an alignment of small-offset dextral faults that project northward toward the southern tip of the Powerline fault. The fault zone persists roughly 4-5 km from a southeastern branch-point with the Superstition Hills fault is at UTM 11S 609109 m E, 3653822 m N. Some sections of this fault zone were mapped in Sharp et al. (1989).

Groups of northwest-striking right-lateral faults that may step left to the Imperial fault

Besides the Powerline fault zone, most other northwest-striking right-lateral faults are scattered fairly randomly through the area and seem to be mostly short, fairly narrow,

small offset fault zones that link like rungs on a ladder between adjacent northeast-striking left-lateral faults (Fig. 27). These cross faults are typically no longer than 3 km and 1 km wide with three discontinuous strands each (Fig. 27). Some of the dextral faults appear to be concentrated into small, short fault zones. None of the small fault zones are continuous across significant left-lateral faults although some of the fault zones are not exposed well enough to determine their relationship with the cross faults. These groups of dextral faults might account for some of the dextral strain of a through going Clark fault. Few of these dextral faults show evidence for Holocene activity.

Those dextral faults with evidence for Holocene ruptures, including a dozen short fault strands that failed in the 1987 Elmore Ranch earthquake, occur east of the Superstition Hills, near Kane Spring, and along the East Powerline and West Powerline faults. Most of these faults strike north-northwest although several strike north-northeast and have normal components of slip. Although imperfect, the dextral normal faults with Holocene activity appear to form a left-stepping en echelon array that is composed of many small fault strands and includes quite a few irregular patterns. The complexity of the en echelon faulting may be due to the interfering left-lateral faults in the area. Each fault or fault zone is typically separated by 1-2 kilometers east-west and recur to the south about the same. The pattern of left-stepping active faults may persist outside of the area examined in this study to link ultimately to the dextral-normal strand of the Imperial fault along the west edge of Mesquite Basin (Fig. 1). InSAR data sets along the eastern flank of the Superstition Hills may be useful to further refine this interpretation.

Similarity between the Clark fault zone in the San Sebastian Marsh area and the Brawley Seismic zone

The northeast-striking Extra fault array is positioned between the southern termination of the Clark fault and the northern termination of the Superstition Hills fault. The relationship is similar in that respect to the Brawley Seismic zone that is positioned between the San Andreas fault and the northern extent of the Imperial fault (Fig. 30 A). The San Andreas fault appears to terminate where the Brawley Seismic zone replaces it southward and is revealed by abundant microseismic swarm events (Fig. 30 A). Typical plate boundary dextral faulting resumes again along the Imperial fault to the south (Fig. 30; Dibblee, 1954). Seismicity within the Brawley seismic zone occurs on east-northeast-striking left-lateral faults that form aligned epicenter swarms (Fig. 30). Hypocenters associated with a swarm event on a fault occur at similar depths and within the same year, typically within a small window of time. Small north or northwest-striking faults revealed by epicenter alignments between the longer northeast-striking faults are often truncated by the northeast-striking left-lateral faults (Fig. 30) even though the zone transfers the dextral strain evident within and perhaps equivalent to strain on the San Andreas and Imperial faults (Fig. 1). The small amount of slip produced by the small seismic events on left-lateral faults is likely not enough to account for all the dextral slip.

Seismicity in the Brawley Seismic zone and surface faults in the San Sebastian Marsh area both indicate dominance of northeast-striking left-lateral faults in a stress regime that forms dominantly dextral faults (Fig. 30). One observation in the Brawley Seismic zone indicates how the Clark fault might continue in the subsurface through the Extra fault array. Evidence for crossing faults is shown at a much smaller scale within

Figure 30: Microseismicity and interpretation of the Brawley Seismic zone. A) The Brawley Seismic zone is outlined in a blue dashed line on a basemap from GeoMappApp. Seismic epicenters vary by color according to year to show swarm events and slightly by size that varies by magnitude. B) A zoomed-in section of the BSZ showing NE-striking fault zones within the NW-trending BSZ. C) A map-view model that illustrates a simplified BSZ and suggests a deeper dextral slip shear zone driving the sinistral faulting. C) A 3D block model conceptualizes the model with a blue block for the subsurface shear zone and green fault planes above where the active seismicity occurs. A decollment surface is between the two strain modes.

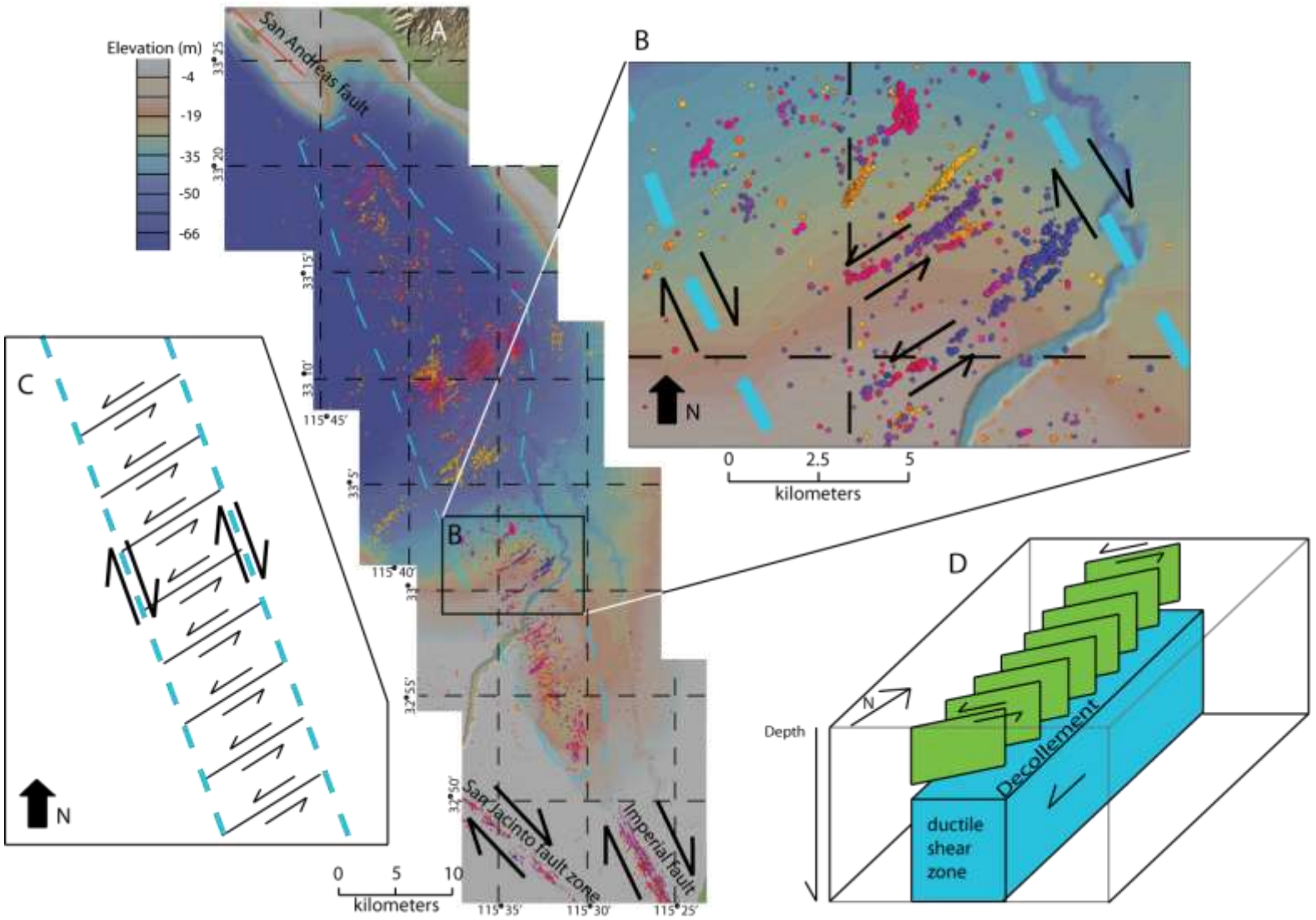
Elevation (m)
-4
-19
-35
-50
-66
A
San Andreas fault
33°25'
33°20'
33°15'
33°10'
33°5'
33°
32°55'
32°50'
115°45'
115°40'
115°35'
115°30'
115°25'
B
N
0
2.5
5
kilometers
C
N
0
5
10
kilometers
B
San Jacinto fault zone
Imperial fault
D
N
Depth
Decollement
ductile
shear
zone

the Brawley Seismic zone (Fig. 31). Epicenters from a swarm event on a relatively continuous north-northwest-striking dextral fault are crossed by several smaller northeast-striking sinistral faults (Fig. 31). Careful investigation suggests that the north-northwest-striking dextral fault is producing epicenters more deeply than the northeast-striking left-lateral faults that produced the seismicity of the northeast-trending epicenter lineaments (Fig. 31 A). The northeast-striking faults appear to cross over the right-lateral fault while both faults are active (Fig. 31 A). Perhaps a similar, larger-scale version of this relationship exists between strands of the Clark fault and the Extra fault array (Fig. 2).

Holocene sediment and fault activity

Character of the thin to absent Holocene sediment in the field area

Exposures of the underlying Brawley Formation in the field area are obscured in many places by a thin and discontinuous layer of Holocene sediment, particularly along gullies and San Sebastian marsh and in low lying areas in between sinsitral faults (Fig. 3). Holocene sedimentary facies include eolian, fluvial and lacustrine from the Holocene Lake Cahuilla that covered the region as recently as 300 years ago (Waters, 1983; Sharp et al., 1989). Holocene deposits are usually flat lying and, undeformed and lie unconformably on the Pleistocene Brawley Formation. Faulting and tilting of the Holocene sediment is localized in active fault zones. The unconformity represents about 1 Ma of erosion from Late Pleistocene to Late Holocene.

Lake Cahuilla rose and fell episodically several times in the Late Holocene with a maximum shoreline elevation at 12 meters (Sharp et al., 1989; Kirby, 2005). Most Lake

Figure 31: A small section of the BSZ showing crossing microseismic swarms. A) Epicenters are colored according to depth with two polygons outlining a N-S trending lineament and a NE-trending group of more shallow lineaments that are partially continuous over the N-S striking fault. B) The same fault zones but with epicenters varying color by year and size by magnitude. The two groups are circled again to show that they are individual swarm events that took place at different times and cross at different depths. The highlighted blue swarm event occurred in 1981 and the orange event occurred in 1987.

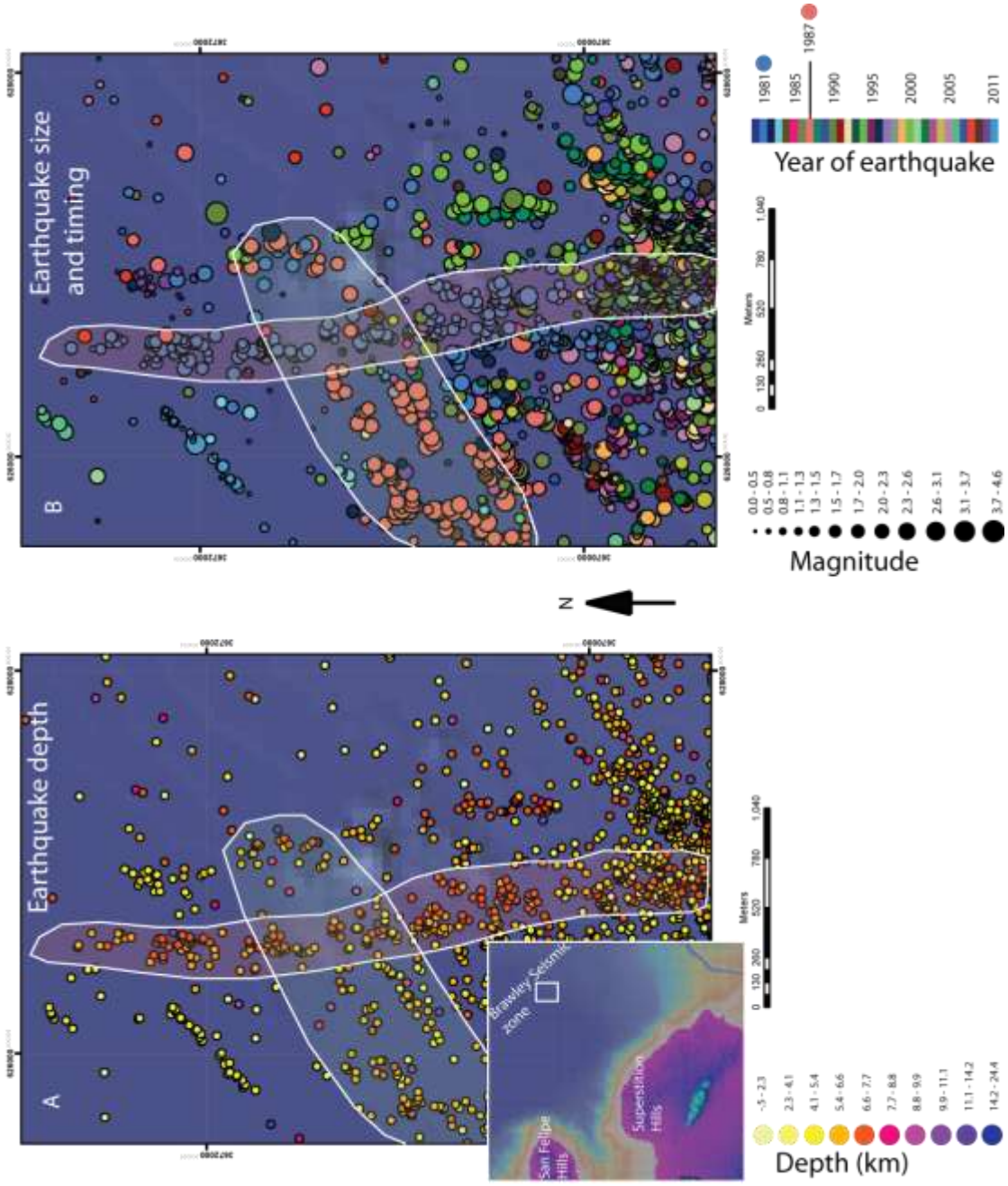
Earthquake size and timing
B
Year of earthquake
1981
1985
1987
1990
1995
2000
2005
2011
Meters
0 130 260 520 780 1,040
Magnitude
0.0 - 0.5
0.5 - 0.8
0.8 - 1.1
1.1 - 1.3
1.3 - 1.5
1.5 - 1.7
1.7 - 2.0
2.0 - 2.3
2.3 - 2.6
2.6 - 3.1
3.1 - 3.7
3.7 - 4.6
N
Earthquake depth
A
Bradley Seismic zone
Superstition Hills
San Felipe Hills
Depth (km)
-.5 - 2.3
2.3 - 4.1
4.1 - 5.4
5.4 - 6.6
6.6 - 7.7
7.7 - 8.8
8.8 - 9.9
9.9 - 11.1
11.1 - 14.2
14.2 - 24.4

Cahuilla deep-water deposits form thin (~20 cm or less) beds but some thicker fine-grained deposits are inconclusively Lake Cahuilla deposits. West of the subsidence boundary the thicknesses seem to increase greatly. Very fine grain size, occasional shells, and a muted greenish-grey color help identify the beds. Sometimes the beds appear greenish or an odd grey color. Regardless of exact color, they stand out in stark contrast to the C-suite Brawley Formation.

Most of the field area is below the highstand shoreline of Holocene Lake Cahuilla and the field area and may be expected to expose mostly Holocene lakebeds and eolian deposits (e.g. Dibblee, 1954). Only a thin ~2 – 100cm veneer of rounded plutonic pebbles and cobbles weathering out of sand and rock from the Peninsular Ranges and what appears to be re-worked mudstone covers the Sebastian uplift (Plate 1). The re-worked mudstone is sediment that was originally deposited as part of the Brawley Formation but has been picked up by Holocene fluvial systems and re-deposited unconformably over the Brawley Formation. West of the Sebastian uplift are thick Holocene lacustrine, playa, fluvial and eolian sediments with no exposed contacts of the Pleistocene rock (Fig. 2; Plate 1).

When cut by younger faults, the Holocene deposits are typically offset only small amounts and remains flat lying. Along some faults with high amounts of Holocene activity (e.g. the Extra fault), Holocene strata are tilted as much as 15° near the faults and bend back to horizontal typically within ~10 meters away from the fault. Besides these shallow folds near the highly active faults, we identified no other evidence for folding of Holocene sediments.

Dunes are active in the field area but there are also ancient dune deposits that form interbeds between deeper water deposits of Holocene Lake Cahuilla. Typically less than a meter thick, the ancient dune deposits are identified by cross bedding and concentrations of mica on the dunes slip face. Modern dunes are typically coppice dunes that form around specific types of vegetation including tamarisk and mesquite that are common in the field area. Typically an isolated plant or groups of plants are centered on the top of an isolated dune. In some small areas, coppice dunes concentrate in groups forming large and extensive dune fields or mounds. Dunes within the thick Holocene sediment are sporadically dispersed with no apparent control, probably because of the high amounts of vegetation. The dunes do not form as commonly on the Brawley mudstone because of limited tamarisk growth near active drainages. Because they are less common in the Brawley Formation, concentrations of dunes stand out as anomalous in several locations. Most dune fields in the exposed Brawley Formation are isolated within a fault zone or section of a fault zone. Small isolated dune fields form on the uplifted centers of domes in sandstone and siltstone that is coarser than typical red-brown mudstone of the Brawley Formation. The reason for limited dune formation is probably the relative impermeability of the Brawley Formation mudstone, limiting large vegetation growth. Faults may provide areas of fluid transport, allowing for larger plant growth and finally dune field formation. The section of the Extra fault with the large dune field is within an area of moderate Holocene cover, so the combination of unconsolidated sediment that is faulted is ideal for fluid flow and large plant growth.

Shoreline features include a large spit, shoreline scarps and beach sediments. The spit provides one of the primary topographic features in the area. It extends roughly north-south for almost 2.5 km, is as much as 200 meters wide and approximately 6 meters high (Plate 1). Shorelines often form small scarps that can be confused with tectonic scarps. Scarps are assumed to be shoreline related if they parallel topography, follow topography, are within beach deposits and do not display any truncated bedding. Identifying these is not a challenge in the field but proves difficult from imagery. Two primary types of beach deposit were identified. The first consists of rounded plutonic pebbles and some cobbles without any cementation or cohesion of any type. Some thick deposits were found in small graven but typically only form a small layer. A second type of beach deposit was identified in only two locations and was not differentiated in mapping. It consists of much smaller plutonic grains and some small gravel size rocks. They are held together with calcareous gray color cement. Shoreline deposits are evident in most of the field area but not within active Holocene sedimentation. They are most pronounced in areas with abrupt topography changes.

Geochronology

Optically stimulated luminescence

Two samples from the Extra fault zone were collected and processed at the Utah State University Optically Stimulated Luminescence (OSL) lab. Sample number USU 933 was collected from Eight-Mile Wash (Fig. 11 B). The sample was collected from a Holocene sand interbed within Lake Cahuilla intervals that were deposited about 20cm above the Extra fault. The dated sand bed overlay Holocene sediments that are cut by the

Extra fault. Dating the sand layer provides a minimum date of last activity on this strand of the Extra fault. Results from 22 aliquots was 0.7 +/- 0.29 ka (Table 2). The aliquots were in good agreement; error could be reduced with more aliquots. Sample number USU 932 was collected from an exposure about 150 meters south of highway 78 (Fig. 11 A) from a sand layer that is juxtaposed next to the Brawley Formation by the fault. Results from 22 aliquots produced an age of 10.64 +/- 1.98 ka (Table 2). Dating this sand deposit provides a maximum age constraint of last activity of this strand of the fault.

Radiocarbon dates

Occasional concentrations of detrital charcoal are scattered throughout Holocene Sand deposits and may represent hearths of native people. One sample was collected from the same horizon as was sampled by OSL sample number 932 for validation of the OSL methods in the dune sands of the Salton Trough (Fig. 11 B). Tom Rockwell processed the radiocarbon sample. Age determinations were made at the University of California, Irving. Radiocarbon results returned an age of 975 +/- 15 years BP. The OSL and radiocarbon methods agree within error and the radiocarbon helps confirm that the preliminary OSL results are acceptable. This date indicates that this strand of the Extra fault last slipped sometime before ~1000 years ago (Table 2).

GEOPHYSICAL RESULTS IN THE EXTRA FAULT ARRAY

The Extra fault array coincides with a gap in microseismicity along the San Jacinto fault zone

We tested whether there is a continuous strand of the Clark fault through and beneath the Extra fault array by examining the microseismic patterns in the field area and

exploring their relationships to mapped faults. Microseismicity is prevalent along most of the San Jacinto fault zone, and this fault is well known for the continuous production of small earthquakes along its trace (Sanders and Magistrale, 1986; Magistrale, 2002; Wdowinski, 2009; Hauksson et al., 2012; Yang et al., 2012) and the large volume of its damage zone (Lin et al., 2007; Yang et al., 2012). The Clark fault directly northwest of the field area typically produces seismic activity between 8-10 km deep and the dominant and maximum depth of small earthquakes increases northwestward to about 16 km (Fig. 32; Peterson et al., 1991; Lin et al., 2007). Shallower seismicity near the Clark fault in the San Felipe Hills is primarily associated with cross faults that strike perpendicular to faults of the San Jacinto fault (Peterson et al., 1991; Belgarde, 2007).

The San Jacinto fault zone has historically been the most microseismically active fault zone in California, so quiet sections stand out in contrast to the rest of the fault zone (Fig. 32; Sanders et al., 1986; Yang et al., 2012). A sizable area that lacks such microseismicity coincides with the Extra fault array and encompasses much of this study area. The quiet area continues northeast along strike as far as the San Andreas fault (Fig. 32).

Considering the dominance of northeast-striking left-lateral faults in the field area and the abundant evidence for historic and Holocene slip, this gap in the microseismicity along the Extra fault array is unexpected. No northeast-trending alignments of microseismic swarms formed along the fault zones in the Extra fault array between 1981 year and 2011 with only a few isolated events (Yang et al., 2012; Fig. 32). The quiet area is sizable, including the entire Extra fault array at ~300 sq. km. Another sizable quiet

Figure 32: A microseismically quiet section of the San Jacinto fault zone. Earthquake hypocenters vary size by magnitude and color by depth. Seismicity in the San Felipe Hills and Superstition Hills extends several kilometers to the NE. Seismicity within the field area is extremely limited and forms no NE-trending lineaments associated with the Extra fault array. Directly south of the field area is an area of limited seismicity that forms some NE-trending lineaments that project toward the Coyote Creek fault.

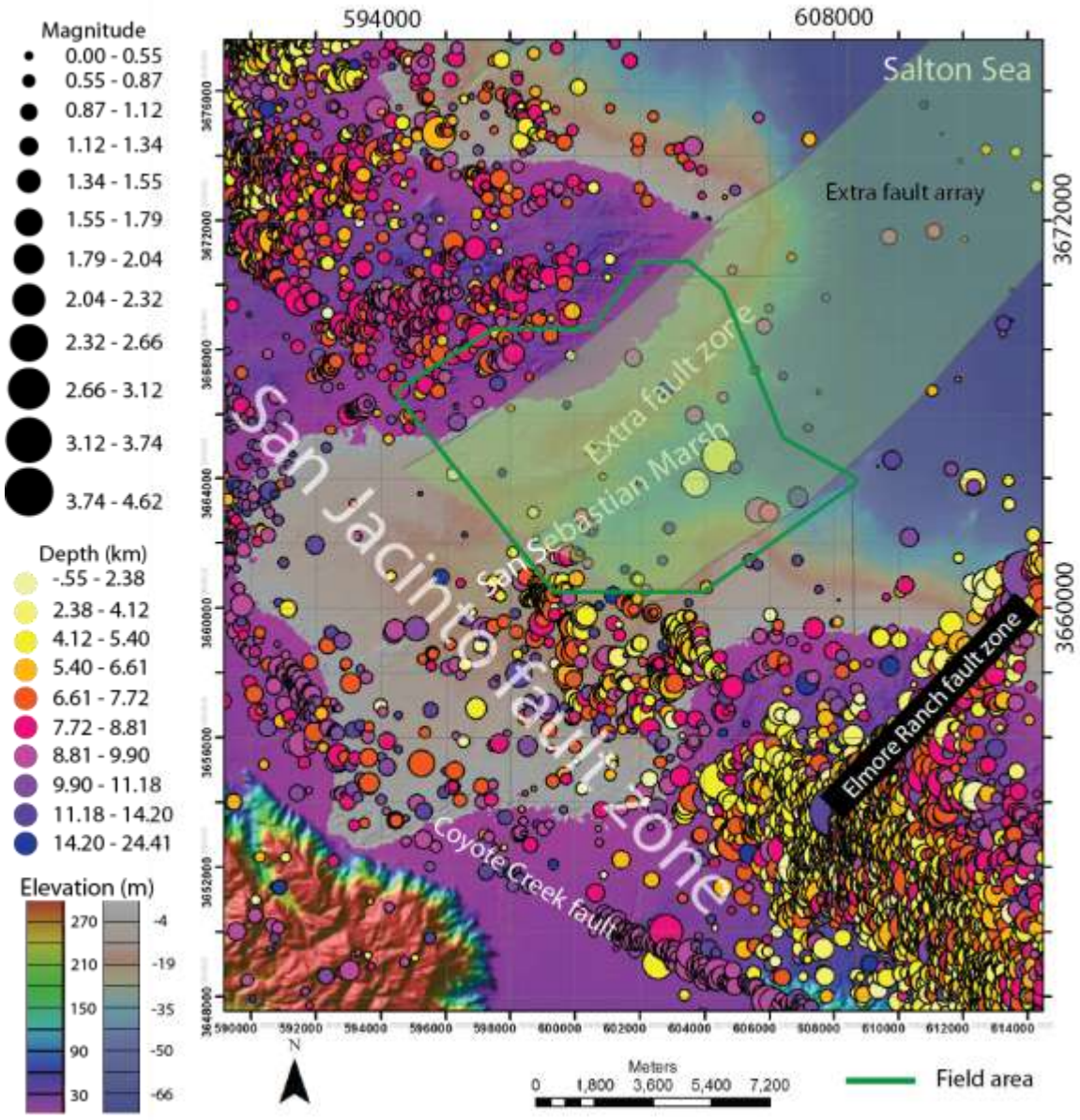
Magnitude
0.00 - 0.55
0.55 - 0.87
0.87 - 1.12
1.12 - 1.34
1.34 - 1.55
1.55 - 1.79
1.79 - 2.04
2.04 - 2.32
2.32 - 2.66
2.66 - 3.12
3.12 - 3.74
3.74 - 4.62
Depth (km)
-.55 - 2.38
2.38 - 4.12
4.12 - 5.40
5.40 - 6.61
6.61 - 7.72
7.72 - 8.81
8.81 - 9.90
9.90 - 11.18
11.18 - 14.20
14.20 - 24.41
Elevation (m)
270
210
150
90
30
-4
-19
-35
-50
-66
594000
608000
3672000
3660000
Salton Sea
Extra fault array
Extra fault zone
San Sebastian Marsh
San Jacinto fault zone
Elmore Ranch fault zone
Coyote Creek fault
N
Meters
0 1,800 3,600 5,400 7,200
Field area

zone, with a northwest elongate shape, is centered on the San Felipe Hills fault (Belgarde, 2007).

Microseismic swarms

Microseismic swarms are composed of numerous microearthquakes that are related both spatially and temporally. Microeathquakes within a swarm occur in close proximity and within a short time of others associated with the swarm. Microseismic swarms are common throughout the area of the datasets used (Hauksson et al., 2012; Yang et al., 2012). The majority of swarms occur within the Brawley Seismic zone (Figs. 1 and 30) although they do occur in less abundance elsewhere in the southern San Andreas fault system. Most swarms form microseismic alignments along the two predominant fault strikes toward the northwest and NE. The Brawley seismic zone swarms occur primarily as NE-trending lineations. Depths of the swarm events vary between 0 and 30 km with a majority between 4 and 8 km (Hauksson et al., 2012). The lengths of the swarms in map view are about 2 to 6 km on average (Fig. 30). Most events occur within a time span of a couple of months, respectively, but spatially related events can be separated by as much as 3 years.

Typically swarm events are associated with fluid flow and can occur within seismogenic or ductile regimes in the subsurface (Sibson, 1996). The Brawley seismic zone in particular appears to be what Sibson (1996) refers to as a mesh structure that connects the San Andreas fault with the Imperial fault. Mesh structures that form a link between major faults can form swarms orthogonal to the primary slip vector as observed in the Brawley seismic zone (Sibson, 1996). The fluid migration causing shallow swarm

activity within the Brawley seismic zone is likely due to geothermal activity but could have anthropogenic or magmatic affects (Spicak, 2000). The shallow swarm events support a geothermal mechanism because the entire Salton Sea geothermal area is restricted to Pliocene and Quaternary rock and sediment (Muffler and White, 1969). Those events that are deeper than perhaps 7 km are probably not related to fluid migration within the Salton Sea geothermal area (Muffler and White, 1969). Perhaps these events are caused by deeper ductile magmatism that applies concentrated stress and forms similar swarms to those caused by geothermal fluid flow (Spicak, 2000).

The Salton Sea geothermal area has temperatures up to 360° C at a depth of 2164 meters with metamorphism of the sediments to the greenschist facies (Muffler and White, 1969). Heat transfer within the system occurs primarily as fluid convection (Helgeson, 1968), which also supports geothermal fluid flow as the mechanism for the shallow microseismic swarm development in the Brawley seismic zone.

Northwest-trending alignments of epicenters are roughly along strike of the Clark fault zone

Although there is relatively little microseismicity in the Extra fault array, there is an area of marked aligned microseismicity near the southwest edge of the field area (Fig. 33). There are two swarm events that are the most obvious microseismic features of the field area (Fig. 32). These swarms are separate from the microseismicity that is localized along the Brawley seismic zone (Figs. 30 and 32) and they are likely not tied to the same geothermal fluid flow. The mechanism for fluid flow through rocks that produced these swarms of earthquakes is unclear as there is no geothermal production in the field area

and no surface evidence for hydrothermal activity. Perhaps these swarms are the result of magmatic heat and ductile movement.

The larger of the two prominent swarms in the study area occurred in 2008 with over 100 individual events and is about 4 km north of the Superstition Hills (Fig. 33 C; Hudnut et al., 1989a; Sharp et al., 1989). The other prominent swarm occurred in 2007 and is near the confluence of San Felipe wash and Carrizo wash, near the middle of the San Sebastian Marsh area (Fig. 33 B). Other microseismic events – including from these two years – occurred almost exclusively to the southwest of the 2007 and 2008 swarms (Fig. 33). Subtle microseismic alignments suggest possible northeast-striking left-lateral cross faults between the Coyote Creek fault and these swarm events of 2007 and 2008 (Fig. 33 A).

Although the 2007 and 2008 microseismic swarms trend northwest, fault traces on the surface primarily strike N 60° E and are continuous over the hypocenter locations of the swarms (Fig. 5). Possibly six active fault zones of the Elmore Ranch fault array form continuous traces over the seismic lineament (Thornock and Janecke, unpublished data). The narrow 2007 and 2008 swarm events roughly correlate spatially with the location that the left-lateral faults of the Extra fault array change strike back to ~20° from ~60° at the western side of the field area (Fig. 25, see above). The alignment of hypocenters of the 2007 and 2008 swarms are at depths of about 4-8 km and might represent a fault in the subsurface that strikes N 45° W, apparently below faults that oriented orthogonally to it at the surface (Fig. 33).

Figure 33: Microseismic swarms in the field area. A) Seismic epicenters that vary size with magnitude and color with the year the event took place. The three primary years of interest are 1987 salmon colored epicenters and the 2007-2008 swarms that form NW-trending faults in part B. B) Only the microearthquakes that took place in 2007 and 2008. SW of the 2007-2008 swarms is slightly increased seismic activity compared to NE of the swarm events. These epicenters SW of the swarm events form subtle NE-trending lineaments toward the Coyote Creek fault. C) A zoomed in view around just the 2008 swarm but shows hypocenters from every year recorded in the data.

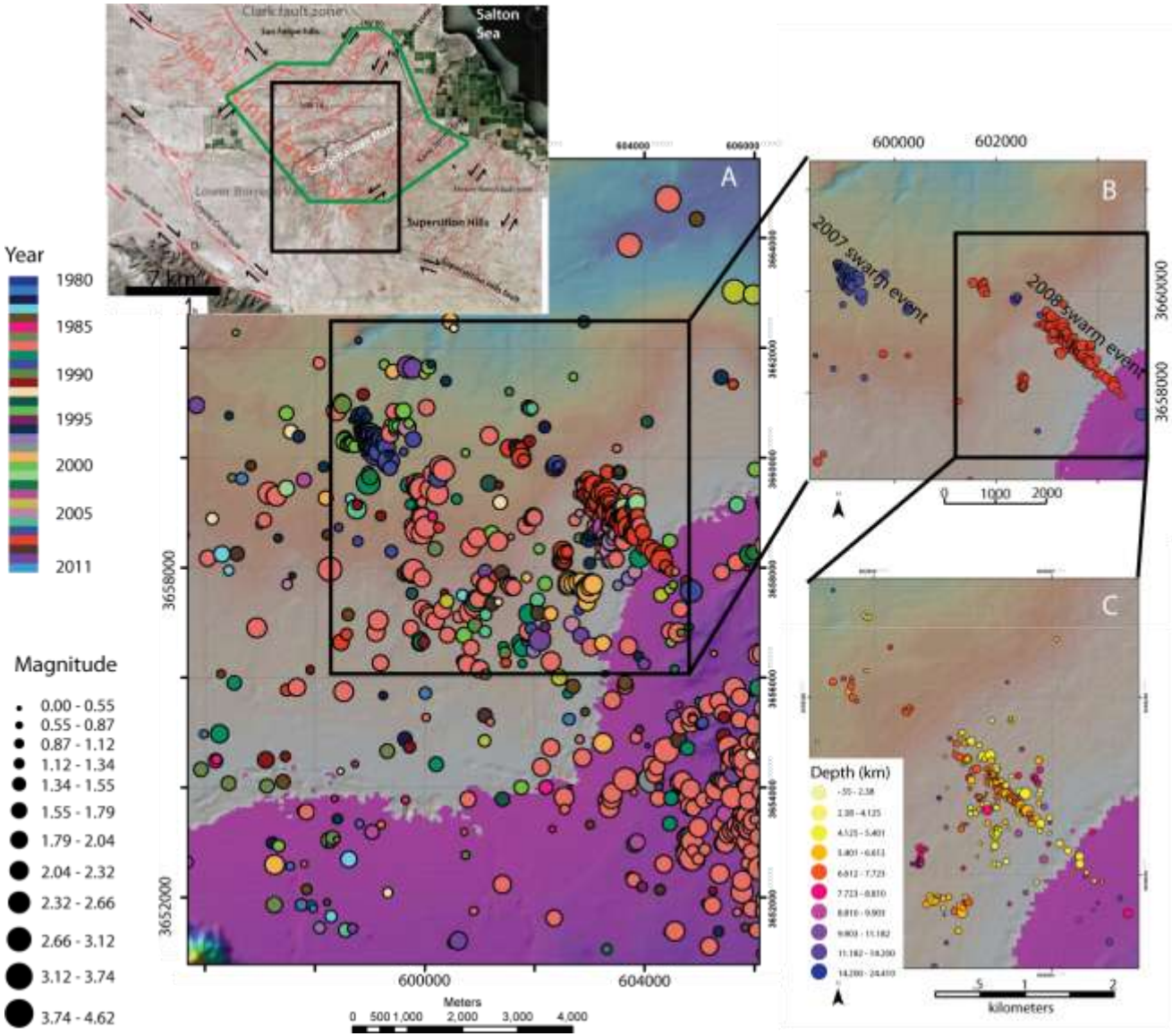
Clark fault zone
Salton Sea
Superstition Hills
7 km
Year
1980
1985
1990
1995
2000
2005
2011
Magnitude
0.00 - 0.55
0.55 - 0.87
0.87 - 1.12
1.12 - 1.34
1.34 - 1.55
1.55 - 1.79
1.79 - 2.04
2.04 - 2.32
2.32 - 2.66
2.66 - 3.12
3.12 - 3.74
3.74 - 4.62
A
B
C
2007 swarm event
2008 swarm event
600000
602000
604000
3658000
3652000
3660000
Meters
0 500 1,000 2,000 3,000 4,000
0 1000 2000
Depth (km)
kilometers

Overall the hypocenters associated with the 2008 swarm shallow toward the southeast where the hypocenters appear to be on a steeply dipping section of the fault (Fig. 33). The northwest end of the hypocenter alignment shows an overall dip direction with more shallow earthquakes that occur on the northeast side of the lineament with deeper ones on the southwest side of the lineament (Fig. 33). If the swarm does represent a fault at depth, a best-fit plane through the hypocenter swarm would represent a fault that dips between 83 and 87° southwest (Fig. 33 C).

Focal Mechanisms with steep northwest-striking nodal planes

The Yang et al. (2012) catalog of relocated focal mechanisms also exhibit a northwest-trending alignment that seems to correlate with the northwest-trending epicenter alignments from 2007 and 2008 (Fig. 14; Hauksson et al., 2012; Yang et al., 2012). The locations of the focal mechanisms are spread over a larger area and are plotted farther to the west when compared to the microseismic swarm events from Hauksson et al. (2012) (Fig. 14). The two data sets probably show the same earthquakes because of similar magnitudes, number of events and the same trend of the aligned swarm event. The two data sets may have used different methods of relocating the data sets. An undetected error may also explain this discrepancy.

Most focal mechanisms along the northwest-trending lineament show predominantly strike-slip motion with very little oblique component (Fig. 31; Yang et al., 2012). Average strike of the mechanisms is 226° and dip of 75° typically to the northeast assuming a northwest-striking active nodal plane (Fig. 14). The average rake is 156° which indicates a strong strike-slip movement regardless of the active nodal plane or

direction of oblique slip. Normal components of slip are slightly more common than reverse components (Fig. 14). The focal mechanisms form a well-defined northwest trending alignment and the dip directions of focal mechanisms alternate from northeast to southwest and the strikes varies within ~30° toward the northwest (Fig. 14; Yang et al., 2012).

Published InSAR shows strains on some faults

Geophysical imagery, including pre-processed gravity and Interferometric Synthetic Radar (InSAR) images were also interpreted in this study to help identify possible faults in the field area (Lundgren et al., 2009; Lyons and Sandwell, 2003; Mellors and Boisvert, 2003; Mellors et al., 2005; Tong et al., 2011; Van Zandt et al., 2004; Wei et al., 2009). Mellors et al. (2005) identified an anomaly from InSAR of particular importance to this study (Fig. 18 A). Their work indicates a northwest-trending subsidence boundary that correlates roughly with the southwest boundary of the field area (Fig. 18). The southwestern section of the subsidence boundary is bound by the Superstition Hills fault (Fig. 18). The subsidence boundary continues to the northwest toward the Clark fault, passing by the northeast side of the Allegretti farms (Fig. 18). Although no fault is evident between the Clark fault and the Elmore Ranch fault in the field, the subsidence boundary indicates the possible presence of a northwest-striking fault at this location. Mellors et al. (2005) noticed this structure and drew in a dashed line between the Clark fault and Superstition Hills fault indicating a fault at depth that is not evident on the surface (Fig. 18; Mellors and Boisvart, 2003; Fialko, 2006; Wei et al., 2009).

Some InSAR images also show sharp, straight lineaments near Allegretti Farms (Mellors and Boisvert, 2003; Wei et al., 2009). One trends to the southeast on the southwest side of Allegretti Farms, paralleling the primary subsidence boundary (Fig. 18 A). Another straight lineament controls the east-southeast edge of the strong subsidence under Allegretti Farms and trends to the northeast, revealing a more north-northeast-striking part of the merged Bondit-Shoreline fault (Fig. 7 and 18 A). The two lineaments meet at a point south of Allegretti Farms. Tom Rockwell and his students mapped the northwest-striking fault for at least another 5 km southeast of this intersection (Tom Rockwell, written communication; Fig. 18). The geometry of Rockwell's fault projects toward the northwest end of the Superstition Hills fault but several NE-striking sinisitral faults interfere (Fig. 1).

GEOMORPHIC ASPECTS OF THE STUDY AREA

Exhuming basin-fill is localized in a northwest-trending zone that is centered on the Clark fault zone

One of the most important pieces of evidence for the continuity of the Clark fault through the Extra fault array to the Superstition Hills fault is in the presence of a continuous broad uplift that extends from the southern 20-30 km of the Clark fault zone through the intervening area of our study to the Superstition Hills (Fig. 34). Previously recognized uplifts of the San Felipe and Superstition Hills (Dibblee, 1954, 1984; Sharp et al., 1989; Kirby, 2005) are the most uplifted parts of this much broader structural high (Fig. 2).

Figure 34: Outline of the Sebastian uplift. The Sebastian uplift of exposed Late Miocene – Late Pleistocene deposits is outlined in black. A) Central section of the Sebastian uplift centered around the Sebastian Marsh. Faults are in red, notice the majority of northeast-striking faults on the Sebastian uplift that trends northwest. B) A regional view of the Sebastian uplift that is split roughly between the southern Clark fault zone in darker brown and the Coyote Creek fault in lighter brown. The basemap for part A is from 2012 Digital Globe imagery in Google Earth and part B is a processed landsat image.

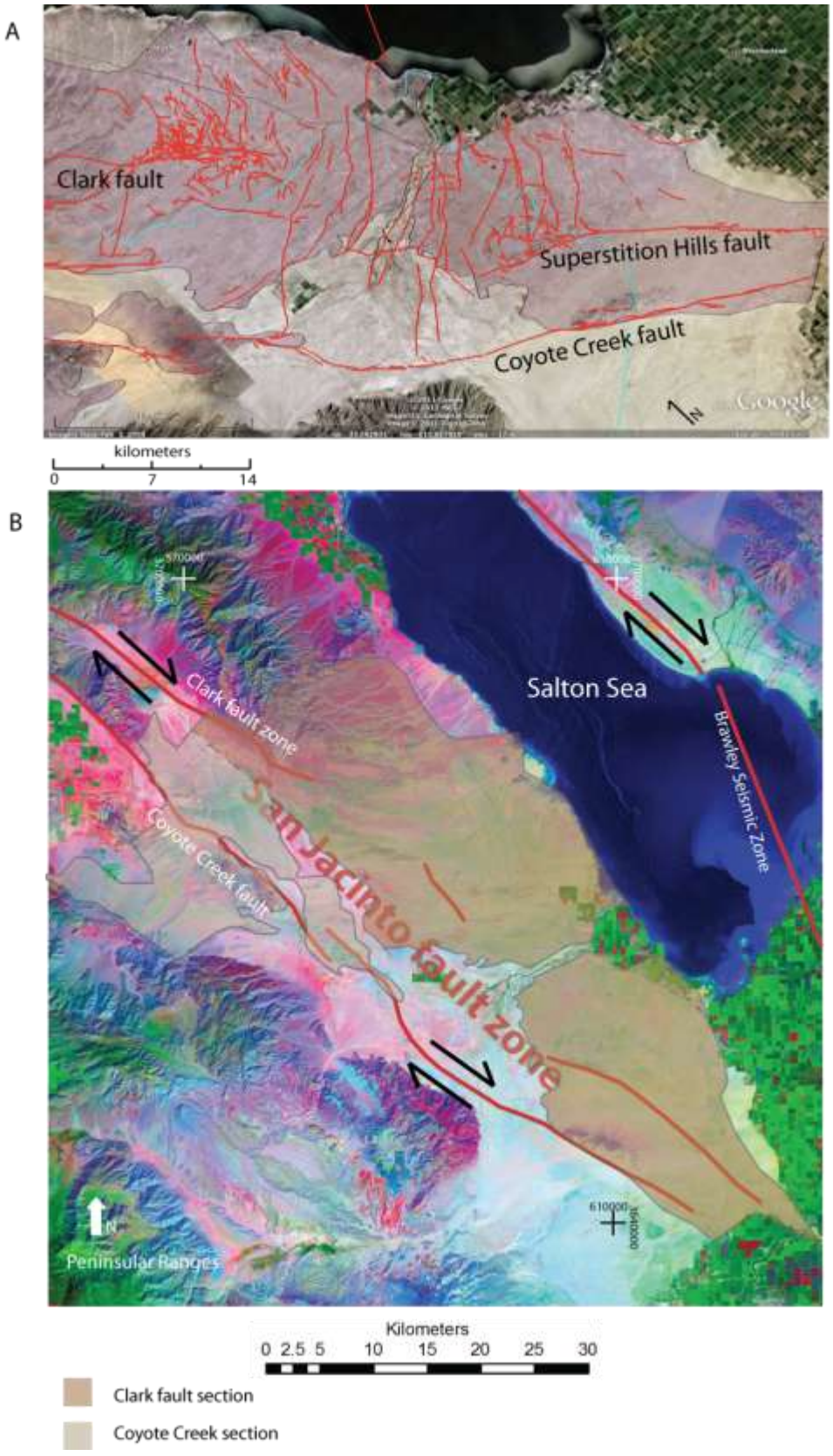
A
Clark fault
Superstition Hills fault
Coyote Creek fault
Google
kilometers
0 7 14
B
Salton Sea
Clark fault zone
Coyote Creek fault
San Jacinto fault zone
Brawley Seismic Zone
Peninsular Ranges
Kilometers
0 2.5 5 10 15 20 25 30
Clark fault section
Coyote Creek section

Previous maps interpreted the San Sebastian Marsh area, at the center of the newly identified uplift, as covered by Holocene sediment (Dibblee, 1954, 1984, 1996). The field area around San Sebastian Marsh is instead underlain by expansive deformed Pleistocene sediment and is a continuation of an uplift that connects the San Felipe Hills to the Superstition Hills (Fig. 34). We chose the name Sebastian uplift for this major region of exhumed basin fill because it is centered on San Sebastian Marsh and our discovery of the uplift occurred in the marsh (Fig. 34). The northwestern edge of the uplifted basin fill is along the West Salton detachment fault and the Borrego Badlands. There are also uplifted Cretaceous plutonic rocks in the footwall of the West Salton detachment fault in the southeast Santa Rosa Mountains (Fig. 34; Sharp, 1967; Belgarde, 2007). The Sebastian uplift slowly decreases in altitude southeast of the San Felipe Hills and is covered by Holocene sediment in a narrow band parallel to and bisected by the San Felipe Wash in the field area (Fig. 2 and Plate 1). Exhumed Pleistocene sediment reappears less than 1 km southeast of San Felipe Wash and persist southeast to the Superstition Hills (Fig. 2 and Plate 1).

The main mass of the Sebastian uplift is extensively faulted and folded and exposes sediment as old as the latest Miocene Imperial Formation (Fig. 34; Dibblee, 1954; Rogers, 1965; Reitz, 1977; Kirby, 2005; Kirby et al., 2007). In order to expose the Imperial Formation about 4 km of younger sediment must have been eroded (Winker and Kidwell, 1996; Dorsey, 2006; Dorsey et al., 2011). The Marsh coincides with a structurally least uplifted region within the Sebastian uplift and coincides with a broad

structural saddle and does not expose pre-Pleistocene sedimentary rocks (Plate 1, this study).

Overall the northwest-trending Sebastian uplift extends northwest to southeast for about 70 kilometers and is localized around the Clark fault zone in the San Felipe Hills and the Superstition Hills fault to the southeast (Fig. 34). The spatial association between these structures suggests that the presence of active Sebastian uplift is probably due to strain around the Clark fault zone in the northwest and the Superstition Hills and Superstition Mountains faults to the southeast (Fig. 34). The hypothesized association between the Sebastian uplift and the Clark fault is strengthened by the spatial overlap of the Sebastian uplift with the domains of possible clockwise rotation of preexisting sinistral faults in the central and transitional fault domains in the field (Fig. 25). Major strands of the Clark and Superstition Hills dextral fault zones are localized along the southwest edge and near the central axis of the Sebastian uplift, producing the asymmetric geometry of the Sebastian uplift (Fig. 34). The faults exposed within the Sebastian uplift strike primarily northeast and thus they are unlikely be the source of the northwest-trending uplift. Northeast-striking left-lateral faults are continuous on the northeast and southwest sides of the Sebastian uplift beneath the Salton Sea and in the Holocene depocenter of Lower Borrego Valley (Plate 1).

Minimal amounts of incision are found on the main uplift where San Felipe Wash crosses it and there is even some evidence for cut and fill terraces there (Fig. 34). The San Felipe wash in the Sebastian Marsh area must be incising the Sebastian uplift as quickly as it is uplifting, keeping the uplift at the local base level and at the same

elevation with Holocene sediment west and east of this section of the uplift (Fig. 34). Similar low levels of incision characterize most of the uplift except at its northernmost end in the southeast Santa Rosa Mountains where the deepest and most incised canyons are (Belgarde, 2007).

Irregular hourglass shape of the Sebastian uplift

The map pattern and width of the Sebastian uplift resembles an hourglass shape with narrow tips that thicken then narrow again approaching the center of the hourglass around San Sebastian Marsh (Fig. 34). The widest part is in the south, in the Superstition Hills and is ~16 kilometers (Fig. 34). The widest part in the north is ~ 20 kilometers wide in the San Felipe Hills (Fig. 34). The narrow middle of the hourglass shape is only about 6 km wide near San Sebastian Marsh. The two wide parts of the uplift correlate with the Superstition Hills and the San Felipe Hills (Fig. 34).

The southwest edge of the Sebastian uplift in the field area roughly coincides with the alignment of microseismic swarms from 2007 and 2008 (Fig. 33), the location of strike changes of left-lateral faults between the southwest and the central domains (Fig. 25), gravity data showing a major southwest-down step in the basement there (Langenheim and Rittenour, 2011), and an irregular deformational boundary on several InSAR interferograms (Fig. 18 A; Mellors and Boisvert, 2003; Van Zandt et al., 2004; Wei et al., 2009; Tong et al., 2011). These data all indicate a possible northwest-striking dextral fault zone along the southwest edge of the Sebastian uplift in the field area (Fig. 34). The hypothesized buried dextral-normal fault zone may be a less active fault that is similar to the Superstition Hills or Superstition Mountains dextral faults (Sharp et al.,

1989). The jagged western edge of the Sebastian uplift in the field area, as defined by the maximum extent of Pleistocene rocks, is possibly due to cross-cutting sinistral faults. This would imply coeval or alternating activity of uplift with left-lateral and right-lateral faults. The northeast margin of the Sebastian uplift is not well exposed along this section but appears to be a northeast-dipping homocline of the upper part of the Pleistocene Brawley Formation along most of its extent (Dibblee, 1954, 1984; Kirby et al., 2007, this study). Small-offset north-northeast-striking left-normal faults cut this homocline but do not define its margin (Dronyk, 1977; Kirby et al., 2007).

Superstition Hills-Superstition Mountain part of the Sebastian uplift

The Superstition Hills received significant attention at the time of the Elmore Ranch earthquake in 1987 but the only geologic map of rock units dates back to much earlier (Dibblee, 1954, 1984a and b; Hudnut et al., 1989a; Sharp et al., 1989). The north and east boundary of the Hills is the shoreline of ancient Lake Cahuilla at 13 meters above sea level. The hills are variable in their topography reaching as high as about 72 meters.

Sediments exposed in the Superstition Hills consist primarily of Pleistocene Brawley Formation, Ocotillo Formation, and possibly the underlying Pliocene Borrego Formation in the faulted anticline at the structural core of the hills (Fig. 3; Dibblee, 1954, 1984; Sharp et al., 1989; Janecke and Pendelton, unpublished mapping). The Superstition Hills are interpreted as a faulted anticline on an east-west trending reflection seismic line (Severson, 1987). Janecke interprets the data in Severson (1987) as showing the presence of a fairly significant east or northeast dipping fault on the east flank of the

Superstition Hills, near Highway 86 (personal communication). A component of northeast-down motion is likely across this fault and it may be an en echelon strand of the Clark fault (Fig. 27; see below). The southwestern boundary of Superstition Hill is the Superstition Hills fault (Fig. 2; Dibblee, 1954, 1984; Sharp et al., 1989).

In detail, there are many small and modest left-lateral, right-lateral and normal faults, and nearly as many folds in the broad anticline of the Superstition Hills (Fig. 2; Sharp et al., 1989; Klinger and Rockwell, 1989). The most deeply exhumed areas are adjacent to the Superstition Hills fault on the southwest margin of the hills (Fig. 2). The Superstition Hills are laced by about five anastomosing faults of the left-lateral Elmore Ranch fault array (Fig. 4). Exposed and uplifted basin-fill of the Sebastian uplift persists farther southwest to the Superstition Mountains fault (Fig. 34). The Superstition Mountains fault bounds the Superstition Mountains on the southwest and locally there is so much uplift along the fault that crystalline basement is exposed (Dibblee, 1954; Rogers, 1965; Bjornstad et al., 2006).

San Felipe Hills part of the Sebastian uplift

The San Felipe Hills are another major topographic high in the low Imperial Valley region (Fig. 1). The 13-meter elevation surface that defines the highstand shoreline of Lake Cahuilla lies roughly along the southern boundary of the San Felipe Hills (Fig. 2). The elevation varies greatly in the hills but stays above the shoreline level and reaches as high as about 60 meters elevation. Exposed sediment in the region consists primarily of the Diablo Formation and includes some Brawley Formation, Imperial Formation, Ocotillo Formation, and Borrego Formation (Fig. 3; Dibblee, 1984a;

Kirby, 2005; Belgrade, 2007). An angular unconformity of the Pleistocene Ocotillo Formation over Pliocene rock is evidence that this region is an overall anticline trending northwest, similar to the Superstition Hills (Fig. 2; Kirby et al., 2007).

Similar to the southwest edge of the Superstition Hills and the section of Sebastian uplift in this field area, the southwest edge of the San Felipe Hills is bounded by the San Felipe Hills fault (Fig. 34) The San Felipe Hills fault is the largest strand of the Tarantula Wash section of the southern Clark fault zone (Fig. 2; Belgarde, 2007; Janecke et al., 2010). The San Felipe Hills fault parallels the Powerline strand of the Clark fault in its most southern extent (Fig. 2). Toward the southeast (Fig. 2) the San Felipe Hills fault ends into northeast-striking left-lateral faults of the Tarantula Wash fault array about 2 km northwest of the field area (Fig. 4).

Anomalously small delta formed downstream of the Sebastian uplift

There is more evidence for the Sebastian uplift in the unusually fine grain size and small aerial extent of the delta of San Felipe Wash immediately downstream of the Sebastian uplift (Fig. 35 A and 36). The San Felipe and Carrizo washes are the two large drainages that converge at San Sebastian Marsh and empty into the Salton Sea east of the field area (Fig. 35). Perennial water flow in the marsh transports sediment gathered from the Peninsular Ranges over a large hydrologic area (Fig. 35 B). The delta formed at the mouth into the Salton Sea consists of fine-grained sediment and about 3 by 8 km, based on the bathymetry at the widest and longest sections of the delta (Fig. 36). The extent of the delta is about the same as those that developed downstream of much smaller drainage

basins like the Tule and Arroyo Salada drainage basins immediately to the north (Fig. 35 A).

Hydrologic areas can consist of several hydrologic units with some sediment trapping in each unit but overall flow to one location. The hydrologic drainage area of the San Felipe – Carrizo basin is 6.6 times the size of the hydrologic drainage that forms the Tule and Arroyo Salada delta (Fig. 35 B). There are several hydrologic units that make up the large San Felipe hydrologic area where sediment can be deposited on the way to the Salton Sea (Fig. 35 B). But even comparing the much smaller San Felipe hydrologic unit at the mouth of the Sea to the Tule – Arroyo hydrologic unit, the San Felipe unit is 2.7 times the size (Fig. 35 C) but form similar size deltas. Sediment at the bottom of the Salton Sea downslope of the delta of San Felipe Wash is dominated by clay and mud, not sand and silt, in marked contrast to the rest of the Salton Sea (Fig. 36 B).

Figure 35: Comparison of Salton Sea deltas near the field area. A) Comparison of the relative size of deltas in the southern Salton Sea based on bathymetry. The delta forming downstream of the small Tule and Arroyo Salada Washes is nearly as large as the delta forming from the large San Felipe Wash. The digital elevation model (DEM) is from GeoMappApp. B) The hydrologic areas that provide sediment to San Felipe Wash and Tule and Arroyo Salada Washes respectively. C) A closer look at the hydrologic unit of San Felipe Wash with relative area compared to Tule and Arroyo Salada Washes. The values for area are only relative numbers calculated in Adobe Illustrator and do not represent typical square area units.

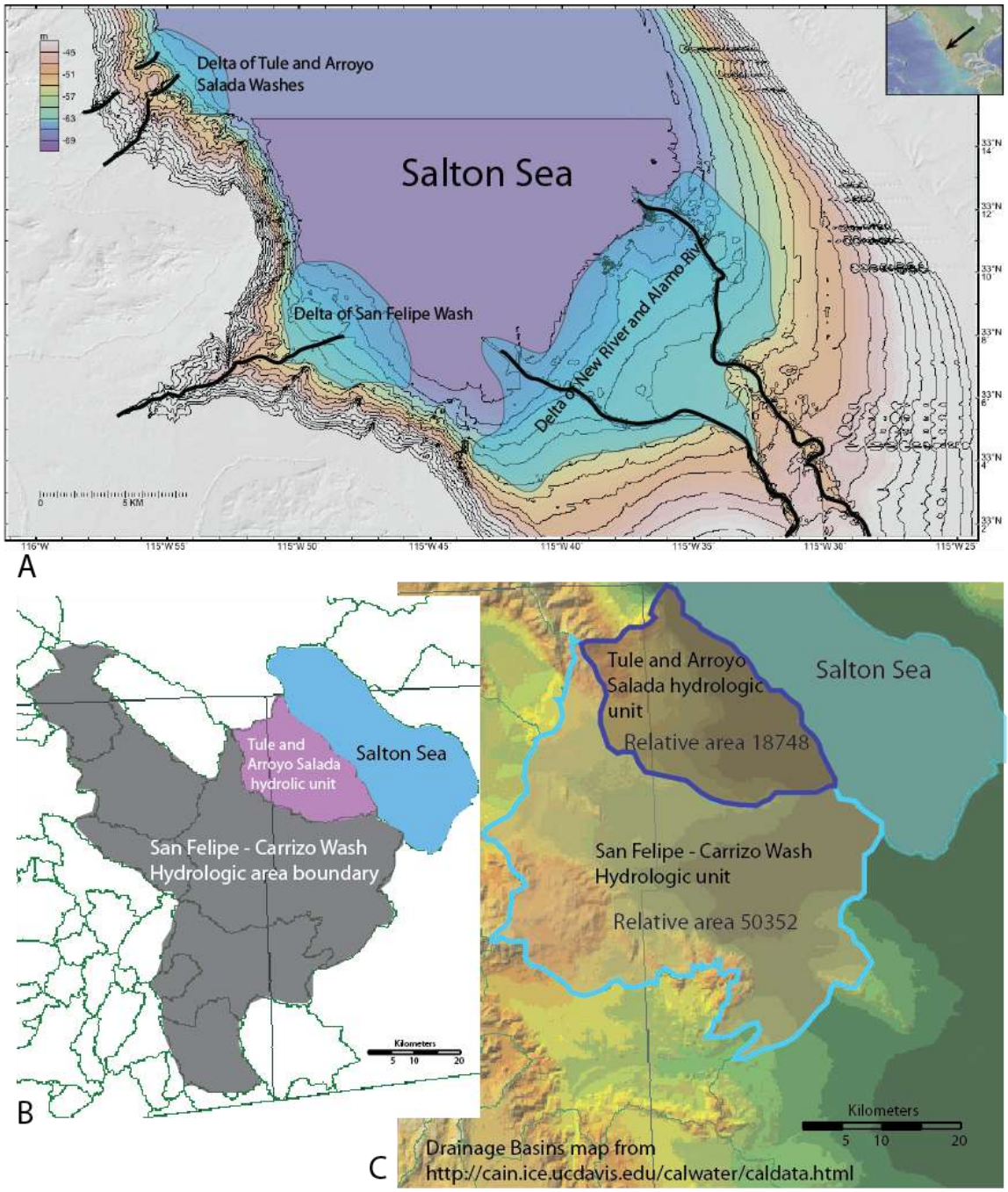
Delta of Tule and Arroyo Salada Washes
Salton Sea
Delta of San Felipe Wash
Delta of New River and Alamo River
A
Tule and Arroyo Salada hydrolic unit
Salton Sea
San Felipe - Carrizo Wash Hydrologic area boundary
B
Tule and Arroyo Salada hydrologic unit
Relative area 18748
Salton Sea
San Felipe - Carrizo Wash Hydrologic unit
Relative area 50352
Kilometers
5 10 20
C
Drainage Basins map from
http://cain.ice.ucdavis.edu/calwater/caldata.html

Figure 36: Bathymetry and clay sediment distribution in the Salton Sea. Both images are from the Salton Sea Atlas by Redlands University. A) A bathymetric image of the Salton Sea. B) The sediment size distribution throughout the sea. Fine grain sediment is represented as blue with a gradational scale coarsening to a brown color. Notice how the sediment is relatively fine at the mouth of San Felipe wash. Most other delta mouths are more dominated by more coarse sediment.

A

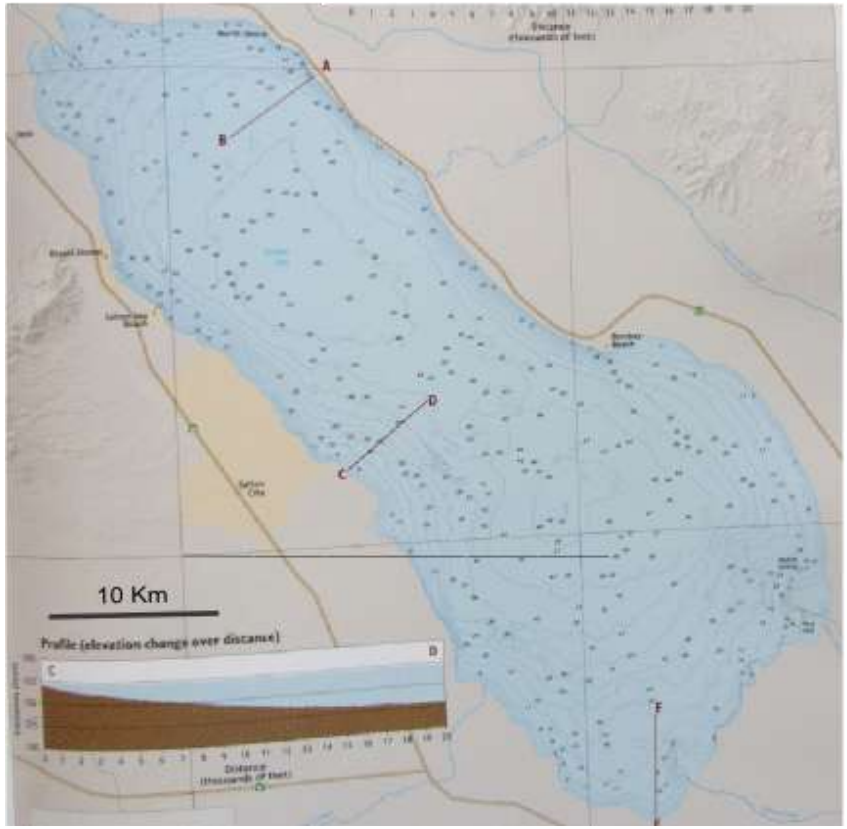
A
B
C
D
E
10 Km
Profile (elevation change over distance)

B

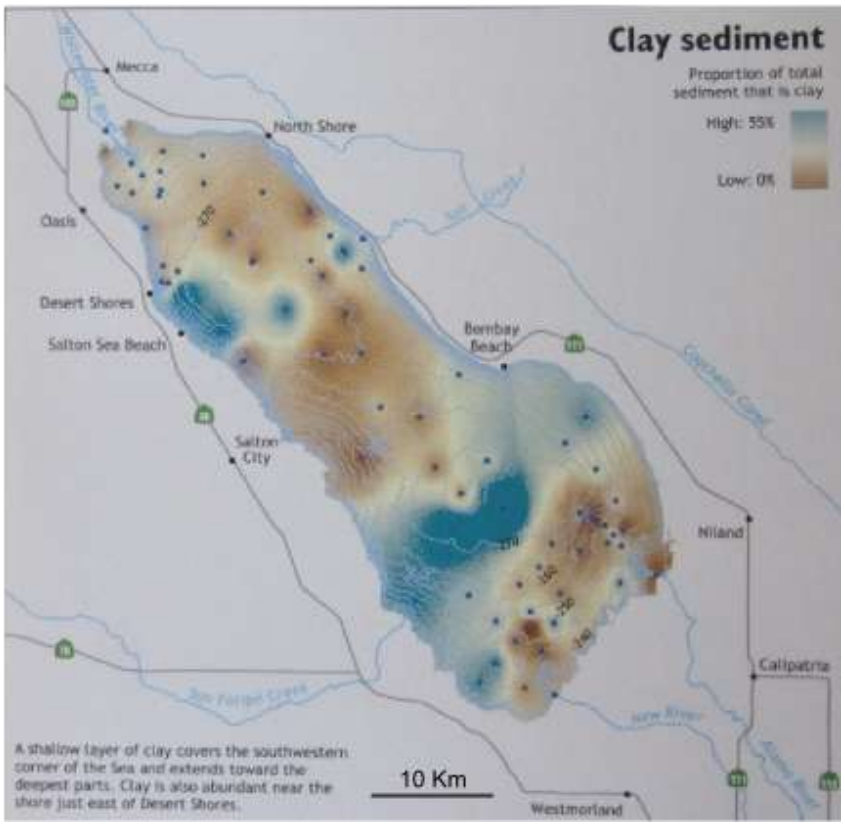
Clay sediment
Proportion of total sediment that is clay
High: 55%
Low: 0%
Mecca
North Shore
Oasis
Desert Shores
Salton Sea Beach
Bombay Beach
Salton City
Niland
Calipatria
Westmorland
A shallow layer of clay covers the southwestern corner of the Sea and extends toward the deepest parts. Clay is also abundant near the shore just east of Desert Shores.
10 Km

DISCUSSION

CONTINUATION OF THE CLARK FAULT BENEATH THE EXTRA FAULT ARRAY

Faults and folds expressed in the structural, geophysical and geomorphic relationships in the San Sebastian Marsh area are complex and may reflect the results of different geological processes. Several interpretations might describe the geometric relationship between the Clark fault and Extra fault array (Table 1). Our original hypotheses about the interactions between the two fault zones included truncation of the Clark fault zone by the Extra fault array, coeval activity on the Extra fault array and the Clark fault zone that produces a checkerboard pattern, offset of an inactive strand of the Clark fault by the Extra fault array, and/or that the Clark fault zone might be continuous in the subsurface as a blind fault (Table 1 and Fig. 6 F). Based on the data presented here, we discuss the most probable results: that the Clark fault continues southeast through and under the northeast-striking left-lateral faults of the Extra and Elmore Ranch fault arrays.

No single process can account for the active and distributed deformation in the field area and we here focus on the more important processes. The Clark fault zone is expressed in the San Sebastian field area by: 1) rotating the interfering left-lateral fault arrays, 2) localizing dextral strain at depth below subhorizontal decollement zones in the basin fill, 3) localizing sinistral strain in the shallower crust above the decollement zones, and 4) distributing dextral deformation onto small, short dextral faults above the decollement zones (Figs. 25, 27, 31, 37, 38 and Table 1). We here refer to high strain surfaces with subhorizontal dips as decollement zones in order to reserve the descriptor

Figure 37: Simplified schematic of dextral block rotation. A) A simplified 3D schematic of what bottom-driven block-rotation could look like before and after. This represents one hypothetical detachment horizon that, instead of propagating the fault upward, transfers motion to clockwise slip. Sediment above acts rigidly, forming sinistral faults between rotating blocks. B) A cross section of hypothetical dextral motion in the plutonic basement but enters detachment horizons in the younger basin fill sediment. C) A map view showing before and after slip and rotation. D) The hypothesized relationship applied to the Extra fault array showing actual but generalized strikes of the fault zones in the field area. Pre-rotated faults at about 20° and rotated orientation at about 60°.

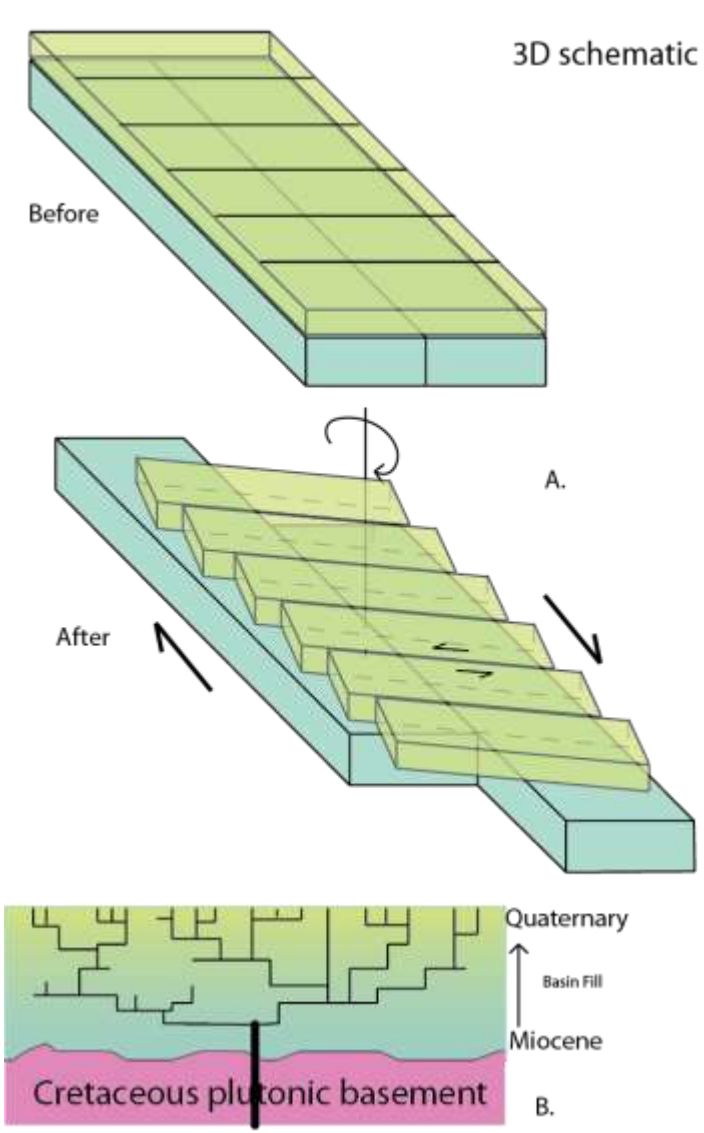
3D schematic
Before
A.
After
Quaternary
Basin Fill
Miocene
Cretaceous plutonic basement
B.

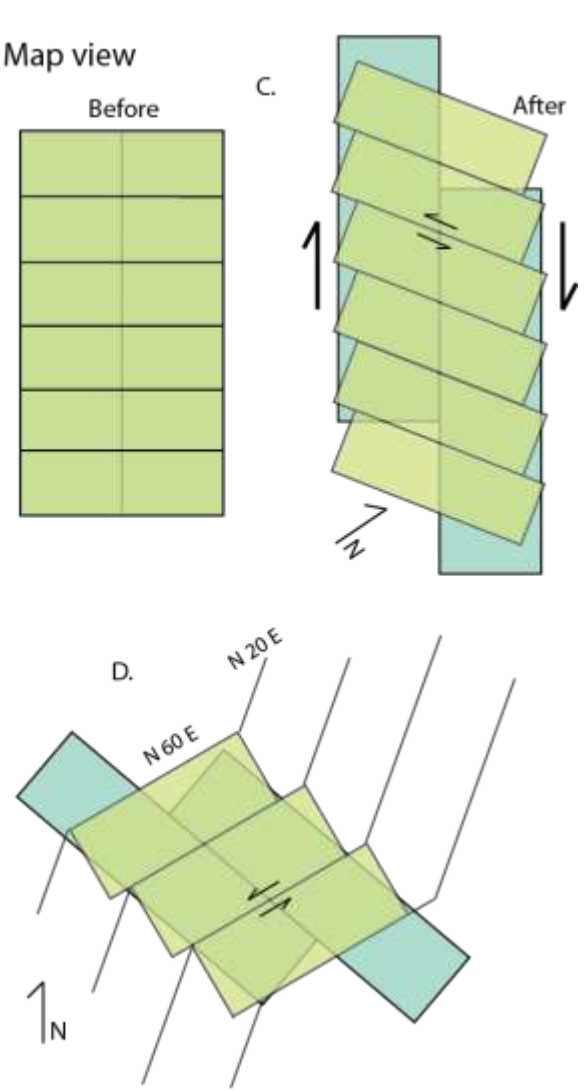
Map view
Before
C.
After
N
D.
N 20 E
N 60 E
N

Figure 38: Rotation calculations from Dickinson, 1996. A) A modified figure from Dickenson (1996) showing a simple model for rigid block rotation. B) A simplified geometry of the Extra fault zone showing a yellow line for its approximate orientation and a dashed line for the original strike of the Extra fault before block rotation occurred. C) A basic representation of a subsurface dextral shear and fault zone that drives rigid rotation and antithetic faults on the surface.

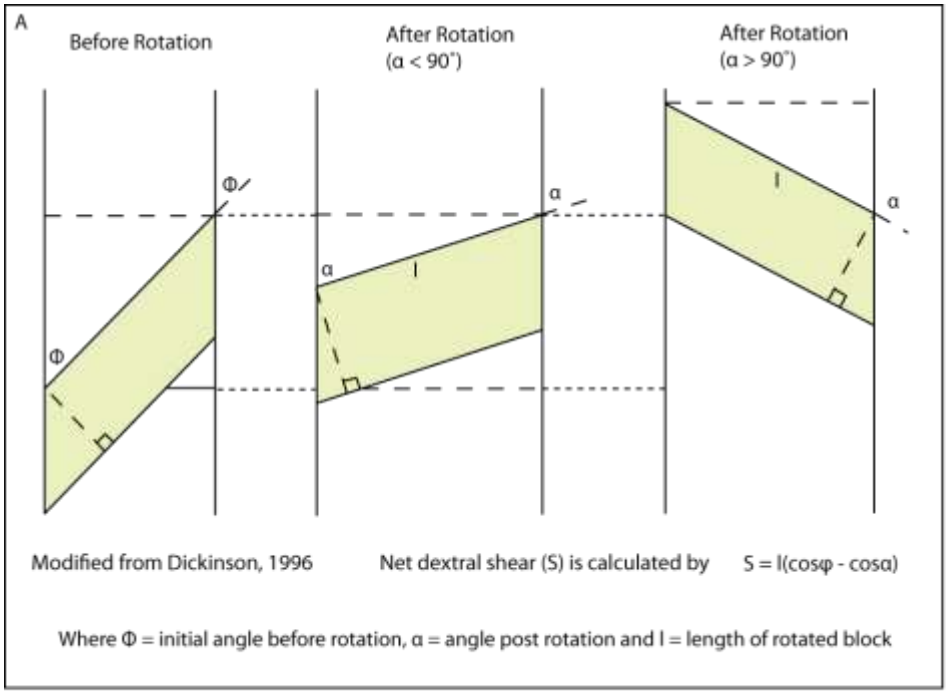

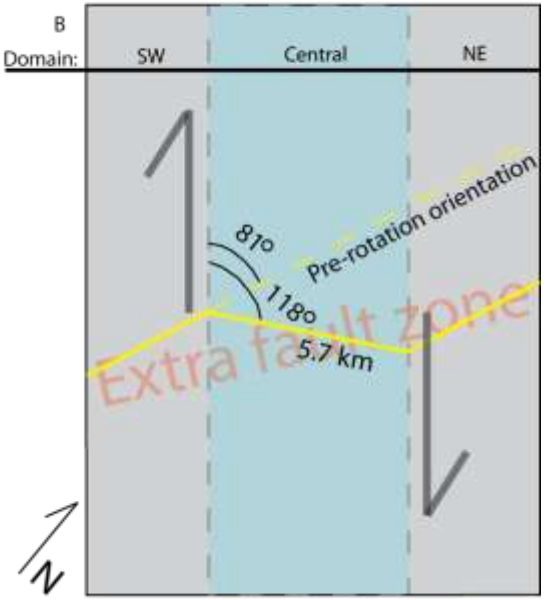

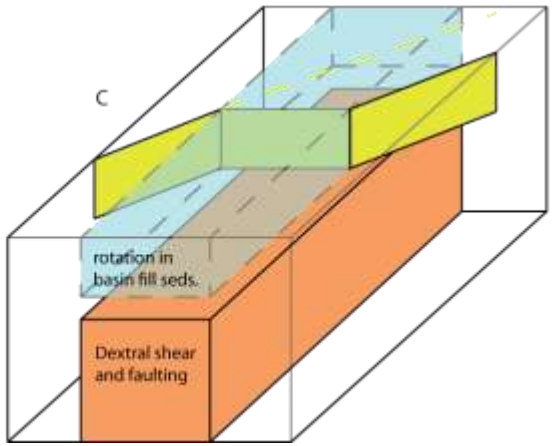

Measured from the Extra fault zone:
α = 118°
Φ = 81°
l = 5.7 km

Approximate dextral slip based on rotation of the Extra fault:
S = 5.7 (cos81-cos118) = 3.6 km

"detachment" for the low-angle right-normal West Salton detachment fault (Dibblee, 1954, 1984; Winker and Kidwell, 1996; Axen and Fletcher, 1998; Dorsey, 2006; Steely et al., 2006).

Evidence for a blind dextral fault zone between the San Felipe and Superstition Hills

Exhumed Miocene to Pleistocene basin-fill indicates active uplift

We interpret the Sebastian uplift, which has the Clark and Superstition Hills fault zones centered on it and along its southwest margin, as a structural high that results from dextral motion within the San Jacinto fault zone. The origin of the vertical component of deformation is not clear and probably results from both transpression between left-stepping dextral faults (Kirby et al., 2007) and a small normal component of deformation across some of the master dextral faults. Focal mechanisms of Yang et al. (2012) (Fig. 14) show that the small dip-slip components of strain tend to be extensional rather than contractional (Fig. 14).

The Sebastian uplift could be due to inflation by magma at depth. The Salton Sea area is an active geothermal field with several scattered Quaternary rhyolite domes (Robinson et al., 1976). Perhaps the uplift is a result of upward magma migration or expansion of a magma chamber at depth centered below the Sebastian uplift. If this is the case, the location and movement of the magma at depth must be tied to deep northwest-striking faults of the San Jacinto fault zone due to spatial relationships between the fault zone and the Sebastian uplift. Although magmatism could cause the uplift, the primary geothermal area of the Salton Sea is east of the field area and none are documented near the center of the uplift.

The strong spatial association of the Sebastian uplift with the Clark and Superstition Hills fault zones suggests the presence of a continuous fault through the field area. The Sebastian uplift is continuously parallel with the major faults associated with each section of the uplift, indicating a genetic relationship. The primary faults are always located along the southwest edge of the Sebastian uplift and it is along the southwest edge of the field area where InSAR anomalies, sharp Holocene/Pleistocene contacts, and microseismic lineaments occur (see above). Based on these correlations between uplift and faults, the San Sebastian Marsh section of the uplift is probably also associated with a fault along the southwest edge.

The size discrepancy between deltas formed by washes along the southwestern margin of the Salton Sea (described above, Fig. 35) may be explained by the delta of San Felipe Creek being anomalously small or the delta of Tule and Arroyo Salada delta being anomalously large. One hypothesis to explain the size discrepancy could be that erosion rates are fairly high in the drainage basin of Tule and Arroyo Salads washes, ultimately producing a large delta that matches the slower input of less sediment of San Felipe Creek (Fig. 36). This hypothesis seems unlikely because if the San Felipe Hills were shedding sediment fast enough to create an anomalously large delta, the topography would probably be lower than it is. Janecke et al. (2008) confirm that erosion rates are slow in the San Felipe Hills by reporting pediments that date roughly 22-62 ka and are only a few tens of meters above the active washes (OSL age determinations from Janecke et al., 2010). Slow erosion rates indicate that the delta is not receiving enough sediment to produce an anomalously large delta there. Inspection of the sizes of other deltas and

drainage basins in the Salton Trough suggests that the delta of San Felipe Wash is unusually small for the size of its drainage basin. Thus, any coarse material carried by San Felipe Creek must be deposited west of the Sebastian uplift while primarily suspended particles are carried into the delta and then the Salton Sea. If uplift is occurring rapidly enough in the Sebastian uplift to trap coarse sediment upstream, then some explanation is required for the somewhat lower elevation of the San Sebastian Marsh area relative to the San Felipe Hill and Superstition Hills. San Felipe Wash in the Marsh area probably localized along the structural saddle between the San Felipe Hills in the north and the Superstition Hills in the south. San Felipe Wash is also centered between the slight structural low between the Extra and Kane Springs fault zones (Fig. 2).

Northwest-striking dextral faults beneath northeast-striking sinistral faults

The Sebastian uplift provides evidence that the Clark fault is continuous beneath the Extra fault array in the subsurface to the Superstition Hills (Fig. 6 F). The continuity of the Clark fault in the subsurface requires a subhorizontal decollement interface between the sinistral faults in the shallow crust that are continuous across the hypothesized location of the Clark fault zone and the hypothesized dextral faults below. The interaction between the deep Clark fault zone and the shallower sinistral faults might localize along decollement horizons in mud-rich sedimentary intervals like those documented throughout this part of the Salton basin (Belgarde, 2007; Belgarde and Janecke, 2007; and this study) (Fig. 36 B). These decollement horizons may allow for strain to transfer between different crustal levels, between different families of structures, and between seemingly disconnected fault zones (Fig. 37 A and B). Since the Clark fault

is not cut by the northeast-striking left-lateral faults in the field area, this mechanism allows dextral strain to be transferred between the San Felipe Hills and the Superstition Hills and as well as from deeper to shallower levels of the crust.

Slip on the northeast-striking sinistral faults, fold formation and uplift could all be ultimately caused by subsurface dextral slip by transfer through the decollement surfaces (Fig. 37). This idea depends on the rheology of the basin-fill sediment. If the decollement surfaces in the basin-fill are transferring strain to structures and faults with different orientations, the northeast-striking faults evident on the surface do not represent the geometries of the faults in the subsurface (Fig. 37). However the northeast-striking left-lateral faults of the Extra fault array are in an orientation conjugate to the dextral faults that could produce seismic slip on their own within the shallow basin-fill sediments (Townend and Zoback, 2004) as seen on the Elmore Ranch fault (Hudnut et al., 1989a; Sharp et al., 1989).

Perhaps one particularly weak horizon acts as a main decollement horizon for the entire region. If this is the case, the decollement level must be above the basement-cover contact because exposures of the basement-cover contact at Borrego Mountain, Vallecito Mountains, and Coyote Mountains consistently show an irregular nonconformity (Steely, 2007; Kairouz, 2005; Dibblee, 1984 a and b). These locations were all uplifted from beneath the Salton basin (Janecke et al., 2010). We suggest that it would be more mechanically likely if the decollement horizons are within the basin-fill.

The northwest-trending alignment of microseismicity may support the need for a strain transference mechanism between the possible northwest-striking fault at depth and

the faults at the surface (Sharp, 1967; Peterson et al., 1991; Shearer et al., 2005; Lin et al., 2007; Yang et al., 2012). Perhaps rheological rock properties determine the fault expressions. High coefficients of friction within the plutonic rock might allow for high stress to accumulate until released in a larger event, more easily creating a continuous break. The new plane of weakness is a likely place for earthquakes to happen again, encouraging fault growth laterally and vertically. The energy from earthquakes in the study area propagates upward until the contact with basin-fill sediments (Fig. 37 A and B). The much younger basin-fill has much lower rock strength than the underlying basement, failing much more easily in response to any stress in any orientation. Exceptionally weak mud-rich horizons in the stratigraphy could allow for decollement surfaces to develop (Fig. 37 B).

Dextral slip-driven block rotation

The observed lateral strike change along all the fault zones of the Extra and Elmore Ranch fault arrays might be due to dextral rotation of underlying fault blocks (Fig. 25). Although there is not any paleomagnetic data from the central domain where highest magnitude would be expected, there is paleomagnetic data in the transitional domain (Fig. 25) that shows some small amount of clockwise rotation (Housen et al., 2004).

Vertical-axis rotation has been hypothesized between the Coyote Creek fault and Brawley seismic zone and a few studies have documented it paleomagnetically in this region (Nicholson et al., 1986; Housen et al., 2004; Johnson et al., 1983; Housen and Dorsey, 2012). Critical tests to confirm block rotation include paleomagnetism

orientations and the presence of a driving mechanism. The driving mechanism could be a continuous Clark fault zone within the field area as either bounding dextral faults at the edges of the shear zone or dextral motion from below (Dickinson, 1996). Unless a dextral fault on the southwest edge of the Sebastian uplift is covered by Holocene sediment, no dextral faults with enough offset along the edges are evident in the field (Plate 1). If dextral rotation is driving the change in strike, the motion must – at least in part – be driven by motion from below the Sebastian uplift; either as fault slip or as ductile motion beneath the seismogenic zone (Fig. 33 B).

Nicholson and others (1986) discuss the need for decollement surfaces to transfer strain from dextral faults to rotation. In the San Sebastian study area, rotation is likely being transferred through various levels of the previously discussed decollement surfaces, potentially losing large amounts of rotational strain in shearing (Fig. 37). If so, the amount of rotation evident on the surface in the faults is a minimum and does not record the total dextral strain at depth (Fig. 38). Another factor of the minimum constraint is when the northeast-striking left-lateral faults formed. If the faults of the Extra fault array formed before any rotation occurred, then they record all rotation that has not been lost in the decollement horizons. If rotation was occurring before they were emplaced, then the rotation recorded is another minimum constraint.

The northeast-striking faults of the sinistral Extra fault array may have formed in conjunction with rotation, accommodating secondary sinistral strain associated with the motion. The Extra fault array fault zones could represent bounding faults of rotating rigid blocks (Fig. 38). Block boundaries in clockwise rotation would produce sinistral

slip, which is what the Extra fault array seems to exhibit (Fig. 38). The fairly regular interval of sinistral faults may suggest similar width of blocks within the rotating central domain (Fig. 23).

Dickinson (1996) presents equations for various cases of dextral-driven block rotation based on geometric variables of rotated panels. We use a preferred "pinned" model for calculations of the Extra fault array because it allows for widths of the shear zone and rotating blocks to vary during deformation (Dickinson, 1996). The total amount of dextral shear (S) is calculated by multiplying the length (l) of the rotated panels by the difference between the cosine of the initial and rotated angles of the panel to the shear zone:

$$S = l(\cos\phi - \cos\alpha)$$

(Fig. 38). We use the Extra fault zone for the geometric measurements because it is the best exposed of the faults in the Extra fault array (Fig. 7). The length of the "rotated section" of the Extra fault zone is estimated at 5.7 km (Fig. 38). The average strike used to represent the Clark fault shear zone is N 53° W and the strike of the Extra fault zone in the northeast region is N 28° E making for an estimated initial angle of 81° between the Extra and Clark fault zones. The post-rotational angle of the Extra fault zone to the Clark fault is estimated to be 118°, a 37° change from the initial 81° (Fig. 38). Using the equation provided by Dickinson (1996) results in a required net dextral shear value of 3.6 km in the subsurface. This value is a first-order estimate and more detailed analysis could be performed to acquire more refined estimate of dextral strain.

Paleomagnetic data from Oil Well Wash and the Borrego Badlands

Paleomagnetic data are crucial to determining the likelihood and amount of rotation in the field area, particularly in the central domain of figure 39 where our structural model predicts up to 40° of clockwise rotation. Paleomagnetically determined vertical axis rotations are only available within the transitional domain in the southern San Felipe Hills along Oil Well Wash (Housen et al., 2004) (Fig. 2), where the structural data predict small clockwise rotation.

Paleomagnetic poles of samples from spatially distributed sites predict a lateral change in declination along the sites if rotation is occurring (Housen et al., 2004). Paleomagnetic data from 31 sites in Oil Well Wash were collected for the dual purpose of determining the Brawley and Ocotillo Formations magnetostratigraphy and vertical-axis rotation since deposition (Housen et al., 2004). Sample spacing was 10-30 meters and all the samples were collected within the section of the wash in the San Felipe Hills (Fig. 2).

Rotations calculated from these data indicate clockwise rotation of 8.5° ± 5.7° since about 1.0 Ma and are based on 6 sites with the most reliable data (Housen et al., 2004). Similar rotation patterns are evident in the southeast continuation of the Powerline fault zone (Fig. 28). The strike change of the Powerline fault zone at the intersection with the Bondit fault is consistent with counter-clockwise rotation (Fig. 28). The difference of 20° is not as significant as the strike change in the left-lateral faults but still suggests possible sinistral-driven rotation (Fig. 28). For the Powerline fault zone, the rotation is probably side-driven by motion of the shallow Extra fault array, also explaining the discontinuity of the northwest-striking right-lateral faults that are dissected by the northeast-striking fault (Fig. 28).

This clockwise rotation is what our model predicts in the transitional domain, where the paleomagnetic data were collected (Fig. 25). To fully test our structural model, however, paleomagnetic data are needed farther west, from the central domain of figure 25, where our geometric model of the field area predicts 40° of clockwise rotation. Although this magnitude of rotation in 1-2 m.y. seems unusually high, there is a growing body of paleomagnetic data from the late Cenozoic sedimentary rocks nearby that document clockwise rotation up to 40° in Plio-Pleistocene sediment, as well as pronounced lateral changes in rotations (Housen and Dorsey, 2012). Our preferred interpretation of all the currently available data is that clockwise rotation has occurred in the Sebastian uplift due to slip along the Clark fault zone and the rotation may be as much as the 40° predicted by our structural analysis. High-resolution geodetic data might also be used to determine short-term rotation rates.

Northwest-striking dextral fault zones may step en echelon to the Imperial fault

The Clark fault may be transferring strain to the Imperial fault via en echelon faults of short fault zones that step progressively left and southeast. The Superstition Hills and Superstition Mountains faults, in contrast, connect to the middle of the Imperial fault southeast of the field area (Figs. 1 and 27; Magistrale, 2002; Shearer et al., 2005; Lin et al., 2007). The short northwest-striking fault zones occur in a fairly regular interval, resembling some en echelon fault zones (Sharp, 1967). Understanding the geometric relationship of these northwest-striking fault zones with the northeast-striking left-lateral faults in the area is critical in determining if the northwest-striking fault zones are en echelon. If the northwest-striking fault zones are active en echelon faults related to

the Clark fault then they would form independent of the northeast-striking left-lateral faults. But the truncation of the northwest-striking dextral fault zones by the northeast-striking faults of the sinistral Extra and Elmore Ranch fault arrays resembles a relationship of cross-faults with master faults more than independent en echelon faults. The actual relationship could be a combination of en echelon steps and cross faulting. The location of the small fault zones may be controlled areas where en echelon fault strands develop but they are longer with more offset due to the addition of secondary strain associated with motion on the left-lateral northeast-striking faults (Fig. 27).

Instead of being en echelon strands, perhaps the northwest-striking right-lateral fault zones used to be linked in a continuous dextral fault in the Clark fault zone that has been dissected by younger, northeast-striking faults (Fig. 6 G). The observation that most of the faults are truncated by northeast-striking fault zones does support the idea. A critical test of this is scenario is to connect each tip of the northwest-fault zones to reconstruct motion on the northeast-striking left-lateral fault zones and see if the fault zones resemble each other sufficiently to have once been a continuous fault zone. Our data show instead that each northwest-striking dextral fault zone has a different expression and number of strands. The tips of the fault zones would not line up with the other tips upon reconstruction suggesting that the fault zones were not produced as a continuous strand. The reconstruction of motion along the northeast-striking fault zones would also produce a minimum estimate of slip on the northeast-striking left-lateral fault array. The amount of offset on each northeast-striking fault would need to be nearly identical at about 2 km which seems like too much and too consistent for the Extra fault

array (Fig. 27). The preferred explanation is a combination of the scenarios discussed above. The fault zones probably had an original tectonic origin but are now a plane of weakness for secondary strain from the northeast-striking faults and are now simply amplified cross faults (Fig. 27).

The San Sebastian Marsh area is a region of dextral fault growth

The southern Clark fault zone is a young fault that initiated slip around 1.1-1.3 Ma (Janecke et al., 2010). Structural expressions of the Clark fault in areas of its southward propagation might represent growth of the fault. The Tarantula Wash segment might represent a wide damage zone that simplifies downward into a more continuous, single trace. As the fault develops the more continuous subsurface trace will grow upward until it reaches the surface as a continuation of a clear Clark fault break and other smaller structures currently associated with the fault zone will be part of the faults damage zone. The section of the Extra fault array in the field area may represent an area of younger dextral fault development and growth. Over time we predict that the field area will develop more dextral faults and resemble more closely the structural expression currently observed within the San Felipe Hills. The Powerline fault zone is one dextral fault zone in the area that will likely form a more continuous trace at the surface as the Clark fault extends southward (Fig. 15). Geophysical analyses could determine if the Powerline fault zone is more continuous at depth or if the fault zone is actually a concentration of small discontinuous cross faults (Table 1). If the Powerline fault zone is continuous at depth then over time the Clark fault could develop a continuous surface trace that will truncate the faults of the Extra fault array.

The Superstition Hills fault might also be growing northward through the Elmore Ranch fault array that is part of the faults damage zone. The Superstition Hills fault already truncates several strands of the Elmore Ranch fault zone, but this may not always have been the case. The Superstition Hills fault exhibits a more mature relationship with the Elmore Ranch fault array than the Clark fault does with the Extra fault array. Perhaps several hundred thousand years ago the Superstition Hills fault had a very similar geometric relationship with the Elmore Ranch fault array that the Clark fault now exhibits with the Extra fault array. Eventually we predict that the Clark fault will grow and truncate some of the faults of the Extra fault array, similar to how the Superstition Hills fault is now. Finally, the Superstition Hills fault will continue growing to the northwest, cutting off remaining strands of northeast-striking left-lateral Kane Spring faults while the Clark fault similarly grows to the southwest, forming a continuous fault at the surface that bounds the entire Sebastian uplift along the southwest side.

DEXTRAL STRAIN DISPERSION INTO MULTIPLE STRUCTURES

The reason no large dextral fault has formed at the surface might be due to strain being dispersed into several structures, ultimately accommodating all the strain that would otherwise contribute to fault growth of a single dextral fault. Some of the structures that might accommodate portions of the strain include vertical axis rotation, en echelon slip, small cross fault formation, and strain transfer to northeast-striking sinistral faults.

If the strike changes presented above do represent vertical axis rotation of 37°, this could account for a very significant portion of overall dextral strain in the field area

(Fig. 38). Potential en echelon faults in the area might account for some strain that is ultimately being transferred to the Imperial fault (Fig. 27). All of the small dextral, northwest-striking faults in the field area might be accommodating very small amounts of strain individually, and collectively along with folds in the area might account for a portion of regional dextral strain. Strain transfer from dextral to sinistral faults might be the most significant factor of dextral strain dispersion.

The mutual interference of the Powerline fault with the Allegretti Farm fault likely involves strain transfer (Fig. 15). Both of these faults form prominent, continuous traces even very near their intersection and both are large enough that they could likely be continuous for several more kilometers. The abrupt termination of both faults at a location of such high strain may indicate that the strain is being transferred between the northeast and northwest striking faults. This is potentially plausible because the Allegretti and Powerline faults are at conjugate angles to the transtensional stress field. The dextral motion of the Clark fault would be transferring the strain to sinistral motion on the Allegretti Farm fault where they both become more diffuse within ~1 kilometer from the intersection (Fig. 15). The Allegretti Farm fault then transfers all of its strain to the Coyote Creek fault. This idea indicates that the Powerline strand of the Clark fault is ultimately transferring strain to the Coyote Creek fault via the sinistral Allegretti Farm fault (Fig. 4). Although this one example does not represent large amounts of strain transfer, this general relationship might account for most of the dextral strain dispersion into other structures in the field area.

IMPLICATIONS OF SEISMIC HAZARD

The field studies, mapping and discovery of displaced Holocene sediment show that every fault in the Extra fault array has been active during the Holocene. Evidence varies from fault scarps, offset streams, OSL and radiocarbon dating of sediment that overlies two to three clear colluvial wedges along the Extra fault zone, and faulted Holocene sediment in the other fault zones (Fig. 9, 10 and 11 and Table 2). Although most of the Extra fault array is not currently producing microseismicity, it still represents a seismic hazard. The microseismicity around the Extra fault array forms a noticeable shadow (or halo) zone that resembled the shadow zone around the 1968 rupture on the Borrego Mountain section of the Coyote Creek fault and the San Felipe Hills fault (Belgarde, 2007). A similar quiet period, characterized by a lack of microseismicity in the future rupture zone, preceded the M 7.2 2010 Baja California earthquake (also known as 2010 Easter earthquake, 2010 Sierra El Mayor earthquake, or 2010 El Mayor – Cucapah earthquake) (Hauksson et al., 2012) and the Elmore Ranch earthquake (Hudnut et al., 1989a; Sharp et al., 1989). Thus, the absence of microseismicity around the Extra fault array may be an early indicator of a future moderate-sized earthquake or earthquake swarm.

The Elmore Ranch fault array produced an M 6.2 earthquake in 1987 and strain at the surface spanned ~10 km from northwest to southeast on several fault strands (Hudnut et al., 1989a; Sharp et al., 1989). The width perpendicular to strike of the Extra fault array is similar to the width of faults that were active within the Elmore Ranch fault array in 1987 (Sharp et al., 1989). If these two fault arrays behave similarly, we predict that a large earthquake in the Extra fault array would produce surface faulting on short sections

of the Shoreline, Bondit and Sebastian, fault zones and most of the larger strands of the Extra fault zone when the Extra fault array fails. Slip on the Extra fault array could induce slip on other larger faults in the region, similar to the 1987 Elmore Ranch event that induced slip on master dextral faults in the area (Hudnut et al., 1989a; Sharp et al., 1989). The most likely secondary events would be a rupture of the Coyote Creek fault from the intersection of the Extra fault array to the southeast, and perhaps the San Andreas fault. Depending on the magnitude of strain release on these faults, other events could occur on the Superstition Mountain or Imperial faults.

Current interpretations (Hudnut et al., 1989a; Brothers et al., 2009, 2011) interpret the Extra fault array as terminating into the San Andreas fault. Work in progress (Janecke, unpublished mapping) suggests that this model is too simple and probably erroneous along the southern San Andreas fault. The Extra fault array may not persist to the main strand of the San Andreas fault in the northeast.

Any fault associated with the southern Clark fault zone that interacts with the Extra fault array may also be triggered. This depends on the actual geometric relationship a hypothesized Clark fault has with more shallow conjugate faults. Sinistral motion on the Extra fault array could increase or decrease effective pressure on the underlying Clark fault depending on relative asymmetry of fault slip and could increase or decrease the likelihood of inducing slip.

CONCLUSIONS

Field mapping, geophysical interpretation and processing and geomorphic relationships within the San Jacinto fault zone document complex and unexpected interactions between the Clark fault of the San Jacinto fault zone and the Extra-Elmore fault arrays. Mapping in the San Sebastian field area between the San Felipe and Superstition Hills at 1:24000 confirms previous geologic mapping that the Clark fault ends in the southern San Felipe Hills and is not well expressed within or southeast of the Extra fault zone (Dibblee, 1954, 1984; Reitz, 1977; Heitman, 2002; Lilly, 2003; Kirby et al., 2007; Janecke et al., 2010). The regional strain farther south is dominated by northeast-striking left-lateral faults on the surface. The Extra fault array may be continuous from as far southwest as the Coyote Creek fault and one strand(?) in the array may extend as far northeast as the San Andreas fault (Brothers et al., 2009, 2011), for a maximum distance of ~42 km. Holocene alluvial, eolian and lacustrine sediment obscured the last 6-8 km of its trace in Lower Borrego Valley. Complex interactions between the San Jacinto and Extra and Elmore Ranch fault zones suggest that the Extra and Elmore Ranch fault arrays are mutually interfering with the dextral faults in previously unimagined ways.

A first-order description of the Extra-Elmore sinistral fault array is presented. Several previously unknown left-lateral faults were mapped on either side of the master Extra fault zone. The faults are spaced fairly regularly and occur from northwest to southeast as the Shoreline, Bondit, Extra, Extra East, Sebastian, and Border Patrol fault zones in the Extra fault array. This fault array is about 7 km wide and 35 km long, and

bears a striking resemblance to the better known Elmore Ranch fault array. Like the Elmore Ranch fault array, the Extra fault array probably represents a single major left-lateral fault at depth yet is expressed by dispersed faulting and folding in the upper few kilometers of the crust. The dispersed "pitch fork" geometry of the deformation conceals the true magnitude of the Extra and Elmore Ranch fault zones.

Slickenlines reveal primary strike-slip motion across the northeast-striking faults and tool marks suggest left-slip. En echelon relationships in the Extra fault zone step right and form contractional domes which is consistent with left-slip across the faults. Vertical slip components are concentrated near step-over zones.

There is widespread evidence in fault scarps, displaced Holocene sediment and morphometric data for Holocene activity on the Extra fault array. The most abundant evidence is along the central, transitional and northeastern domain of the Extra fault zone (Fig. 16). Optically Stimulated Luminescence and radiocarbon dates of a lacustrine bed that immediately postdate the last earthquake are 0.7 +/- 0.29 ka old and 975 +/- 15 years b.p., respectively, along Bondit Wash (Table 2 of OSL results). Two or three Holocene colluvial wedges formed during moderate to large earthquakes in this part of the Extra fault prior to the ~1 ka capping sediment. The southwest end of the fault zone appears less active and is mostly buried by Holocene deposits.

In spite of widespread indicators of Holocene slip on the Extra fault array, very little seismicity has occurred nearby since 1981. The San Jacinto fault zone is known for the large number of small earthquakes produced by its many fault strands (Petersen et al., 1991; Hauksson et al., 2012; Yang et al., 2012). There is a marked lack of

microseismicity, however, spatially associated with the Extra fault array, except in its southern extent. Occasional isolated earthquakes are known but the only lineaments form in a northwest trend at high angles to the Extra fault array. Previous to the historic rupture of 1987, the Elmore Ranch fault was also very quiet. The Extra fault array and the Clark fault below may be locked, much like the Elmore Ranch and Superstition Hills faults were before the 1987 earthquakes.

If the Extra fault branches from the Coyote Creek fault in the southwest, as we provisionally interpret, then a moderate earthquake on the Extra fault array could trigger a larger southward-rupturing earthquake on the Coyote Creek fault. This earthquake would rupture toward Superstition Mountain. Other researchers have suggested that the southern San Andreas fault could fail when a moderate earthquake ruptures the Extra fault zone, because such an earthquake would extensionally unclamp the San Andreas fault near Bombay Beach (Hudnut et al., 1989a; Brothers et al., 2009, 2011). The strong evidence for contraction near the San Andreas fault in Durmid Hill (Babcock, 1974;; Bürgmann, 1991) casts serious doubt on this interpretation (Janecke and Markowski, work in progress).

The Salton trough has been accommodating the deposition of sediment from the Colorado River since the latest Miocene and is the current depocenter for the eastern Peninsular Ranges and Colorado River (Dibblee, 1984a and b; Winker and Kidwell, 1996; Dorsey et al., 2007). Holocene basin-fill deposits cover most of the older sediment in the Salton Trough, except in narrow uplifts along the San Andreas fault zone and within much wider uplifts along the San Jacinto and Elsinore fault zones (Janecke et al.,

2010). One anomalous area of exhuming sediment is the northwest trending Sebastian uplift, which has active dextral oblique slip faults of the San Jacinto fault zone localized along its spine and western margin. The biggest named faults embedded within the uplift are the Clark, Superstition Hills and Superstition Mountains faults.

The narrow central part of the Sebastian uplift is in the field area around the San Sebastian Marsh. There the Sebastian uplift exposes nothing older than Pleistocene sedimentary rock of the Brawley and Ocotillo formations, and surface structures are dominated by northeast-striking left-lateral faults of the Extra and the northwestern part of the Elmore Ranch fault arrays. Individual faults in these arrays strike between N50-70E° across the crest of the Sebastian uplift, whereas northeast and southwest of the uplift, the along strike-continuations of the faults strike between N0-30°E. This geometry suggests that the left-lateral faults were probably rotated clockwise about a vertical axis in the vicinity of the Clark fault zone. This rotated domain coincides roughly with the crest of the Sebastian uplift.

We interpret that the Clark fault is acting as a "blind fault" between the San Felipe Hills and the Superstition Hills fault to the south. Dextral motion on a subvertical fault in the subsurface is being transferred upward through low-angle decollement horizons in the weak mudstone horizons to rotation of steep sinistral-slip faults in shallower parts of the crust according to this preferred interpretation. Published InSAR interferograms of this region reveal much more tectonic deformation along northwest-striking boundaries than along northeast-striking ones (Fig. 32; Lyons and Sandwell, 2003; Mellors and Boisvert, 2003; Van Zandt et al., 2004; Lundgren et al., 2009; Wei et

al., 2009; Tong et al., 2011). The only well-developed northeast–striking deformational boundary has a nontectonic origin, and results from pumping groundwater withdrawal from a faulted aquifer (Wei et al., 2009).

Relocated hypocenters show two northwest-striking fault planes in the subsurface between the Clark and Superstition Hills faults at depth of 5 and 6 km. The fault planes defined by this microseismicity have the same strike as the San Felipe Hills and Powerline strands of the Clark fault but lie midway (~2.5 km laterally) between the projected traces of those two dextral faults (Fig. 33; Hauksson et al., 2012; Yang et al., 2012). Surface faults in the vicinity of the two dextral microseismic alignments show no spatial relationship with the earthquakes at 5 to 6 km. Instead there are continuous northeast-striking left-lateral faults that cross above the dextral faults (this study fig. 37). Focal data from some of the seismic events reveal a steep northwest-striking nodal plane with primary strike-slip deformation along with a component of normal slip (Yang et al., 2012).

The newly defined relationship between the blind Clark fault in the subsurface and shallower conjugate faults above resembles freeways in that there are overpasses and underpasses to accommodate otherwise interfering strain. We therefore refer to this as an "underpass and overpass model" of mutually interfering conjugate strike-slip faults. This type of relationship has not been recognized in other regions but may be fairly common in mud-rich sedimentary basins like the Los Angeles and Salton basins. More work is required to fully define the kinematic and mechanicals aspects of fault zones with this geometry and to characterize the seismic hazard posed by such cryptic faults.

REFERENCES

Atwater, T., 1970, Implications of plate tectonics for the Cenozoic tectonic evolution of western North America: Geological Society of America Bulletin, v. 81, p. 3513-3536.

Axen, G.J., and Fletcher, J.M., 1998, Late Miocene–Pleistocene extensional faulting, northern Gulf of California, Mexico and Salton Trough, California: International Geology Review, v. 40, p. 217–244.

Babcock, A.E., 1974, Geology of the northeast margin of the Salton Trough, Salton Sea, California: Geological Society of America Bulletin, v. 85, no. 3, p. 321-332.

Bartholomew, M.J., 1970, San Jacinto fault zone in the northern Imperial Valley, California: Geological Society of America Bulletin, v. 81, no. 10, p. 3161–3166.

Belgarde, B.E., 2007, Structural characterization of the three southeast segments of the Clark fault, Salton Trough, California [M.S thesis]: Logan, Utah State University, 4 plates, map scale 1:24,000, 216 p.

Belgarde, B.E., and Janecke, S.U., 2006, Structural characterization and microseismicity near the southeast end of the Clark fault of the San Jacinto fault zone in the southwest Salton Trough: Palm Springs, California, Annual Meeting of the Southern California Earthquake Center, v. 16, p. 75.

Belgarde, B.E., and Janecke, S.U., 2007, A “hidden” fault? Structural geology of three segments of the Clark fault, San Jacinto fault zone, California: Geological Society of America Abstracts with Programs, v. 39, p. 375, http://gsa.confex.com/gsa/2007AM/fi nalprogram/abstract_129101.htm.

Biehler, S., and Rothstein, D., compilers, 1979, Salton Sea sheet of Bouguer gravity map of California, Sacramento: California Division of Mines and Geology, scale 1:250,000.

Bjornstad, S.C., Hall B., Unruh J., and Richards-Dinger K., 2006, Geothermal Resource Exploration: Naval Air Facility El Centro – Superstition Mountain Area, Imperial Valley, California, GRC 2006.

Brothers, D.S., Driscoll, N.W., Kent, G.M., Harding, A.J., Babcock, J.M., and Baskin, R.L., 2009, Tectonic evolution of the Salton Sea inferred from seismic reflection data: Nature Geoscience, v. 2, p. 581-584.

Brothers, D.S., Kilb, D., Luttrell, K., Driscoll, N., and Kent, G., 2011, Loading of the San Andreas fault by flood-induced rupture of faults beneath the Salton Sea: Nature Geoscience, v. 4, p. 486-492.

Burbank, D.W., and Anderson, R.S., 2001, Tectonic Geomorphology: Blackwell, Malden, MA, 274 p.

Bürgmann, R., 1991, Transpression along the Southern San Andreas Fault, Durmid Hill, California: Tectonics, v. 10, no. 6, p. 1152-1163.

Clark, M.M., 1972, Surface rupture along the Coyote Creek fault, in The Borrego Mountain earthquake of April 9, 1968: United States Geological Survey Professional Paper, 787, p. 55-86.

Dickinson, W.R., 1996, Kinematics of Transrotational Tectonism in the California Transverse Ranges and Its Contribution to Cumulative Slip Along the San

Andreas Transform Fault System: Geological Society of America Special Paper, 305, p. 1-46.

Dibblee, T.W., Jr., 1954, Geology of the Imperial Valley region, California, Geology of southern California: California Division of Mines Bulletin, v. 170, p. 21–28.

Dibblee, T.W., Jr., 1984a, Stratigraphy and tectonics of the San Felipe Hills, Borrego Badlands, Superstition Hills, and vicinity, *in* Rigsby, C.A., ed., The Imperial Basin—Tectonics, Sedimentation, and Thermal Aspects: Los Angeles, California, Pacific Section, Society of Economic Paleontologists and Mineralogists, p. 31–44.

Dibblee, T.W., 1984b, Stratigraphy and tectonics of the Vallecito-Fish Creek mountains, Vallecito badlands, Coyote mountains, Yuha desert, southwestern Imperial basin, *in* Rigsby, C.A. ed., The Imperial Basin—Tectonics, Sedimentation, and Thermal Aspects: Los Angeles, California, Pacific Section, Society of Economic Paleontologists and Mineralogists, p. 59-79.

Dibblee, T.W., Jr., 1996, Stratigraphy and tectonics of the Fish Creek-Vallecito Mountains, Vallecito Badlands, Coyote Mountains, and Yuha Desert, southwestern Imperial basin, California, *in* Abbott, P.L., and Seymore, D.C., eds., Sturzstroms and Detachment Faults, Anza-Borrego Desert State Park, California: Santa Ana, California, South Coast Geological Society, Annual Field Trip Guidebook, v. 24, p. 59-79.

Dibblee, T.W., Jr., and Minch, J.A., 2008, Geologic map of the Neenach & Willow Springs 15 minute quadrangles, Kern & Los Angeles Counties, California: Dibblee Geological Foundation Map DF-383, scale 1:62500.

Dorsey, R.J., 2006, Stratigraphy, tectonics, and basin evolution in the Anza-Borrego Desert region, *in* Jefferson, G.T., and Lindsay, L.E., eds., Fossil Treasures of Anza-Borrego Desert: San Diego, California, Sunbelt Publications, p. 89–104.

Dorsey, R.J., Fluette, A., McDougall, K.A., Housen, B.A., Janecke, S.U., Axen, G.A., and Shirvell, C.R., 2007, Chronology of Miocene–Pliocene deposits at Split Mountain Gorge, southern California: A record of regional tectonics and Colorado River evolution: Geology, v. 35, p. 57-60.

Dorsey, R.J., Housen, B.A., Janecke, S.U., Fanning, M., and Spears, A.L.F., 2011, Stratigraphic record of basin development within the San Andreas fault system: Late Cenozoic Fish Creek–Vallecito basin, southern California: Geological Society of America Bulletin, v. 123, p. 771-793.

Dorsey, R.J., Axen, G.J., Peryam, T.C., and Kairouz, M.E., 2012, Initiation of the Southern Elsinore Fault at ~ 1.2 Ma: Evidence from the Fish Creek–Vallecito Basin, southern California: Tectonics, v. 31, no. 2, p. TC2006.

Dronyk, M.P., 1977, Stratigraphy, structure and a seismic refraction survey of a portion of the San Felipe Hills Imperial Valley, California [M.S. Thesis]: Riverside, California University of California, 141 p.

Fialko, Y., Sandwell D., Simmons M., and Rosen, P., 2005, Three-dimensional deformation caused by the Bam, Iran, earthquake and the origin of shallow slip deficit: Nature, v. 435, p. 295-299.

Fialko, Y., 2006, Interseismic strain accumulation and the earthquake potential on the southern San Andreas fault system: Nature, v. 441, p. 968–971.

Forand, D.H., 2010, Examination of Deformation in Crystalline Rock from strike-slip faults in two locations, southern California [M.S. Thesis]: Logan, Utah State University, 208 p.

Fuis, G.S., and Kohler, W.M., 1984, Crustal structure and tectonics of the Imperial Valley region, California, *in* Rigsby, C.A., ed., The Imperial Basin-Tectonics, sedimentation and thermal aspects: Los Angeles, Pacific Section: Society of Economic Paleontologists and Mineralogists, p. 1-13.

Fuis, G.S., Mooney, W.D., Healy, J.H., Mcmechan, G.A., and Lutter, W.J., 1984, A seismic refraction survey of the Imperial-Valley Region, California: Journal of Geophysics Research, v. 89, p. 1165-1189.

Hardebeck, J.L., and Shearer, P.M., 2002, A new method for determining first-motion focal mechanisms: Bulletin of the Seismological Society of America, v. 92, p. 2264–2276, doi 10.1785/0120010200.

Hardebeck, J.L., and Shearer, P.M., 2003, Using S/P amplitude ratios to constrain the focal mechanisms of small earthquakes: Bulletin of the Seismological Society of America, v. 93, p. 2434–2444, doi 10.1785/0120020236.

Hauksson, E., Yang, W., and Shearer, P.M., 2012, Waveform Relocated Earthquake Catalog for Southern California (1981 to 2011): Bulletin Seismological Society of America v. 102, p. 2239-2244.

Heitman, E.A., 2002, Characteristics of the structural fabric developed at the termination of a major wrench fault [M.S. Thesis]: San Diego, California, San Diego State University, 77 p.

Helgeson, H.C., 1968, Geologic and thermodynamic characteristics of the Salton Sea geothermal system: American Journal of Science, v. 266, n. 3, p. 129-166.

Housen, B.A., and Dorsey, R.J., 2012, Magnetostratigraphy and paleomagnetism of the Plio-Pleistocene Arroyo Diablo and Borrego Formations in the Borrego Badlands, western Salton Trough, CA: American Geophysical Union, Fall Meeting 2010, abstract GP23C-08.

Housen, B.A., Dorsey, R.J., Janecke, S.U., Kirby, S.M., and Lutz, A.T., 2004, Magnetostratigraphy and Rotation of Pleistocene Sedimentary Rocks in the San Jacinto Fault zone, Western Salton Trough, California: American Geophysical Union, Fall Meeting 2004, abstract GP43A-0841.

Hudnut, K.W., Seeber, L., and Pacheco, J., 1989, Cross-fault triggering in the November 1987 Superstition Hills earthquake sequence, southern California: Geophysical Research Letters, v. 16, p. 199-202.

Hudnut, K.W., Seeber, L., Pacheco, J., Armbruster, J.G., Sykes, L.R., Bond, C.G., and Kominz, M.A., 1989, Cross faults and block rotation in Southern California; earthquake triggering and strain distribution: Yearbook Lamont –Doherty Geological Observatory of Columbia University, p. 44-49.

Hudnut, K.W., Beavan, J., and Bilham, R., 1984, Salton Sea level data; active transpression on the southern San Andreas Fault: American Geophysical Union, v. 66, p. 383.

Hutton, K., Woessner, J., and Hauksson, E., 2010, Earthquake monitoring in southern California for seventy-seven years (1932–2008): Bulletin of the Seismological Society of America, v. 100, p. 423–446, doi 10.1785/0120090130.

Janecke, S.U., and Belgarde, B.E., 2008, Detecting hidden, high-slip rate faults: S. San Jacinto fault zone: Final Report for NEHRP Grant 06HQGR0031, 96 p., http://earthquake.usgs.gov/research/external/research.php?yearID=2006&pi=janecke&regionID=&award=&keyword=&submit=Find+Projects.

Janecke, S.U., Dorsey, R.J., Forand, D., Steely, A.N., Kirby, S.M., Lutz, A.T., Housen, B.A., Belgarde, B., Langenheim, V.E., and Rittenour, T.M, 2010, High Geologic Slip Rates since Early Pleistocene Initiation of the San Jacinto and San Felipe Fault Zones in the San Andreas Fault System: Southern California, USA: Geological Society of America Special Paper 475, doi: 10.1130/2010.2475.

Janecke, S.U., and Thornock, S.J., 2011, Interactions between the Clark strand of the San Jacinto fault zone and the Extra-Elmore fault arrays: poster presented at Southern California Earthquake Center annual meeting.

Jennings, C.W., Strand, R.G., Rogers, T.R., Boylan, R., Moar, R.R. and Switzer, R.A., 1982, Geologic map of California: California Division of Mines and Geology

Johnson, C.E. and L.K. Hutton, 1982, Aftershocks and pre-earthquake seismicity, in The Imperial Valley earthquake of October 15, 1979: United States Geological Survey Professional Paper, v. 1254, p. 59-76.

Johnson, M., Officer, C.B., Opdyke, D., Woodard, G.D., Zeitler, P.K., and Lindsay, E.H., 1983, Rates of late Cenozoic tectonism in the Vallecito-Fish Creek basin, western

Imperial Valley, California: Geology, v. 11, p. 664–667, doi: 10.1130/0091-7613(1983)11<664:RO LCTI>2.0.CO;2.

Kairouz, M.E., 2005, Geology of the Whale Peak Region of the Vallecito Mountains: Emphasis on the kinematics and timing of the West Salton detachment fault, southern California [M.S. thesis]: Los Angeles, University of California, 156 p.

Kendrick, K.J., Morton, D.M., Wells, S.G., and Simpson, R.W., 2002, Spatial and temporal deformation along the northern San Jacinto fault, southern California: Implications for slip rates: Bulletin of the Seismological Society of America, v. 92, p. 2782–2802.

Kim, Y.S., Peacock, D.C.P., and Sanderson, D.J., 2004, Fault damage zones: Journal of Structural Geology, v. 26, p. 503–517.

Kirby, S.M., 2005, The Quaternary tectonic and structural evolution of the San Felipe Hills, California [M.S. thesis]: Logan, Utah State University, 182 p.

Kirby, S.M., Janecke, S.U., Dorsey, R.J., Housen, B.A., McDougall, K., Langenheim, V., and Steely, A., 2007, Pleistocene Brawley and Ocotillo Formations: Evidence for initial strike-slip deformation along the San Felipe and San Jacinto fault zones, California: Journal of Geology, v. 115, p. 43–62, doi: 10.1086/509248.

Klinger, R.E., and Rockwell, T.K., 1989, Flexural-slip folding along the eastern Elmore Ranch fault in the Superstition Hills earthquake sequence of November 1987: Bulletin of the Seismological Society of America, v. 79, p. 297-303.

Kohler, W.M., and Fuis, G.S., 1986, Travel-time, time-term, and basement depth maps for the Imperial Valley region, California, from explosions: Bulletin of the

Seismological Society of America, v. 76 no. 5, p. 1289-1303.

Langenheim, V.C., and Jachens, R.C., 1993, Isostatic residual gravity map of the Borrego Valley 1:100,000 scale quadrangle, California: United States Geological Survey, Open-File Report 93-2461, scale 1:100,000.

Langenheim, V.E., and Rittenour, T.M., 2011, High Geologic Slip Rates since Early Pleistocene Initiation of the San Jacinto and San Felipe Fault Zones in the San Andreas Fault System: Southern California, USA: Geological Society of America Special Paper 475, p. 48.

Lilly, D.R. 2003, Structural geology of a transitory left step in San Felipe Hills fault, [M.S. Thesis]: San Diego, California, San Diego State University, 91 p.

Lin, G., Shearer, P.M., and Hauksson, E., 2007, Applying a three-dimensional velocity model, waveform cross correlation, and cluster analysis to locate southern California seismicity from 1981 to 2005: Journal of Geophysical Research, v. 112, B12309, doi: 10.1029/2007JB004986.

Lundgren, P., Hetland, E.A., Liu, Z., and Fielding, E., 2009, Southern San Andreas-San Jacinto fault system slip rates estimated from earthquake cycle models constrained by GPS and interferometric synthetic aperture radar observations: Journal of Geophysical Research, vol. 114, no. b0, 2403.

Lutz, A.T., Dorsey, R.J., Housen, B.A., and Janecke, S.U., 2006, Stratigraphic record of Pleistocene faulting and basin evolution in the Borrego Badlands, San Jacinto fault zone, southern California: Geological Society of America Bulletin, v. 118, p. 1377–1397, doi: 10.1130/B25946.1.

Lyons, S., and Sandwell, D., 2003, Fault creep along the southern San Andreas from interferometric synthetic aperture radar, permanent scatterers, and stacking: Journal of Geophysical Research, v. 108, no. b1, 2047, doi:10.1029/2002jb001831.

Magistrale, H., 2002, Relative contributions of crustal temperature and composition to controlling the depth of earthquakes in Southern California: Geophysical Research Letters, v. 29, no. 10, p. 1447, doi:10.1029/2001GL014375.

Magistrale, H., Jones, L., and Kanamori, H., 1989, The Superstition Hills, California, earthquakes of 24 November 1987: Bulletin of the Seismological Society of America, v. 79, p. 239-251.

Matti, J.C., and Morton, D.M., 1993, Paleogeographic evolution of the San Andreas fault in southern California: A reconstruction based on a new cross-fault correlation, *in* Powell, R.E., Weldon, R J., and Matti, J.C., eds., The San Andreas Fault System: Displacement, Palinspastic Reconstruction, and Geologic Evolution: Geological Society of America Memoir 178, p. 107–159.

Mellors, R.J., and Boisvert, A., 2003, Deformation near the Coyote Creek fault, Imperial County, California: Tectonic or groundwater-related?: Geochemistry Geophysics Geosystems, v. 4(2), 1012, doi:10.1029/2001GC000254.

Mellors, R.J., Van Zandt, A., and Rojas, O., 2005, The temporal and spatial distribution of deformation in the western Salton trough from 1992-2001 as observed by InSAR: American Geophysical Union, Fall Meeting 2005, abstract G43A-06

Morley, E.R., 1963, Geology of the Borrego Mountain quadrangle and the western portion of the Shell Reef quadrangle, San Diego County, California: [Ph.D. dissertation]: Los Angeles, University of Southern California., 1963 p.

Muffler, L.P.J., and White, D.E., 1969, Active metamorphism of Upper Cenozoic sediments in the Salton Sea geothermal field and the Salton Trough, southeastern California: Geological Society of America Bulletin, v. 80, p. 157-182.

Nicholson, C., Seeber, L., Williams, P., and Sykes, L.R., 1986, Seismic evidence for conjugate slip and block rotation within the San Andreas Fault System, southern California: Tectonics, v. 5, p. 629–648, doi:10.1029/TC005i004p00629.

Petersen, M.D., Seeber, L., Sykes, L.R., Nábělek, L.J., Armbruster, J.G., Pacheco, J., and Hudnut, K.W., 1991, Seismicity and fault interaction, Southern San Jacinto Fault Zone and adjacent faults, southern California: Implications for seismic hazard: Tectonics, v. 10(6), p. 1187–1203, doi:10.1029/91TC01240.

Reitz, D.T., 1977, Geology of the western and central San Felipe Hills, northwestern Imperial County, California, [M.S. Thesis]: Los Angeles, University of Southern California, 155 p.

Robinson, P.T., Elders, W.A., and Muffler, L.J.P., 1976, Quaternary volcanism in the Salton Sea geothermal field, Imperial Valley, California: Geological Society of America Bulletin, v. 87, no. 3, p. 347-360.

Rogers, T.H., 1965, Geologic map of California: Santa Ana sheet: California Division of Mines and Geology, scale 1:250000.

Rosen, P., Werner, C., Fielding, E., Hensley, S., Buckley, S., and Vincent, P., 2000,

Aseismic creep along the San Andreas Fault northwest of Parkfield, California, measured by radar interferometry: Geophysical Research Letters, v. 25, no. 6, p. 825–828.

Sanders, C.H., Magistrale, H., and Kanamori, H., 1986, Rupture patterns and preshocks of large earthquakes in the southern San Jacinto fault zone: Bulletin of the Seismological Society of America, v. 76, p. 1187–1206.

Sanders, C.O., 1989, Fault segmentation and earthquake occurrence in the strike-slip San Jacinto fault zone, California, *in* Schwartz, D.P., and Sibson, R.H., eds., Proceedings of Conference XLV: A Workshop on Fault Segmentation and Controls of Rupture Initiation and Termination: United States Geological Survey Open-File Report, v. 89-0315, p. 324–349.

Severson, L.K., 1987, Interpretation of shallow crustal structure of the Imperial Valley, California, from seismic reflection profiles [M.S. Thesis]: Berkeley, California, Lawrence Berkeley Lab, 90 p.

Sharp, R.V., 1967, San Jacinto fault zone in the Peninsular Ranges of southern California: Geological Society of America Bulletin, v. 78, p. 705–729, doi: 10.1130/0016-7606(1967)78[705:SJFZIT]2.0.CO;2.

Sharp, R.V., 1972, Tectonic setting of the Salton Trough, in the Borrego Mountain earthquake of April 9, 1968: United States Geological Survey Professional Paper, 787, p. 3–15.

Sharp, R.V., and Clark, M.M., 1972, Geologic evidence of previous faulting near the1968 rupture on the Coyote Creek fault: United States Geological Survey Professional

Paper, 1254, p. 5-14.

Sharp, R.V., 1975, En echelon fault patterns of the San Jacinto fault zone: California Division of Mines Geology, Special Report 118, p. 147-152.

Sharp, R.V., Budding, K.E., Boatwright, J., Ader, M.J., Bonilla, M.G., Clark, M.M., Fumal, T.E., Harms, K.K., Lienkaemper, J.J., Morton, D.M., O'Neill, B.J., Ostergren, C.L., Ponti, D.J., Rymer, M.J., Saxton, J.L., and Sims, D.J., 1989, Surface faulting along the Superstition Hills fault zone and nearby faults associated with the earthquakes of 24 November 1987: Bulletin of the Seismological Society of America, v. 79, p. 252-281.

Shearer, P., Hauksson, E., and Guoqing, L., 2005, Southern California Hypocenter Relocation with Waveform Cross Correlation, Part 2: Results Using Source-Specific Station Terms and Cluster Analysis: Bulletin of the Seismological Society of America, v. 95, no. 3, p. 904–915, doi: 10.1785/0120040168

Shirvell, C.R., 2006, Pliocene exhumation along the West Salton Detachment system and tectonic evolution of the Fish Creek–Vallecito supradetachment basin, Salton Trough, southern California [MS thesis]: Los Angeles, University of California, 133 p.

Sibson, R.H., 1996, Structural permeability of fluid-driven fault-fracture meshes: Journal of Structural Geology, v. 18, p. 1031-1042.

Spicak, A., 2000, Earthquake swarms and accompanying phenomena in intraplate regions: A review: Studia Geophysica et Geodaetica, v. 44, p. 89-106.

Steely, A.N., 2006, The evolution from late Miocene West Salton detachment faulting to

cross-cutting oblique strike-slip faults in the southwest Salton Trough, California [M.S. thesis]: Logan, Utah State University, 253 p., 3 plates, scale 1:24,000.

Steely, A.N., Janecke, S.U., Dorsey, R.J., and Axen, G.J., 2009, Early Pleistocene initiation of the San Felipe fault zone, SW Salton Trough, during reorganization of the San Andreas fault system: Geological Society of America Bulletin, v. 121, no. 5-6, p. 663-687, doi: 10.1130/B26239.1

Thatcher, W., Hileman, J.A., and Hanks, T.C., 1975, Seismic Slip Distribution along the San Jacinto Fault Zone, Southern California, and Its Implications: Geological Society of America Bulletin, v. 86, no. 8, p. 1140-1146, doi: 10.1130/0016-7606

Tong, X., Sandwell, D.T., and Smith-Konter, B.R., 2011, High resolution interseismic velocity model of the San Andreas Fault from GPS and InSAR: American Geophysical Union, abstract G41A-0723.

Townend, J., and Zoback, M.D., 2004, Regional tectonic stress near the San Andreas fault in central and southern California: Geophysical Research Letters, v. 31, L15S11, doi:10.1029/2003GL018918

Van Zandt, A.J., Mellors, R.J., and Lindsay, M., 2004, Surface deformation in the Western Salton Trough as observed by InSAR: poster presentation at Southern California Earthquake Center annual meeting.

Vincent, P., 2000, Aseismic slip events along the southern San Andreas fault system captured by radar interferometry: In proceedings of the 3rd Conference on Tectonic Problems of the San Andreas Fault System, Bokelmann, G., Kovach, R.L., editors, p. 193, https://e-reports-ext.llnl.gov/pdf/240798.pdf.

Wagoner, J.L., 1977, Stratigraphy and sedimentation of the Pleistocene Brawley and Borrego formations in the San Felipe Hills area, Imperial Valley, California, U.S.A. [M.S. Thesis]: Riverside, University of California Riverside, 128 p.

Wallace, R.E., 1990, The San Andreas fault system, California: United States Geological Survey Professional Paper, 1515.

Waters, M.R., 1983, Late Holocene Lacustrine Chronology and Archaeology of Ancient Lake Cahuilla, California: Quaternary Research, v. 19, p. 373-387.

Wdowinski, S., 2009, Deep creep as a cause for the excess seismicity along the San Jacinto fault: Nature Geoscience, v. 2, no. 12, p. 882-885.

Wei, M., Sandwell, D., and Fialko, Y., 2009, A silent M w 4.7 slip event of October 2006 on the Superstition Hills fault, southern California: Journal of Geophysical Research, v. 114, B07402, doi:10.1029/2008JB006135.

Wesnousky, S.G., 2006, Predicting the endpoints of earthquake ruptures: Nature, v. 444, no. 7117, p. 358-360.

Winker, C.D., 1987, Neogene stratigraphy of the Fish Creek - Vallecito section, southern California: Implications for early history of the northern Gulf of California and Colorado delta [Ph.D. dissertation]: Tucson, University of Arizona, 494 p.

Winker, C.D., and Kidwell, S.M., 1986, Paleocurrent evidence for lateral displacement of the Colorado River delta by the San Andreas fault system, southeastern California: Geology, v. 14, p. 788-791.

Winker, C.D., and Kidwell, S.M., 1996, Stratigraphy of a marine rift basin: Neogene of the western Salton Trough, California, *in* Abbott, P.L., and Cooper, J.D., eds.,

Field conference guidebook and volume for the annual convention, San Diego, California, May, 1996, Bakersfield, California: Pacific Section, American Association of Petroleum Geologist, p. 295-336.

Yang, W., Hauksson, E., and Shearer, P.M., 2012, Computing a large refined catalog of focal mechanisms for southern California (1981 – 2010): Temporal stability of the style of faulting: Bulletin of the Seismological Society of America, v. 102, p. 1179 – 1194, doi: 10.1785/0120110311, 2012.

APPENDIXES

A PHOTOGRAPH UTM LOCATIONS

Figure #	Part	Northing	Easting
8	A	600761	3668997
8	B	602254	3671418
8	C	602238	3671401
11	A	602011	3668184
11	B	604019	3671022
14	A	603908	3668294
14	B	601554	3665615
14	C	600552	3664901
18	A	600762	3669002
18	B	604937	3669973
18	C	601581	3665631
18	D	600966	3664906
18	E	603039	3666527
18	F	610608	3660908
28	A	601553	3665619
28	B	600510	3664914

B HYPOCENTERS IN NORTHWEST-TRENDING LINEAMENTS

2008 swarm events

Date	Latitude	Longitude	Depth	Magnitude
2008	33.07538	115.91212	6.747	2.29
1982	33.07567	-115.91084	7.79	1.61
2008	33.07436	-115.91027	6.604	1.97
2008	33.07487	-115.90999	6.68	2.32
2008	33.07536	-115.90984	6.633	1.43
2008	33.07378	-115.90978	6.653	2.41
2008	33.07343	-115.90932	6.645	1.43
1989	33.07239	-115.90345	7.275	2.04
1989	33.0722	-115.9033	7.333	2.23
1989	33.07262	-115.9029	7.361	2.15
1989	33.07234	-115.9029	7.389	1.2
1989	33.07257	-115.9026	7.462	1
2008	33.0677	-115.8986	5.572	1.22

1989	33.0695	-115.8981	13.29	1.4
2008	33.06822	-115.8976	6.437	1.03
2008	33.06786	-115.8974	6.943	1.98
1987	33.069	-115.8973	6.94	2.22
2008	33.06761	-115.8969	6.686	2.45
2008	33.0699	-115.8968	5.575	1.77
2008	33.07013	-115.8966	5.146	1.86
2008	33.06697	-115.8965	6.944	1.43
2008	33.06906	-115.8962	6.139	2.4
2008	33.06739	-115.8960	6.537	2.7
2008	33.06744	-115.8960	6.564	2.01
2008	33.06916	-115.8959	4.6	1.83
1987	33.0655	-115.8958	7.79	2.32
2008	33.06528	-115.8955	6.523	2.59
2008	33.06923	-115.8955	5.369	2.57
2008	33.06626	-115.8953	6.806	2.47
2008	33.06641	-115.8949	6.741	2.53
2008	33.06877	-115.8946	5.217	1.74
1987	33.06747	-115.8945	3.267	2.04
2008	33.06771	-115.8942	5.345	2.82
2008	33.06743	-115.8939	4.277	1.9
2008	33.06562	-115.8937	6.889	1.71
2008	33.06638	-115.8937	7.19	1.73
2008	33.06503	-115.8936	7.181	2.32
2008	33.06755	-115.8934	5.114	1.71
2008	33.06779	-115.8932	4.903	3.24
2008	33.06613	-115.8932	7.231	1.99
2008	33.06723	-115.8932	6.153	2.06
2008	33.06597	-115.8931	7.254	1.82
2008	33.06642	-115.8931	3.771	1.25
2008	33.06586	-115.8931	5.62	2.09
2008	33.06579	-115.8930	5.749	2.43
2008	33.06517	-115.8929	6.145	2.9
2008	33.06596	-115.8929	7.219	2.71
2008	33.06556	-115.8929	7.328	2.34
2008	33.06591	-115.8929	5.77	1.49
2008	33.06558	-115.8929	5.685	1.93
2008	33.06474	-115.8928	6.935	0.95
2008	33.06482	-115.8928	6.372	1.8
2008	33.06487	-115.8928	6.447	1.8
2008	33.06486	-115.8928	6.015	3.3
2008	33.06472	-115.8928	7.016	1.3
2008	33.06539	-115.8928	5.803	1.36

2008	33.06523	-115.8927	5.911	1.75
2008	33.06524	-115.8927	6.037	1.22
2008	33.06495	-115.8925	6.167	1.8
2008	33.06647	-115.8925	5.199	2.5
2008	33.0645	-115.8925	6.992	1.81
2008	33.06633	-115.8925	3.903	1.65
2008	33.06429	-115.8925	6.703	1.97
2008	33.0641	-115.8920	5.874	1.11
2008	33.06518	-115.8919	5.536	1.85
2008	33.06363	-115.8918	6.998	0.8
2008	33.06466	-115.8915	6.746	2.28
2008	33.06471	-115.8914	5.329	1.96
2008	33.06384	-115.8913	5.871	2.93
2008	33.06335	-115.8913	6.501	1.81
2008	33.06359	-115.8911	7.145	1.67
2008	33.06325	-115.8910	7.076	1.48
2008	33.06425	-115.8909	7.196	1.14
2008	33.06333	-115.8909	5.944	1.6
2008	33.06335	-115.8909	7.125	0.7
2008	33.06372	-115.8909	5.507	2.21
2008	33.06559	-115.8908	3.85	1.5
2008	33.06314	-115.8907	7.096	1.5
2008	33.06357	-115.8907	6.533	2.22
2008	33.06326	-115.8907	6.536	2.43
2008	33.06364	-115.8906	7.241	1.7
2008	33.06286	-115.8905	7.08	1.54
2008	33.06305	-115.8905	7.418	1.53
2008	33.06342	-115.8903	6.744	1.91
2008	33.06327	-115.8902	6.888	1.73
2008	33.06302	-115.8899	6.784	1.63
2008	33.06221	-115.8899	7.17	1.85
2008	33.06297	-115.8899	6.813	1.89
2008	33.0641	-115.8898	5.049	2.1
2008	33.0628	-115.8898	6.952	1.48
2008	33.06247	-115.8897	6.606	1.7
2008	33.06265	-115.8897	5.821	3.04
2008	33.06213	-115.8896	5.796	3.5
2008	33.06213	-115.8895	5.674	2
2008	33.06219	-115.8895	6.461	1.91
2008	33.0621	-115.8893	7.016	1.93
2008	33.06374	-115.8892	4.948	2.93
2008	33.06171	-115.8892	7.216	1.31
2008	33.06385	-115.8891	5.234	3.59

2008	33.06183	-115.8890	7.243	1.31
2008	33.06213	-115.8888	5.604	3.61
2008	33.06155	-115.8887	6.944	1.1
2008	33.06181	-115.8886	7.378	1.72
2008	33.0611	-115.8885	6.994	1.38
2008	33.06113	-115.8884	6.812	1.96
2008	33.06088	-115.8883	6.564	2.07
2008	33.06128	-115.8883	7.352	1.62
2008	33.06133	-115.8877	6.171	2.22
2008	33.06362	-115.8876	3.889	1.81
2008	33.06284	-115.8875	4.641	1.61
2008	33.06005	-115.8874	5.313	1.52
2008	33.06387	-115.8873	3.871	1.94
2008	33.06081	-115.8873	5.173	2.75
2008	33.06415	-115.8872	3.87	1.72
1987	33.0625	-115.8868	9.49	2.01
2008	33.05871	-115.8863	7.843	1.45
2008	33.05981	-115.8862	4.996	1.31
2005	33.06089	-115.8862	8.113	1.3
2008	33.06136	-115.8862	4.458	2
2008	33.05875	-115.8850	4.928	2.31
2008	33.05799	-115.8840	4.887	2.33
2008	33.05764	-115.8831	5.007	0.64
2008	33.05742	-115.8826	4.393	2.64
2008	33.05666	-115.8826	4.726	2.81
2005	33.0555	-115.882	8.77	1.49
2008	33.0558	-115.8818	4.692	1.5
2008	33.05497	-115.8809	4.452	1.48
1987	33.05483	-115.88	5.54	1.1

1994 and 1989 swarm events

Date	Latitude	Longitude	Depth	Magnitude
1994	33.07723	-115.94432	5.838	1.66
1994	33.07686	-115.94419	6.215	1.7
1994	33.07733	-115.94418	6.098	1.71
1994	33.07676	-115.94415	6.306	1.65
1994	33.07671	-115.94414	6.263	2.15
1994	33.07639	-115.94409	5.379	1.02
1994	33.07645	-115.94384	6.247	1.48
1994	33.07655	-115.94379	6.196	1.55

1994	33.07636	-115.94366	6.186	1.41
1994	33.07633	-115.94352	6.207	1.8
1994	33.07674	-115.94351	5.661	0.88
1994	33.0765	-115.94338	6.111	1.39
1994	33.0762	-115.94334	6.296	1.51
1994	33.07672	-115.94324	5.758	1.11
1994	33.07647	-115.94313	5.84	1.17
1994	33.07588	-115.94234	5.616	1.42
1989	33.07888	-115.94067	6.116	2.27
1989	33.07884	-115.9405	6.109	2.22
1989	33.07912	-115.94042	6.049	1.5
1989	33.0782	-115.94026	6.214	2.34
1989	33.07846	-115.94025	6.209	2.19
1989	33.0789	-115.94024	6.088	1.5
1989	33.07811	-115.9399	6.295	2.45
1989	33.07787	-115.93989	6.437	2.1
1989	33.07816	-115.93987	5.854	1.95
1989	33.07626	-115.93986	6.771	2.12
1989	33.07506	-115.93976	6.754	1.5
1989	33.07835	-115.93966	6.082	1.3
1989	33.07584	-115.93957	6.74	2.11
1989	33.07816	-115.93947	5.843	1.79
1989	33.07811	-115.93945	6.185	2.49
1989	33.07558	-115.93942	6.759	2.17
1989	33.07824	-115.93941	6.109	1.93
1989	33.07496	-115.9394	6.667	1.99
1989	33.0749	-115.93922	6.771	1.4
1989	33.07818	-115.9392	5.861	2.12
1989	33.07519	-115.93915	6.704	1.5
1989	33.07824	-115.93911	5.681	2.06
1989	33.07768	-115.93909	6.275	2.13
1989	33.07806	-115.93898	5.755	1.4
1989	33.07535	-115.93894	6.816	2.27
1989	33.07764	-115.9389	6.258	1.4
1989	33.07525	-115.9388	6.762	1.3
1989	33.07671	-115.93876	6.56	1.2
1989	33.0754	-115.93871	6.691	1.99
1989	33.07687	-115.93868	6.442	2.09
1989	33.07445	-115.93845	6.92	1.3
1989	33.07666	-115.93844	6.383	2.18
1989	33.07732	-115.93842	6.274	2
1989	33.07687	-115.93841	6.339	2.13
1989	33.07693	-115.93834	6.331	1.2

1989	33.07391	-115.93833	6.839	1.4
1989	33.07509	-115.93831	6.8	2.08
1989	33.07693	-115.93822	6.311	2.24
1989	33.0771	-115.93822	6.283	2.14
1989	33.07439	-115.93819	6.825	2.39
1989	33.07553	-115.93811	6.639	2.73
1989	33.07687	-115.93804	6.329	1.5
1989	33.07708	-115.93802	6.983	2.52
1989	33.07495	-115.93799	6.653	1.4
1989	33.07673	-115.93797	6.28	1.3
1989	33.07743	-115.93791	6.096	2.36
1989	33.07664	-115.9379	6.376	2.18
1989	33.07684	-115.9379	6.424	1.2
1989	33.07677	-115.93787	6.333	1.4
1989	33.07515	-115.93784	6.615	2.1
1989	33.07611	-115.93782	6.515	0.9
1989	33.07504	-115.93781	6.704	2.36
1989	33.07504	-115.93777	6.683	2.24
1989	33.07729	-115.93745	6.153	2.12
1989	33.07745	-115.93739	6.133	1.9
1989	33.07685	-115.93708	6.295	2.11
1989	33.07668	-115.93705	6.241	1.4
1989	33.07729	-115.93691	6.255	1.1
1989	33.0751	-115.93653	6.63	1.1
1989	33.07635	-115.93639	6.463	1
1989	33.07376	-115.93633	6.794	1
1989	33.0767	-115.9362	6.201	2.18
1989	33.0757	-115.93612	6.38	0.9
1989	33.0758	-115.9361	6.398	2.12
1989	33.0731	-115.93607	6.824	2.3
1989	33.0735	-115.93567	6.805	3.03
1982	33.0745	-115.9355	1.33	1.1
1989	33.07231	-115.93543	7.869	1.6
1989	33.075	-115.93266	10.59	1
1988	33.0695	-115.93183	11.96	1.86
1987	33.06943	-115.93002	6.491	3.32
1987	33.06891	-115.92971	6.631	3.22
1987	33.06983	-115.92954	5.769	2.25
1987	33.06885	-115.92935	6.747	3.25
1987	33.06875	-115.92751	5.038	3.09
1987	33.0713	-115.927	6.61	2.45
1987	33.06808	-115.92628	4.96	2.33
1987	33.06806	-115.92619	5.12	2.74

1989	33.07067	-115.926	9.09	2.37
1987	33.07238	-115.92553	5.259	2.93
1987	33.07215	-115.92532	5.338	2.19
1987	33.07188	-115.92496	4.384	2.68

C FAULT POINT DATA

Easting	Northing	Strike	dip
600527	3664912	55	68
609268	3663461	355	67
609607	3663018	186	40
604874	3662500	235	74
598814	3668745	77	50
601728	3668197	200	82
602097	3667976	25	29
602053	3662445	150	
601748	3659855	340	70
600981	3664926	30	39
601583	3665609	234	51
601749	3665515	186	88
601774	3665623	245	74
603138	3667073	332	52
603384	3667257	276	10
603185	3666656	56	81
602188	3668341	65	62
601483	3668941	27	25
600389	3666866	30	
600122	3666546	50	
599590	3666466	340	
599530	3666438	340	
599498	3666874	15	
599322	3667223	20	
599216	3667377	10	
598075	3668027	325	

598213	3668001	115	77
602451	3666086	210	75
602014	3666161	60	
602148	3666497	240	45
600024	3665880	155	79
596055	3668510	90	35
596906	3668063	325	
597219	3667753	350	
597300	3667732	102	63
605068	3662594	350	57
604998	3662768	200	14
604582	3661928	30	
601679	3660932	168	82
601736	3660834	40	59
601805	3660459	275	37
601821	3658895	60	5
601962	3658679	10	
601940	3658750	350	
601933	3660858	40	
608184	3663588	30	82
610618	3661072	300	32
610631	3660984	55	
611517	3661316	35	
603042	3659554	60	
604451	3659801	205	
605444	3661317	0	71
605117	3661582	345	44
605155	3661817	5	70
605327	3661881	0	76
603225	3662325	275	66
605177	3662872	45	66
605128	3662850	34	38
605561	3662427	20	64
599104	3666002	44	44
599089	3665984	355	67

598618	3666568	205	50
598040	3666755	170	75
597630	3666592	5	78
596765	3666794	0	
596105	3666798	30	79
592786	3668222	224	55
594164	3668254	220	87
594249	3668257	220	87
594256	3668326	220	90
594069	3668701	30	74
593698	3668555	18	49
593559	3668513	75	41
594250	3666685	60	
596584	3665848	120	66
605016	3666252	330E?	
604344	3667494	70e	
603947	3668247	35	58
608155	3662311	340	54
608368	3662462	355	
612876	3662168	320	80
594370	3665294	15?	
605050	3666234	330	90
600573	3666764	220	49
600739	3667008	40	47
600829	3667031	205	74
600861	3667053	120	78
600799	3667084	210	50
600879	3667230	15	87
601013	3667263	340	64
601026	3667357	210	7
601190	3667342	25	61
601330	3667394	170	90
601328	3667440	60?	
601459	3667734	218	90
601170	3668072	25?	

600432	3667339	20?	
600310	3667147	340	80
600153	3666959	220	84
597243	3667168	318	57
597519	3666864	320	
598753	3666758	220	45
599362	3664372	73	
599904	3666754	55	
600337	3667241	75	13
601615	3665589	96	62
601500	3665618	242	52
601662	3665577	90	
601675	3665562	18	80
599904	3666255	0	
599914	3666731	52	
599952	3667145	35	
600031	3667784	30	
600096	3667875	225	84
600483	3668703	40	
599997	3667911	70	55
601659	3665546	50	
601240	3664871	0	
608518	3663416	357	
607966	3663373	35	
607917	3663392	56	
606380	3663868	170	74
598064	3666131	333	47
598114	3666044	325	
606368	3662516	90	
606475	3662645	345	86
604289	3662781	320	
602660	3660855	358	0
603207	3661905	0	
596207	3667808	330	
596330	3667733	0	

596440	3667690	325	
596505	3667695	13	
596519	3667734	5	
596596	3667720	325	
596826	3667701	330	
596774	3667816	335	
596741	3667837	326	
596673	3667808	53	69
596673	3667808	335	
596446	3667874	326	57
603382	3671275	225	
603450	3671244	225	57
603478	3671230	10	
603852	3671090	185	30
604018	3671019	20	34
604087	3670929	215	17
604135	3670901	200	68
604205	3670858	215	15
604220	3670843	35	39
604747	3670213	30	84
604936	3669967	35	83

D Focal Mechanisms

Year	Latitude	Longitude	depth	magnitude	strike	dip	rake
1996	33.082	-115.94566	2.65	1.92	96	84	170
1994	33.08216	-115.94334	2.41	1.74	316	39	-161
1987	33.0725	-115.93233	3.39	2.8	257	77	-165
1987	33.06433	-115.92883	4.92	3.83	106	70	-164
1987	33.05733	-115.93283	5.64	3.54	283	62	166
1987	33.052	-115.91883	3.18	2.3	262	75	137
1987	33.05517	-115.91734	3.66	2	293	88	-148
2003	33.05383	-115.91183	3.25	1.12	269	82	147
2003	33.05917	-115.90867	2.96	3.14	298	73	160
1987	33.04733	-115.8135	10.1	3.82	314	80	-172
1987	33.08167	-115.81633	7.72	1.79	313	77	-176
1987	33.06717	-115.79567	5.16	3.05	304	70	-149

1987	33.07383	-115.78133	8.16	4.22	174	54	-73
1986	33.07833	-116.038	3.65	1.9	292	89	-166
1999	33.055	-115.90434	5.12	2.86	125	88	-153
1999	33.05317	-115.905	6.11	2.92	299	82	148
1999	33.04984	-115.901	5.45	3.36	295	82	148
1987	33.0395	-115.87167	3.7	1.98	111	58	151
1988	33.053	-115.85717	4.5	2.62	123	84	-152
1992	33.0455	-115.85033	3.72	2.09	129	69	-167
1988	33.03783	-115.845	5.04	1.73	130	63	175
1987	33.03883	-115.82433	5.6	2.55	139	89	178
1987	33.03767	-115.8215	5.6	2.04	112	82	-139
1985	33.17617	-115.82066	7.65	1.77	300	70	-147
2000	33.16467	-115.92533	8.26	2.01	304	81	-178
1994	33.11717	-116.04916	5.78	1.48	269	72	-146
1985	33.11183	-116.05067	3.96	2.41	126	85	-172
1996	33.09917	-116.02433	4.16	1.53	287	73	162